Ion Composition in Titan's Exosphere via the Cassini Plasma Spectrometer

_____

A Dissertation

Presented to

the faculty of the School of Engineering and Applied Science

University of Virginia

_____

in partial fulfillment

of the requirements for the degree

Doctor of Philosophy

by

Adam Kyle Woodson

December

2014

APPROVAL SHEET

The dissertation

is submitted in partial fulfillment of the requirements

for the degree of

Doctor of Philosophy

_____
AUTHOR

The dissertation has been read and approved by the examining committee:

Robert E. Johnson
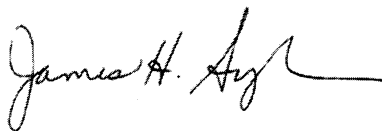Advisor

Peter Arnold

Phil Arras

Frank J. Crary

Petra Reinke

Howard T. Smith

Accepted for the School of Engineering and Applied Science:

Dean, School of Engineering and Applied Science

December

2014

Abstract

A primary goal of the Cassini mission has been to measure atmospheric loss at Saturn's largest moon, Titan. Multiple processes such as sputtering and electromagnetic pickup of ionized neutrals can erode atmospheres over time. Titan is particularly interesting because unlike satellites of similar size and mass in comparably hostile environments, such as Io, Europa and Ganymede at Jupiter, it has managed to retain a column density nearly 10 times that of Earth and an atmospheric-mass to solid ratio comparable to Venus. However, based on some predicted loss rates Titan should have shed a significant portion of its present atmosphere over the lifetime of the solar system [Johnson, 2009]. Prior to the Cassini mission, therefore, Titan's atmosphere was believed to be the primary source of ambient nitrogen in Saturn's magnetosphere. As it turns out, evidence for that contribution has proven elusive and, instead, Enceladus appears to be the primary source of both water *and* nitrogen [Smith et al. 2007, 2008]. Here we study the composition of ions in Titan's exosphere in order to understand the loss processes occurring and better explain the atmosphere's resilience in the context of Saturn's erosive magnetospheric plasma.

My research has focused on calibration of Cassini's Ion Mass Spectrometer (IMS) and analysis of data collected by IMS near Titan. This research has culminated in 1) a numerical method for extracting ion compositions from IMS measurements, 2) an analysis of the ion composition sampled by IMS during the T40 Titan encounter and a comparison of that anlaysis with numerical models of Titan's magnetospheric plasma

interaction, and 3) the design and partial implementation of an experiment to measure the number statistics of ion-induced electron emission from thin carbon foils as it pertains to time-of-flight mass spectrometers like IMS.

List of Figures, Credits, and Copyrights

Please refer to the tables below for source, accredidation, and copyright information pertaining to each of the figures appearing in this dissertation. In the interest of maintaining concise figure captions, the information has not been included in the body of the dissertation. Instead, a reference to this list is included in each figure caption.

Figure 2.1.2: The relative sizes of Saturn's 21 largest satellites
Page: 12
Source: http://www.dlr.de/dlr/en/desktopdefault.aspx/tabid10405/ 596_read-169/#/gallery/304
Credit: NASA/JPL–Caltech /David Seal

Figure 2.1.3: The scale of the Kronian system
Page: 13
Source: http://randomdijit.blogspot.com/2011/07/ grand-tour-of-saturns-moons-part-1.html
Credit: D. J. Turk

Figure 2.1.4: Enceladus and its plumes
Page: 14
Source: **Left:** http://photojournal.jpl.nasa.gov/catalog/PIA06254 **Right:** http://photojournal.jpl.nasa.gov/catalog/PIA07758
Credit: **Left:** NASA/JPL–Caltech /Space Science Institute **Right:** NASA/JPL–Caltech /Space Science Institute

Figure 2.2.1: The Dungey cycle
Page: 17
Source: http://commons.wikimedia.org/wiki/File:Magnetopause.svg
Credit: RicHard-59

Figure 2.2.2: Magnetosphere size comparison
Page: 18
Source: Donahue, M., N. Schneider, and M. Voit. *The cosmic perspective: The Solar System*, 4th ed. Pearson Addison-Wesley, 2005.
Copyright: © 2005 Pearson Education Inc., publishing as Addison Wesley

Figure 2.2.3: Magnetospheric electric potentials
Page: 19
Source: Cravens, T. E. *Physics of Solar System Plasmas*. Cambridge, UK: Cambridge University Press, November 2004.
Copyright: © 2004 Cambridge University Press

Figure 2.2.4: Charged-particle drift motion
Page: 20
Source: Cravens, T. E. *Physics of Solar System Plasmas*. Cambridge, UK: Cambridge University Press, November 2004.
Copyright: © 2004 Cambridge University Press

Figure 2.2.5: Magnetospheric regions and currents
Page: 22
Source: Russell, C. T. "The dynamics of planetary magnetospheres." *Planetary and Space Science* 49.10 (2001): 1005-1030.
CopyRight: © 2001 Elsevier Science Ltd.

Figure 2.2.6: Saturn's distorted magnetosphere
Page: 23
Source: Arridge, C. S., et al. "Warping of Saturn's magnetospheric and magnetotail current sheets." *Journal of Geophysical Research: Space Physics (1978–2012)* 113.A8 (2008).
Copyright: © 2008 American Geophysical Union

Figure 2.3.1: Titan's induced magnetosphere
Page: 25
Source: Sittler, E. C., et al. "Energy deposition processes in Titan's upper atmosphere and its induced magnetosphere." *Titan from Cassini-Huygens*. Springer Netherlands, 2010. 393-453.

Figure 2.4.1: Titan and its north-polar sea

Page: 27

Source:
  Left: http://photojournal.jpl.nasa.gov/catalog/PIA18432
  Right: http://photojournal.jpl.nasa.gov/catalog/PIA14602

Credit:
  Left: NASA/JPL–Caltech/Space Science Institute
  Right: NASA/JPL–Caltech/University of Arizona/University of Idaho

Figure 2.4.2: Chemical pathways in Titan's ionosphere

Page: 28

Source: Cravens, T. E., et al. "Composition and structure of the ionosphere and thermosphere." *Titan From Cassini-Huygens*. Springer Netherlands, 2010. 259-295.

Figure 2.4.3: Haze formation in Titan's atmosphere

Page: 30

Source:
  Left: Waite, J. H., et al. "The process of tholin formation in Titan's upper atmosphere." *Science* 316.5826 (2007): 870-875.
  Right: http://lifeng.lamost.org/courses/astrotoday/CHAISSON/AT312/ HTML/AT31205.HTM

Credit:
  Left: N/A
  Right: unknown

Copyright:
  Left: © 2007 American Association for the Advancement of Science
  Right: N/A

Figure 3.2.1: CAPS Ion Mass Spectrometer

Table of Contents

1. Introduction

1.1 Cassini Mission Overview

Prior to 1979 all of our empirical knowledge about the Kronian system, which primarily concerned the composition of Saturn's upper and middle atmosphere, came from Earth-based radio and optical observations. Within the last few decades those observations have been supplemented by Earth-orbiting instruments including the International Ultraviolet Explorer, the Hubble Space Telescope, and the Infrared Space Observatory. Moreover, during a "golden era" from 1979 to 1981 Pioneer 11, Voyager 1 and Voyager 2 each took measurements at Saturn en route to their intended destinations. The data acquired by these three spacecraft kick-started a much broader study of the complex interactions between Saturn's magnetosphere, its intricate ring structure, and its numerous satellites.

Launched on October 15th, 1997, the Cassini spacecraft crossed the 1.2 billion kilometers between Earth and Saturn with gravitational assists from Venus, Earth, and Jupiter and inserted into orbit at Saturn on July 1, 2004. The fuel savings garnered from these assists allowed for one of the most extensive scientific payloads ever flown. Photographed in Figure 1.1.1, the "school bus sized" spacecraft carries 12 different instruments designed to carry out 27 scientific investigations. Each instrument is categorized as "optical remote sensing" (Composite Infrared Spectrometer, Imaging Science Subsystem, Ultraviolet Imaging Spectrograph, and Visible and Infrared Mapping

Spectrometer), "microwave remote sensing" (Radar and Radio Science Subsystem), or "particles and fields" (Cassini Plasma Spectrometer, Cosmic Dust Analyzer, Ion and Neutral Mass Spectrometer, Magnetometer, Magnetospheric Imaging Instrument, and Radio and Plasma Wave Science instrument). Cassini also transported the Huygens probe, consisting of six additional instruments (Huygens Atmospheric Structure Instrument, Doppler Wind Instrument, Descent Imager/Spectral Radiometer, Gas Cromatograph Mass Spectrometer, Aerosol Collector and Pyrolyser, and Surface Science Package) which descended to Titan's surface on January 14th, 2005, collecting data in transit and at the landing site which, based on accelerometer data, had the consistency of damp sand [Schröder et al., 2012].
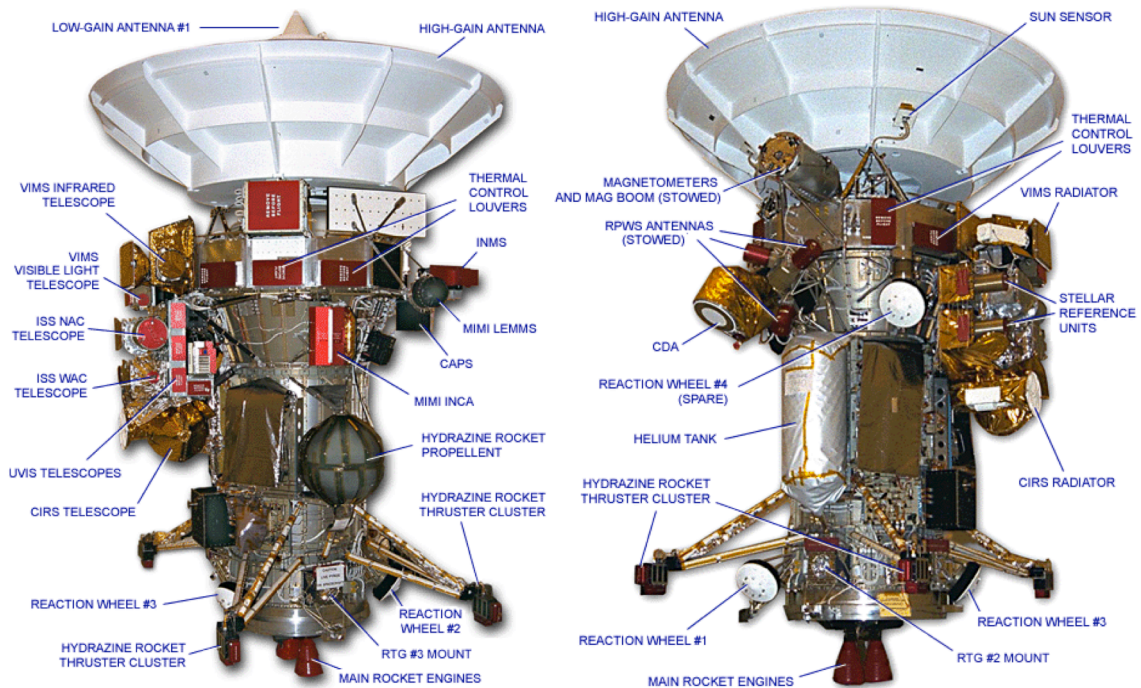
Figure 1.1.1 The Cassini orbiter

Annotated photographs of the orbiter showing instrument locations (Huygens probe not pictured) as well as steering and propulsion mechanisms. See pages I–XI for attributions.

During Cassini's "Prime" mission, which began with orbital insertion just after Saturn's northern winter solstice in July of 2004 (see Figure 1.1.2), the spacecraft conducted thorough studies of Saturn's atmospheric structure and composition, the configuration and composition of its rings, the internal structure and surface morphology of Titan and the icy moons, the composition and structure of Titan's atmosphere, the roles of the rings and moons in contributing plasma to the magnetosphere, and the magnetosphere's overall geometry and variability. By the end of the nominal mission Cassini had completed 75 orbits around Saturn including 44 Titan encounters and 4 encounters with Enceladus.
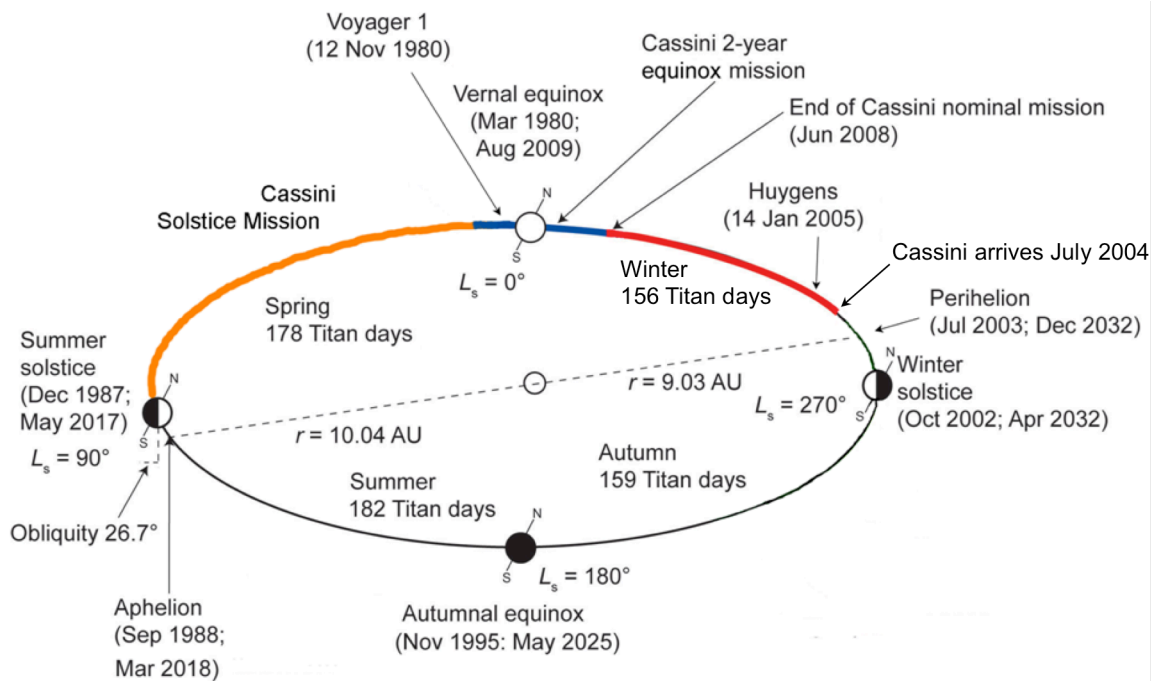
Figure 1.1.2 Saturn's seasons

A schematic diagram indicating the duration of each season and of each Cassini mission segment in relation to the Saturn year. One Titan day is equivalent to ~15.9 Earth days. See pages I–XI for attributions.

After completing its nominal objectives Cassini's mission was extended through equinox until July 1st, 2010, in order to build upon the knowledge gained during the successful prime mission. This extended mission was aptly named the "Equinox" mission, during which Cassini flew an additional 65 orbits, including 27 additional encounters with Titan and 7 with Enceladus, and continued to gather data on all previous objectives. At the end of the Equinox mission in 2010 Cassini was granted a second extended mission—the "Solstice" mission—scheduled to end in May of 2017 just after

Saturn's northern summer solstice.

By the end of the Solstice mission Cassini will have completed a total of 295 orbits, 125 Titan encounters, and 22 encounters with Enceladus. The two extended missions have given Cassini the unprecedented opportunity to observe the Kronian system over a full seasonal cycle and measure associated changes in processes driven by solar intensity such as atmospheric photochemistry, photoionization of neutral populations, photodesorption from the surfaces of icy bodies and ring particles, and the resulting coupling of these processes to the magnetosphere. Figure 1.1.3 summarizes the orbits associated with Cassini's primary and two extended mission from 2004 through 2017.

Despite an electrical malfunction in 2012 (well into the second extended mission) that required the indefinite shutdown of the Cassini Plasma Spectrometer, Cassini has undoubtedly been one of—if not *the* most—successful missions in the history of space exploration. In fact, during the most recent NASA senior review (in which project teams petition for extended funding beyond their primary budgeted missions) Cassini was the only project to receive an "Excellent" rating and procure full funding through the end of the Solstice mission when, having expended its fuel reserves, the spacecraft will be plunged into Saturn's atmosphere. In other words, we can look forward to three more years of breathtaking images and revolutionary discoveries from what is perhaps the most beautiful and complex environment in our solar system.
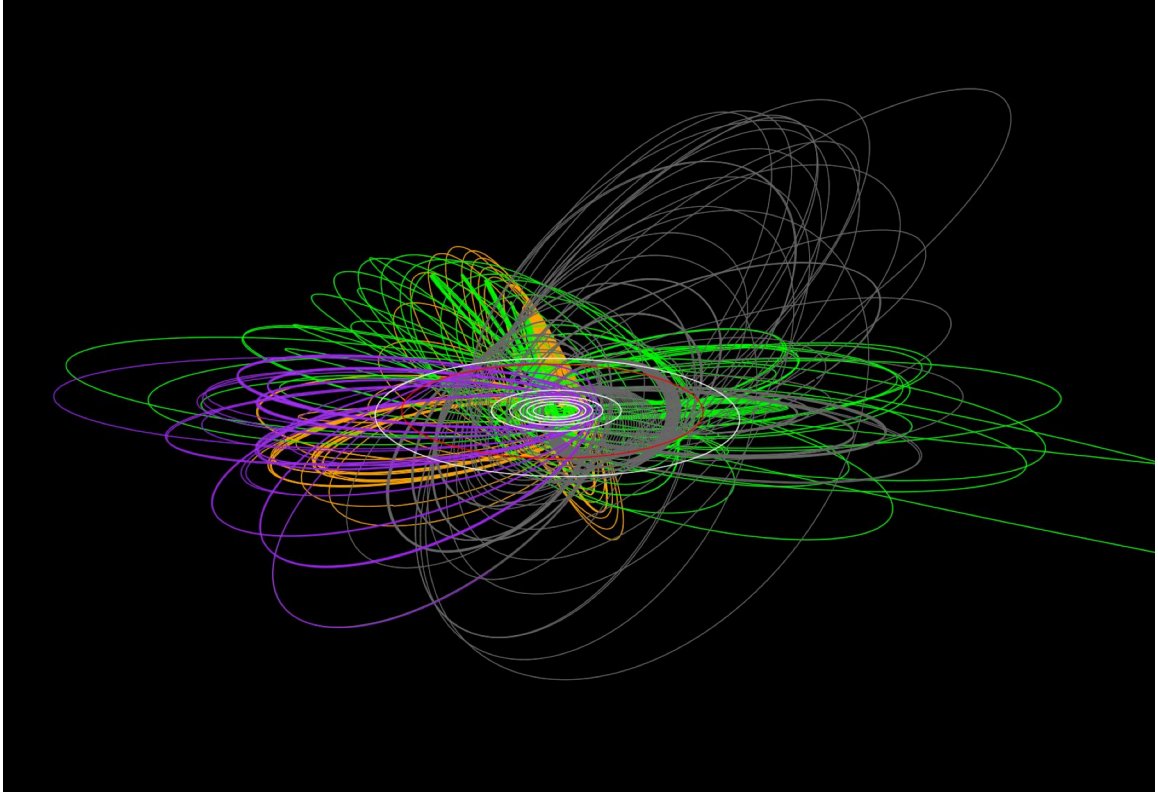
Figure 1.1.3 Cassini mission orbital mechanics

A computer graphic showing the orbits associated with Cassini's prime (green), Equinox (orange), and Solstice missions. The Solstice orbits occuring prior to 15 October 2012 (Cassini's 15th anniversary) are shown in purple, and those occuring between that date and the mission's end are drawn in dark gray. Saturn is in the center, with the orbit of its largest moon, Titan, in red and the orbits of its six other inner satellites in white. See pages I–XI for attributions.

1.2 Research goals and justification

My research goals have shifted over the course of my graduate study. For the first five years I worked on an experiment to measure the number statistics of electrons

ejected from thin carbon foils by incident ions. These statistics are important for thorough calibration of the foil-based time-of-flight (TOF) mechanism that IMS uses to determine mass, since existing calibration data addresses only a fraction of the energies and ion species measured.

The number of ions emitted from a thin (~10 nm) carbon foil by penetrating ions is a function of ion species and energy. An ion entering IMS is accelerated through such a foil and the emitted electrons are steered almost instantaneously (relative to the ion) by an electric field onto a microchannel plate (MCP) detector where they trigger a flight timer for the parent ion. The probability that the electrons, and thereby the parent ion, are detected is a function of the number of electrons simultaneously incident on the MCP surface. Thus, it is imperative to measure these statistics in order to characterize the IMS counting loss and accurately convert from ion counts to ion densities. A detailed explanation of IMS operation is given in Section 3.2 and the electron number statistics are discussed in detail in Appendix A.

Due to a number of obstacles including funding cuts, the experiment has not been finished. However, a detailed discussion of the design and partial implementation of the experiment is presented in Appendix A. Given that foil-based TOF mass spectrometers have been flown in at least 20 space missions since 1990, including the current New Horizons and Maven missions to Pluto and Mars, respectively, it is my hope to revisit this experiment at some point in the near future.

In 2012 my focus changed from IMS calibration to IMS data analysis. Specifically, I have worked to extract ion compositions from the TOF spectra acquired by IMS within Titan's induced magnetosphere, between the moon's exobase and magnetic pileup boundary (MPB). The exobase marks the altitude at which an upward traveling molecule experiences only one collision, on average, over a scale height—the distance over which the density decreases by a factor of *e*. Thus, in the region above the exobase, called the exosphere, the atmosphere is no longer collisional. The MPB (alternately called the draping boundary) is the region where Saturn's magnetic field, rotating faster than Titan orbits the planet, encounters Titan's upper ionosphere and becomes draped around the moon. This boundary effectively serves to separate ions emerging from Titan's atmosphere (which I and others have shown to comprise primarily low-energy molecular hydrogen and hydrocarbons) from Saturn's corotating ambient plasma, which is dominated by energetic water-group ions sourced from Saturn's atmosphere and icy satellites and ring particles [Thomsen et al., 2010].

To analyze the compositions I developed a suite of computer programs in C to search the raw IMS data files for relevant time and altitude ranges, reconstruct TOF spectra from the collapsed raw data, calculate ephemerides such as spacecraft trajectory and instrument pointing, and perform fast, robust, multi-parameter peak fitting on the reconstructed TOF spectra. In addition, I developed a number of programs in Mathematica to extrapolate detection efficiencies from the limited set of simulated efficiencies and to plot the data and ephemerides in various ways. These methods have been applied to the T40 Titan encounter using fortuitous measurements by Cassini's Ion

and Neutral Mass Spectrometer (INMS), acquired during the same pass, as a template for peak selection. In addition to making the first reported observation of H_3^+ at Titan—an ion potentially important for radiative cooling in the upper atmosphere—the abundances that I extracted from the data were used to evaluate three different numerical models of Titan's interaction region [Woodson et al., 2014]. In addition to this work I have contributed to two other peer-reviewed journal articles and a NASA proposal for a novel ion mass spectrometer design, and I have presented my work at a number of professional conferences, including an invited talk at the December 2013 meeting of the American Geophysical Union. A compilation of these works is provided in Appendix B.

1.3 Thesis structure

Section 2 of this thesis provides a succinct introduction to the Kronian system, including Saturn and its rings and moons, the dynamics of Saturn's magnetosphere, the interaction of the magnetosphere with Titan's atmosphere, and the ways in which that interaction may drive atmospheric loss. Section 3 is an adaptation of the material presented in Woodson et al. [2014]. It discusses the operation of IMS, conditions during the T40 encounter, the numerical techniques used to extract ion compositions from the data, and comparison of the extracted abundances with several numerical models of Titan's interaction region. Lastly, Section 4 summarizes the conclusions obtained from the data analysis, and a thorough discussion of the electron emission experiment is provided in Appendix A.

2. Titan's interaction with Saturn's magnetosphere

2.1 Overview of the Kronian System

Saturn, pictured in Figure 2.1.1, is the sixth planet from the Sun and the second largest (mean radius ~60,000 km) in the Solar System after Jupiter (mean radius ~70,000 km). With an average orbital distance of ~1.4 million km it resides nearly twice as far from the Sun as Jupiter and nearly 10 times farther than Earth. As Figure 1.1.2 suggests, Saturn takes ~29.5 Earth years to complete a single orbit around the Sun, and the low eccentricity of that orbit yields perihelion and aphelion distances that differ by less than 6% from the average orbital distance. A day on Saturn lasts less than 11 Earth hours as the planet spins quickly about an axis tilted ~27° with respect to its orbital plane.

With 62 confirmed moons, 24 of which are "regular" moons having low-inclination prograde orbits, and 6 extended rings composed of countless bodies ranging in size from grains to boulders, the Kronian system is the most dynamic in the Solar System. In comparison, while Jupiter has five more known moons than Saturn—only eight of which are regular—its dusty rings are comparably faint, extending only half as far from the planet (~250,000 km) as Saturn's (~500,000 km). As will be discussed, this abundance of ring particles and satellites, through their contribution of plasma to Saturn's magnetosphere, plays a critical role in determining its size and dynamics. Figure 2.1.2 illustrates the relative sizes of Saturn's 21 largest moons, while Figure 2.1.3 conveys the

radial extent of Saturn's seven rings and the positions of its 24 regular moons in relation to them.
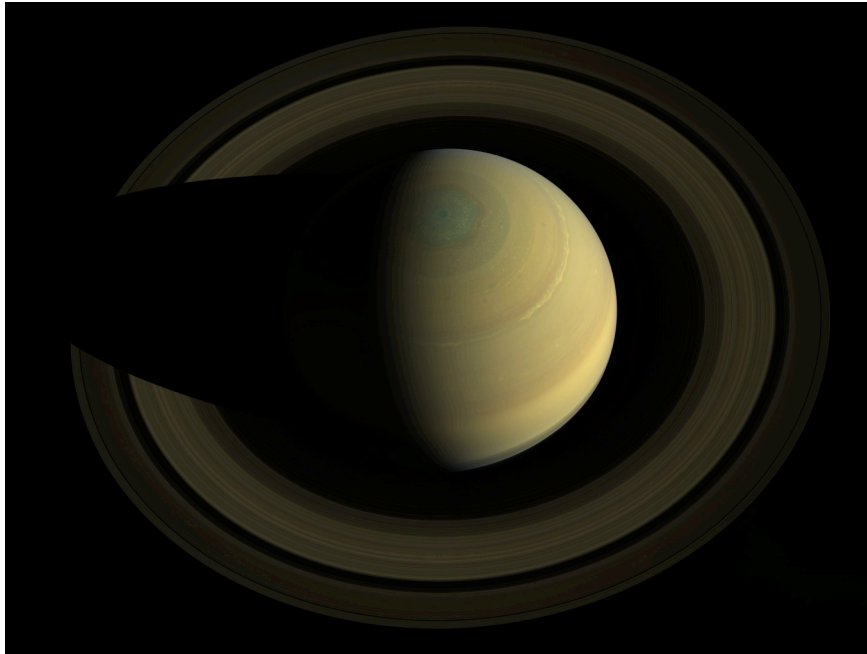
Figure 2.1.1 Saturn and its main rings

A natural-color, top-down mosaic of Saturn and its A, B, and C rings (from outside to inside) created from 36 different images acquired by Cassini's Imaging Science Subsystem on October 10, 2013. See pages I–XI for attributions.

The water-ice composition of Saturn's rings reflects the compositions of its 5 innermost icy satellites: Mimas, Enceladus, Tethys, Dione, and Rhea, all of which are too small to maintain significant atmospheres. The origin of the rings is still debated but most theories maintain that the main A, B, and C rings (see Figure 2.1.3)—in which particle sizes range from microns to meters—represent the remains of an icy moon that was torn apart by some combination of asteroid bombardment and tidal forces [Canup, 2010].

Shape and gravity measurements indicate densities consistent with water ice and varying silicate content [Matson et al., 2009], and while there is evidence for resurfacing in the past, craters and fractures suggest little present-day geologic activity on all but Enceladus [Dones et al., 2009]. The variation in silicate content among the cores of these inner moons, which ranges from 6% (Tethys) to 57% (Enceladus), has been attributed to a compact, massive proto-disk containing silicates and ice. In this scenario, moons formed near the edge of the disk would be composed primarily of ice, while rocky bodies inside the disk would have accreted ice as they migrated outward, eventually being thrown from the disk by tidal forces [Charnoz et al., 2011].
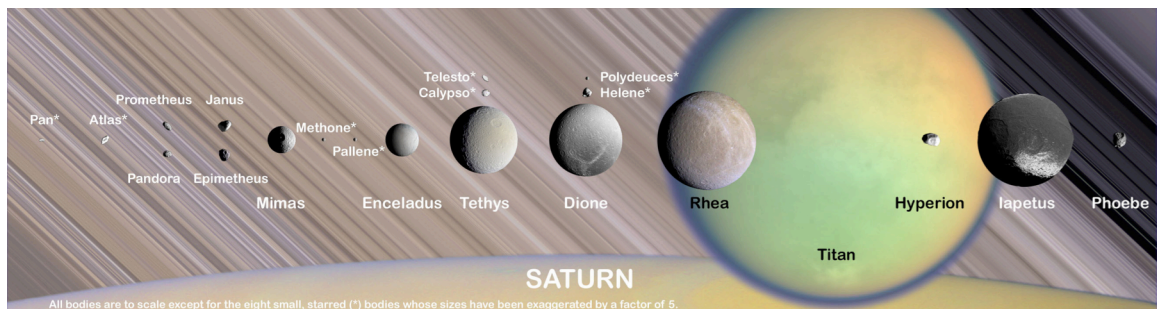
Figure 2.1.2 The relative sizes of Saturn's 21 largest satellites

See pages I–XI for attributions.
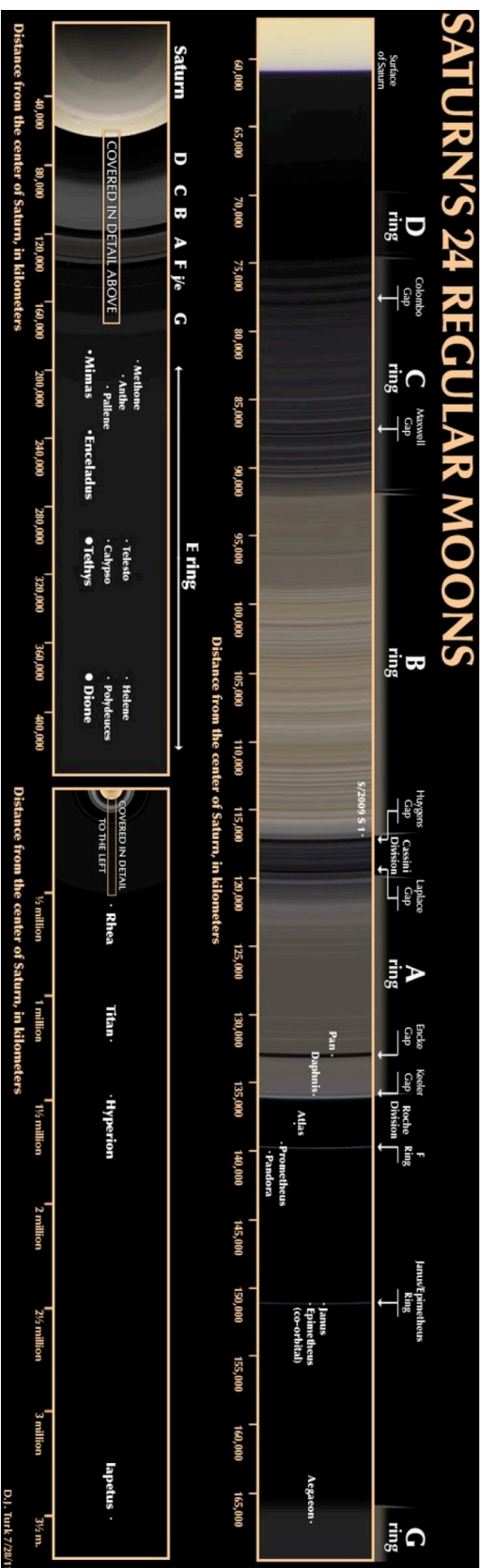
Figure 2.1.3 The scale of the Kronian system.

A montage depicting the extent of Saturn's rings and the radial position of each of its 24 regular moons. See pages I–XI for attributions.

The rings and icy moons are therefore the primary source of water-group ions (H^+, O^+, OH^+, H_2O^+, and H_3O^+) in the Kronian system, which comprise the bulk of Saturn's magnetospheric plasma along with lesser amounts of N^+ and H_2^+ [Thomsen et al., 2010]. Of these sources, Enceladus—pictured in Figure 2.1.4—is perhaps the most prolific, giving rise to the broad E-ring which peaks in density at the moon's orbit, and supplying nitrogen to the magnetosphere in lieu of Titan, contrary to pre-Cassini assumptions [Smith et al., 2007, 2008].
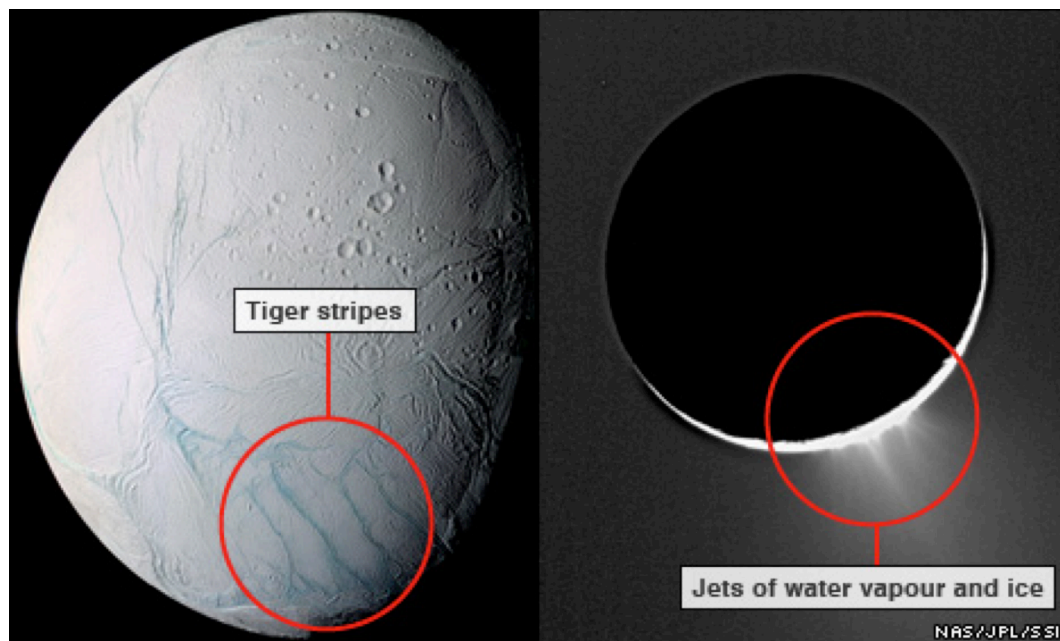
Figure 2.1.4 Enceladus and its plumes

A false-color mosaic of Enceladus' anti-Saturn hemisphere showing the "tiger stripe" features (left) and the moon's ice jets (right) as captured by Cassini's Imaging Science Subsystem in 2005. See pages I–XI for attributions.

14

In 2005 Cassini's Composite Infrared Spectrometer (CIRS) measured an unexpectedly high surface temperature greater than 85 Kelvin at the south pole of Enceladus [Spencer et al., 2006], and the orbiter's Imaging Science Subsystem (ISS) [Porco et al., 2006] and Ultraviolet Imaging Spectrometer (UVIS) [Hansen et al., 2006, 2008] observed ice grains and active water vapor plumes, respectively, spewing from fissure-like features in the same region (a.k.a. the "tiger stripes"). The CIRS measurements showed these emissions to have a temperature of at least 145 Kelvin, indicating hot conditions in the moon's interior, possibly due to some combination radiogenic or tidal heating. While the melting temperature of water ice (~273 Kelvin) is significantly higher than that measured in the plume, traces of ammonia detected in the plume during subsequent flybys in 2008 [Waite et al., 2008] suggest that the compound may act as antifreeze, maintaining liquid water below the moon's crust down to temperatures as low as 173 Kelvin.

Through collisional energy transfer the torus of material ejected from Enceladus flattens and diffuses inward and outward from the moon's orbit. Ions are injected into the magnetosphere through photochemical processes and erosion of icy surfaces by energetic ions and electrons. Thus, even small amounts of trace species like nitrogen imbedded in the water ice can be sourced to regions of the magnetosphere far from Enceladus. These sources—the icy moons and rings—together feed Saturn's corotating plasma, which interacts with Titan and drives atmospheric loss there.

2.2 Magnetospheric structure and dynamics

The magnetosphere of Earth, and those of Saturn and Jupiter, represent opposite extremes in terms of magnetospheric configuration and dynamics. Magnetospheric structure is determined by the balancing of solar wind pressure against internal magnetic pressure and plasma pressure. At Earth's extreme, the solar wind efficiently drives reconnection of magnetic field lines at the subsolar magnetopause and their convection and subsequent reconnection in the magnetotail. This mechanism, known as the Dungey cycle and illustrated in Figure 2.2.1, allows solar wind ions and external electric fields to "map" down open field lines and influence internal dynamics.

Earth's relatively weak magnetic field (~50 μT at the equator) and scarcity of internal plasma sources, aside from its ionosphere, yield a small magnetospheric footprint (~10 R_E mean standoff distance) compared to both Saturn (~216 R_E mean standoff distance) and Jupiter (~825 R_E mean standoff distance). At the other extreme, and at nearly 5 times the distance from the Sun (~484 million km), Jupiter's strong magnetic field (~400 μT at the equator) and numerous internal plasma sources provide great resistance to compression by the diminished solar wind pressure, which falls off roughly as the inverse of the squared distance from the Sun. Thus, while Jupiter's diameter is only 1/10th the diameter of the Sun, it's magnetosphere is many times wider than the Sun and its tail can stretch beyond the orbit of Saturn at ~890 million miles. Meanwhile, although Saturn resides nearly twice as far from the Sun as Jupiter and its magnetosphere is also dominated by internal plasma pressure, its comparatively weak magnetic field (~20 μT at

16

the equator) inhibits the reach of its magnetopause relative to Jupiter's as visualize in

Figure 2.2.2.
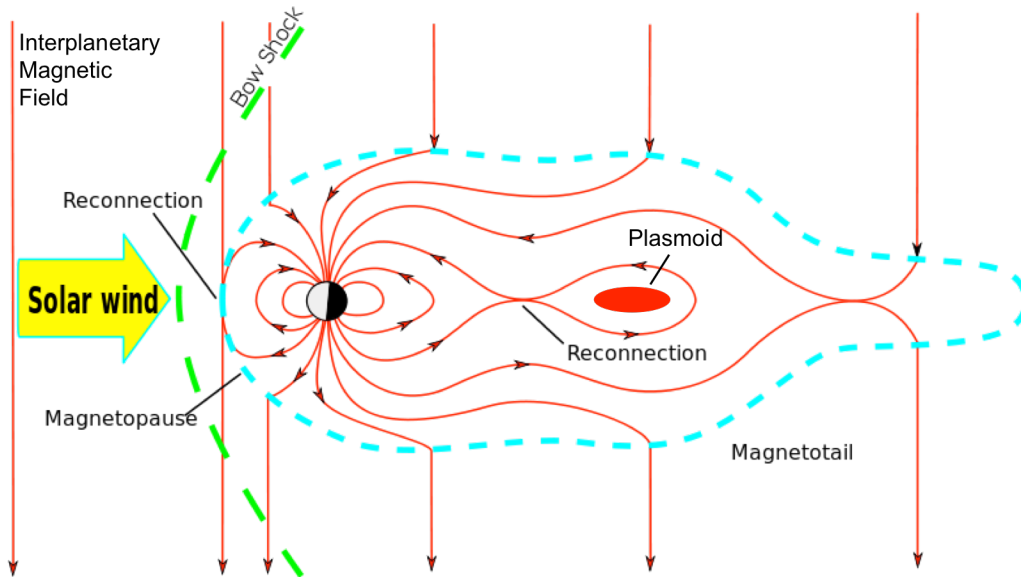
Figure 2.2.1 The Dungey cycle

Carried along by the solar wind, the IMF reconnects with the planet's intrinsic magnetic

field at the subsolar magnetopause. Open field lines convect over the poles toward the

magnetotail where they subsequently close and convect back toward the magnetopause.

See pages I–XI for attributions.

Figure 2.2.3 shows idealized, equatorial cross-sections of the primary electric

potentials driving ion motion inside the magnetopause. The convection potential is

established by interplanetary magnetic field (IMF) lines that do not reconnect but instead

flow around the magnetopause within the magnetosheath. The magnetic field is "frozen"

into the plasma in the Sun's atmosphere; that is, the magnetic Reynolds number there is

much greater than 1 so that the field lines are unable to diffuse *through* the plasma but are

instead advected *by* the plasma [Cravens, 1997]. In the steady state approximation IMF

lines are then carried along streamlines by the solar wind with velocity $\boldsymbol{v}_{sw}$, and

Faraday's law implies that the associated electric field, $\boldsymbol{E}_{IMF} \approx -\boldsymbol{v}_{sw} \times \boldsymbol{B}_{IMF}$, runs

perpendicular to the equipotential surfaces swept out by the field lines [Meyer-Vernet,

2007]. Thus, the field lines flowing to either side of the magnetopause produce a dawn-

to-dusk (with the Sun at noon) potential difference across the magnetosphere that is

illustrated by the left-most panel in Figure 2.2.3 [Cravens, 1997].
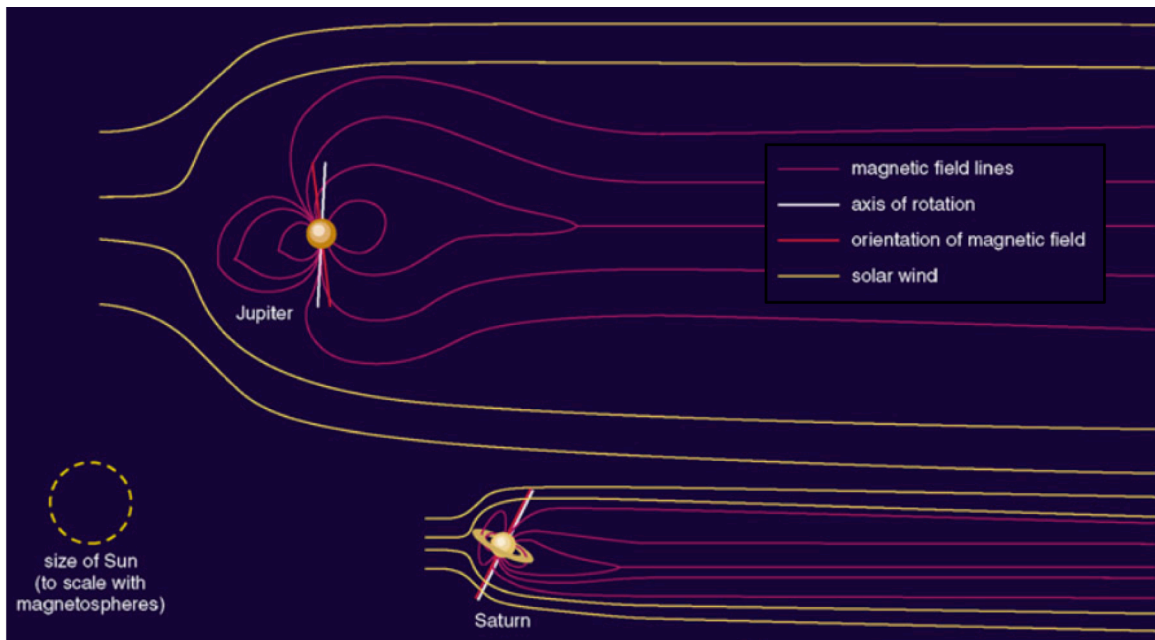
Figure 2.2.2 Magnetosphere size comparison

Sizes of the magnetospheres of Jupiter and Saturn, in cross-section, relative to one

another and to the Sun. See pages I–XI for attributions.

The other primary potential—the corotation potential illustrated in the middle

panel of Figure 2.2.3—arises due to the rotation of the planet's ionosphere. The

ionosphere is collisionally coupled to the planet's neutral atmosphere, which nominally

rotates at the same rate as the planet, with small local deviations due to neutral winds.

This ionospheric current density generates a radial electric field—perpendicular to the

equipotential lines in Figure 2.2.3—in accordance with the generalized Ohm's law

derived from magnetohydrodynamic (MHD) momentum conservation. The strength of

the corotation electric field is proportional to the ionospheric current density and rate of

rotation, and the field in turn drives the rotation of plasma in the inner magnetosphere, or

plasmasphere.
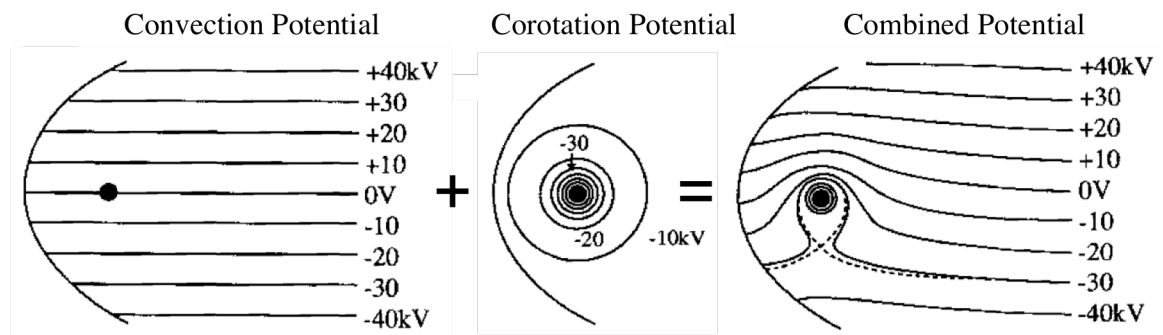
Figure 2.2.3 Magnetospheric electric potentials

Schematic illustrations of the two primary magnetospheric electric potentials (left and

center) and their superposition (right). The figures represent cross sections in the planet's

equatorial plane. See pages I–XI for attributions.

The rightmost panel of Figure 2.2.3 shows the superposition of the convection and

corotation electric fields. Charged particles in the tail and wings of the magnetosphere,

where the electric field is primarily convection-like, experience an $E \times B$ drift

perpendicular to both the electric and magnetic fields that drives them sunward in the

equatorial plane toward the magnetopause. This motion is illustrated schematically on the

left side of Figure 2.2.4. Ions in the inner magnetosphere where the electric field is

primarily radial instead $E \times B$ drift in the direction of magnetic field rotation. In addition,

ions undergo "gradient drift" due to gradients in magnetic field strength and curvature,

resulting in trajectories similar to those induced by $E \times B$ drift but with opposite charges

drifting in opposite directions as illustrated on the right side of Figure 2.2.4. Gradient

drift is most prominent in the inner magnetosphere where field strength gradients are

larger and field line radius of curvature is smaller.
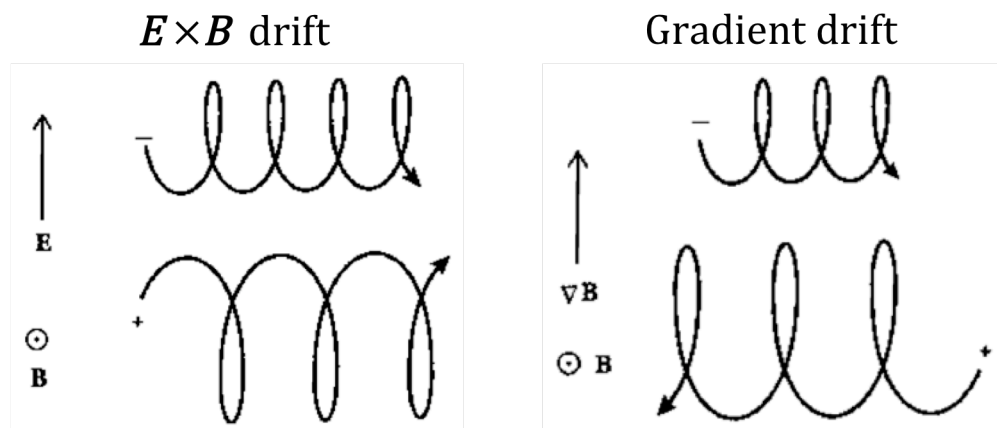
Figure 2.2.4 Charged particle drift motion

The $E \times B$ drift motion of a charged particle in perpendicular electric and magnetic fields

(left) and the grad-B drift of a charged particle in a magnetic field gradient (right). See

pages I–XI for attributions.

The pear-shaped region of closed potential contours on the right-hand side of

Figure 2.2.3 is called the plasmasphere, and the dashed boundary representing the

outermost closed contour is the plasmapause. The plasma within this boundary is relatively dense and cold—of ionospheric origin—and corotates with an angular velocity near that of the planet. Typical energies and densities for this region are a few eV and a few thousand ions per cubic centimeter, respectively. Overlapping with the plasmapause but extending both inward and outward toward the tail, the ring current consists of gradient-drifting hot ions (hundreds of eV to a few keV) injected into the inner magnetosphere from the magnetotail during periods of intense magnetic reconnection. External to the plasmasphere are the equatorial plasma sheet, corresponding to the region between the plasma pause and magnetopause where the electric field is convection-like, and the tail lobe regions above and below the plasma sheet, as illustrated in the cutaway diagram in Figure 2.2.5. In the plasmasheet ion densities are several orders of magnitude lower than in the plasmasphere, but energies of several thousand keV are typical. In the lobe regions densities are lower yet by about an order of magnitude, with somewhat lower energies around 1 keV. [Cravens, 1997]
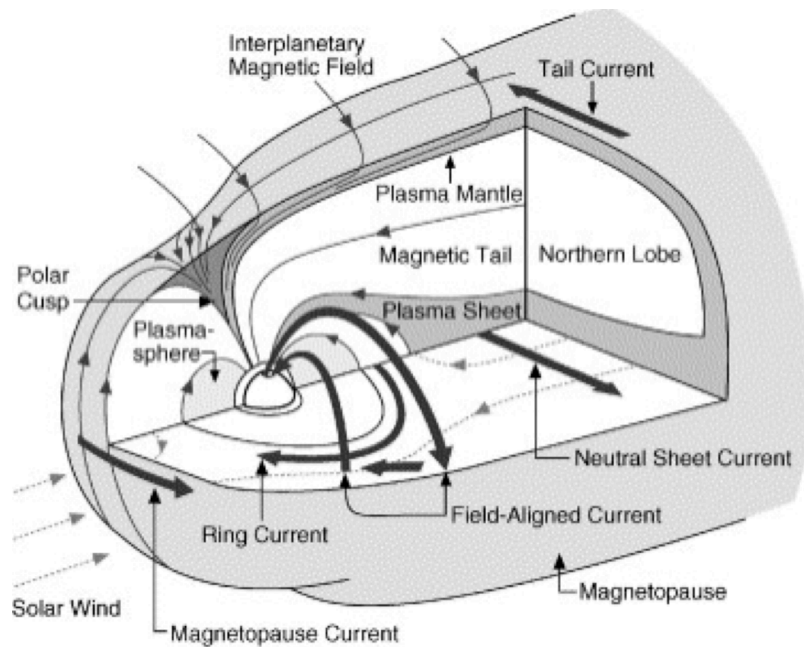
Figure 2.2.5 Magnetospheric regions and currents

A cutaway diagram of an idealized magnetosphere illustrating primary plasma regions and current systems. See pages I–XI for attributions.

Based on the relative strengths of their convection and corotation electric fields, Earth's magnetosphere is said to be solar wind driven while Jupiter's and Saturn's are said to be rotationally driven. In terms of plasma regions this means that Earth's plasma sphere extends only about two-thirds the distance to its magnetopause so that it is flanked on either side by plasma sheet, whereas at Jupiter and Saturn the plasmapause extends nearly all the way to the magnetopause [Mauk et al. 2009]. This is particularly relevant for Titan where, orbiting at ~20 R_S, the moon often straddles the boundary between the corotating edge of the plasmasphere and the plasma sheet, occasionally even moving through the plasmapause into the plasmasheath near noon Saturn Local Time (SLT) where it is bombarded by energetic solar wind ions. Moreover, Titan's orbit alternates between the

22

plasma sheet and tail lobe regions as Saturn's magnetosphere is compressed by the solar wind and the sheet deformed. Figure 2.2.6 illustrates this deformation, as modeled by Arridge et al. [2006]. As discussed below, these changes in environment have important implications for atmospheric loss at Titan.

a)

Current/Plasma Sheet

Ω

M

Distorted
Magnetic Field Lines

Sun

Dipole Magnetic Equator

b)

Current/Plasma Sheet

Titan

Hyperion

Saturn
Spin
Axis

Sun
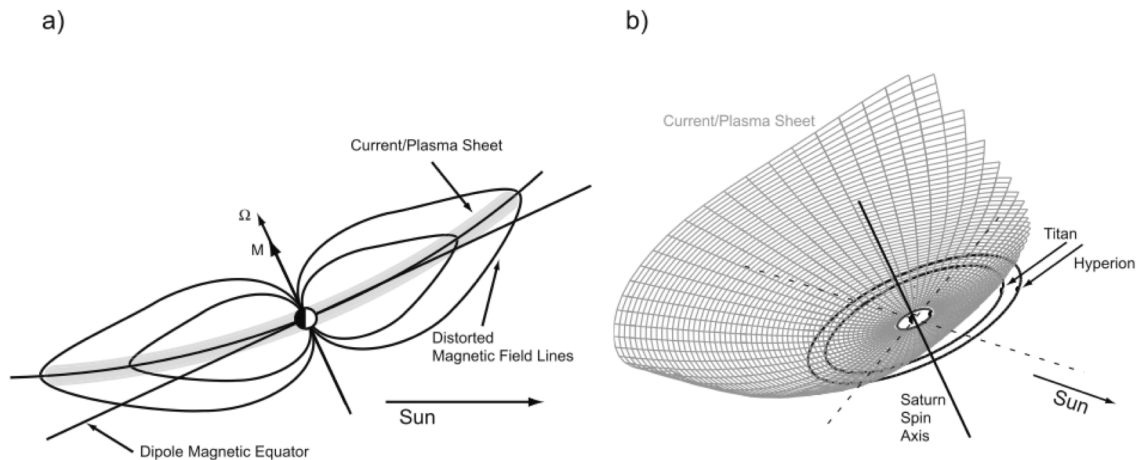
Figure 2.2.6 Saturn's distorted magnetosphere

The solar-wind induced deformation of Saturn's magnetosphere in the noon-midnight meridian (left) and a three-dimensional view of the distorted, bowl-shaped plasma sheet showing Titan's partially imbedded orbit. See pages I–XI for attributions.

2.3 Titan's induced magnetosphere

With a rotation period of ~10.5 hours, Saturn spins nearly 37 times faster than Titan orbits it. Similar to the way in which the IMF piles up in Saturn's bow shock on approach to the magnetopause, Saturn's magnetic field piles up in Titan's "bow shock" as it overtakes the moon. Since Titan has no appreciable magnetic field of its own, this

magnetic pileup is induced entirely by plasma loading as the field lines enter and become mired in the exosphere and ionosphere (due, again, to the high magnetic Reynolds number there). Far from the moon the field continues to rotate with Saturn so that in the vicinity of Titan it stretches and becomes draped around the moon as illustrated schematically in Figure 2.3.1. Moreover, as with the interaction between the solar wind and Saturn's magnetosphere, the convection electric field carried along by the flowing plasma and magnetic field is mapped down magnetic field lines into Titan's ionosphere.

This magnetic field line draping complicates the motions of ions both in the ionosphere and in the near exosphere, and it directs the precipitation of energetic, ionizing electrons into the thermosphere near the moon's poles. Field lines mired in Titan's ionosphere can also be dragged from one magnetospheric environment to another. Bertucci et al. [2008] showed that during the T32 encounter Titan dragged a bundle of Saturn's trapped magnetic field lines outside of the magnetosphere into Saturn's magnetosheath where the orientation of the piled-up IMF is opposite that of Saturn's magnetic field. According to simulations by Ma et al. [2009] it can take up to several hours for these "fossilized" fields to completely vacate the ionosphere. This in addition to the dynamic geometry of Saturn's magnetosphere under varying solar wind and internal plasma conditions results in a near-Titan environment that often diverges drastically from an idealized plasma sheet with a southward magnetic field configuration.
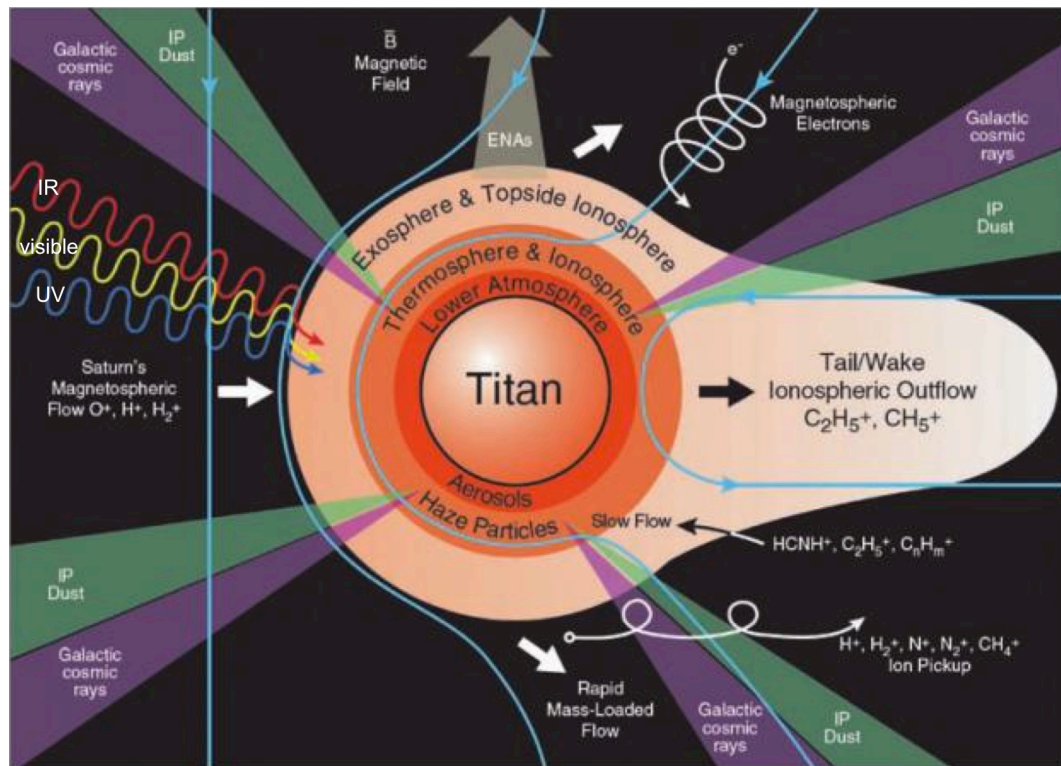
Figure 2.3.1 Titan's induced magnetosphere

A schematic representation of Titan's induced magnetosphere showing energy input

mechanisms and associated atmospheric loss processes. See pages I–XI for attributions.

Rymer et al. [2009], Nemeth et al. [2011], and Simon et al. [2013] have each

demonstrated the variability in Titan's induced magnetosphere based on measurements

from different Cassini instruments over numerous encounters. Rymer et al. [2009] first

analyzed electron energies acquired by the CAPS Electron Spectrometer (ELS) and the

Magnetospheric Imaging Instrument (MIMI) over 54 encounters and discerned four

primary ambient plasma types: three corresponding to Titan's position in the plasma

sheet, lobe, or plasmasheath, and one bimodal type consisting of hot sheet-like or lobe-

like electrons mixed with cold pickup electrons, possibly indicative of freshly-ionized

neutrals. Nemeth et al. [2011] later analyzed ion energies measured by CAPS IMS over the same 54 encounters and found very good agreement with the previous classification, as did Simon et al. [2013] by analyzing magnetometer measurements of the orientation of Saturn's magnetic field over the first 85 encounters. A full characterization of atmospheric loss at Titan thus requires an understanding of loss processes within each of these environments.

2.4 Atmospheric loss at Titan

Unlike every other satellite in the outer solar system, Titan has retained a thick extended atmosphere with a column density ~10 times that of Earth and an atmosphere-to-solid ratio similar to that of Venus. This atmosphere consists of more than 95% N_2 and about 2-3% CH_4 with a mix of H_2 and other minor species. Seasonal variations such as migration of haze layers and shifting circulation patterns are observed to occur in Titan's atmosphere due to the ~27° tilt of Saturn's rotation axis—and thereby Titan's axis—with respect to the Sun. In addition, Saturn's orbital eccentricity yields a variation in solar flux of ~20% between perihelion and aphelion over a solar cycle [Strobel et al., 2009].
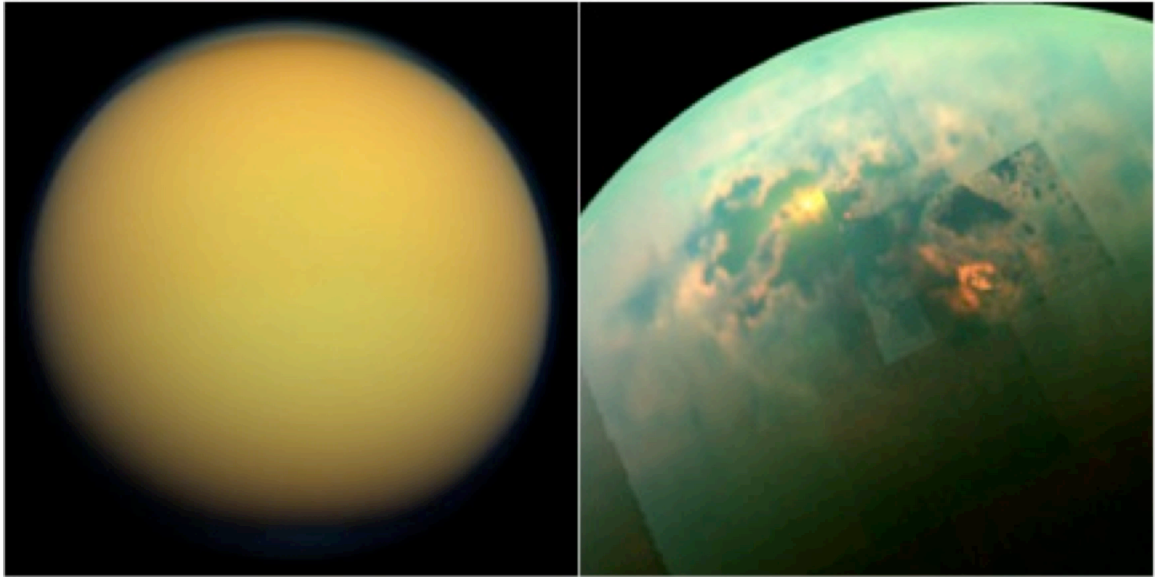
Figure 2.4.1 Titan and its north polar sea

A natural-color photograph of Titan taken by Cassini's Imaging Science Subsystem (left) and a near-infrared color mosaic of sunlight glinting off of Titan's north polar methane-ethane sea, acquired by Cassini's Visual and Infrared Mapping Spectrometer (right). See pages I–XI for attributions.

The maintenance of a stable nitrogen atmosphere on Titan depends critically on the warming effect of its constituent methane. In the absence of solar absorption by methane and its derivative tholin haze, Titan's nitrogen atmosphere would condense and collapse. However, the long-term stability of the atmosphere's methane content is not a certainty. Its meteorological cycle in the troposphere (the lowest layer of the atmosphere) involves at least temporary loss of methane to the interior, and photochemistry in the upper atmosphere and ionosphere, as well as interaction with Saturn's magnetospheric plasma, all lead to the irreversible loss of methane [Atreya et al., 2009]. Based on models of atmospheric loss using present loss rates, Johnson [2004] showed that if Jupiter's

moons Io and Europa ever had similar atmospheres they would have been completely removed by plasma trapped in the Jovian magnetosphere over the lifetime of the solar system. Titan therefore represents a unique and important endpoint in the evolution of planetary atmospheres from which we can better understand the erosion of atmospheres on other planets and satellites.
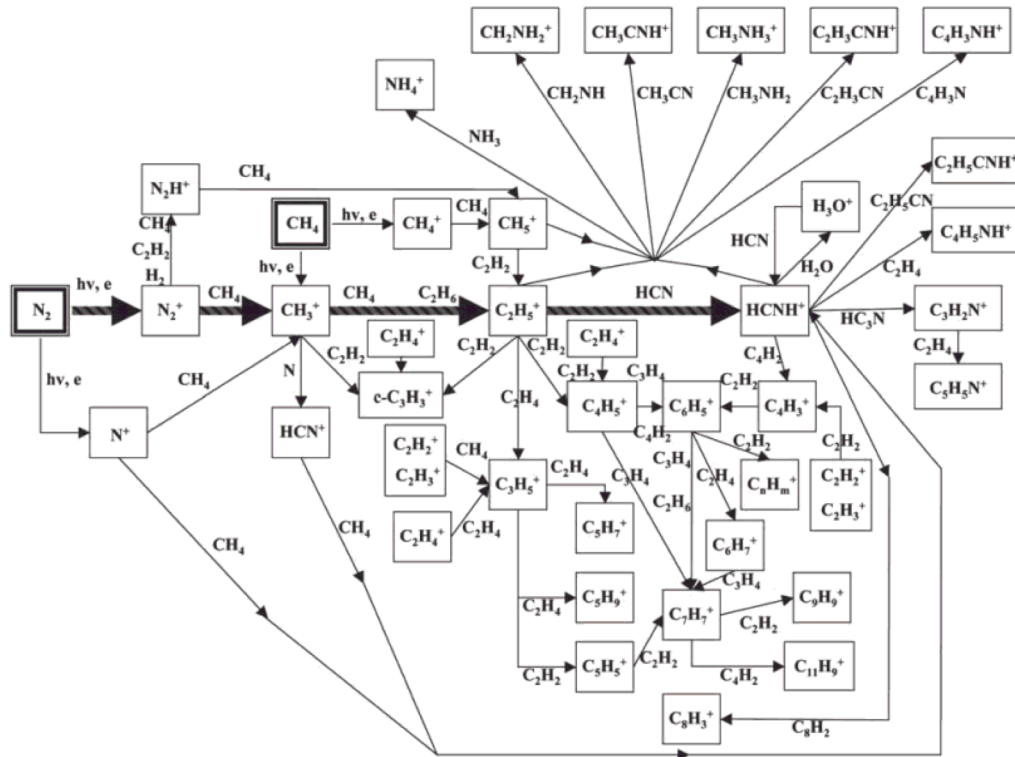
Figure 2.4.2 Chemical pathways in Titan's ionosphere

A simplified chemical network showing primary chemical species and reactions in Titan's ionoshpere. Bold boxes indicate the two most prevalent neutral species and bold arrows indicate their primary reaction pathways. See pages I–XI for attributions.

Titan's neutral thermosphere (the atmospheric region immediately below the exobase) and ionosphere (the ionized component of the thermosphere) form an interface between Saturn's magnetosphere and Titan's lower atmosphere. These layers supply thermalized and energetic neutrals and ions to the magnetosphere via a number of different loss processes which, over billions of years, may have significantly influenced the evolution of Titan's atmosphere. Moreover, the complex molecular products of photo- and ion-neutral chemistry in Titan's upper atmosphere can be transported to the lower atmosphere where they contribute to the formation of haze layers. Figure 2.4.2 illustrates primary chemical pathways in Titan's ionosphere, including those species observed in the CAPS IMS data acquired in Titan's wake, and Figure 2.4.3 offers a simplified schematic of the chemical processes giving rise to the haze.
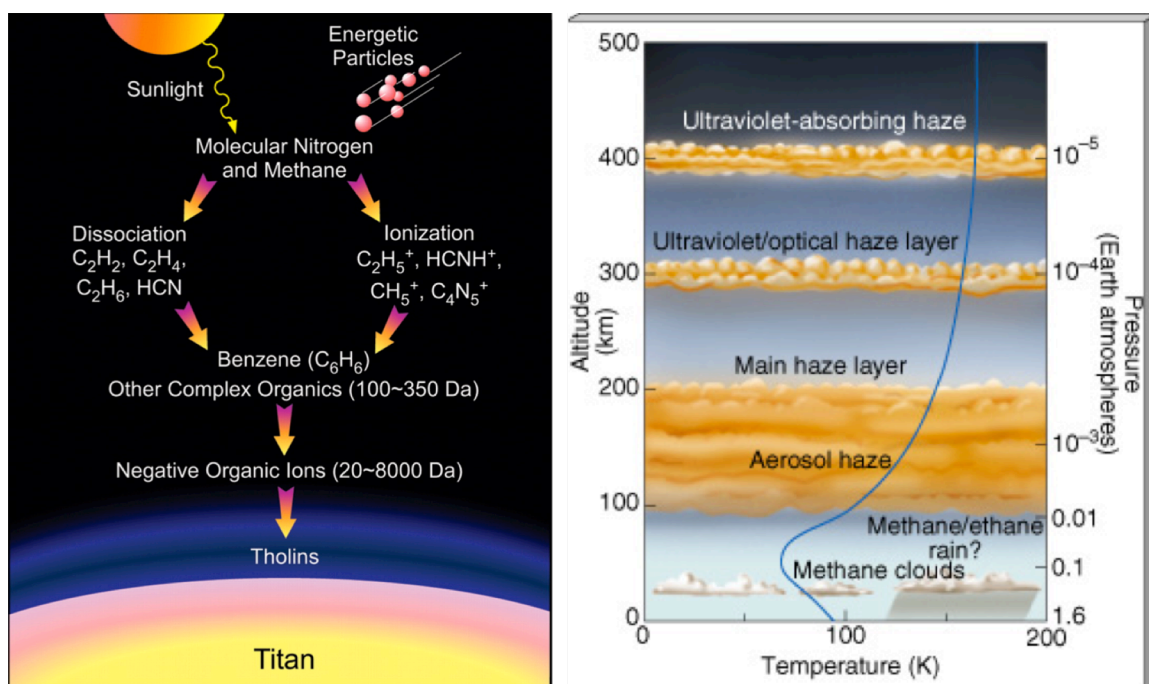
Figure 2.4.3 Haze formation in Titan's atmosphere

Reactions leading to tholin formation in Titan's atmosphere (left) and the resulting haze layers (right). Tholins are large polymers formed from dissociation and recombination of simple organic compounds. See pages I–XI for attributions.

De La Haye et al. [2007] studied INMS data from a number of early Titan encounters and found that observed neutral density profiles in the exosphere could be explained if the energy distribution had a non-thermal, hot component. Based on known exothermic chemistry and available models of plasma-induced sputtering, they concluded that such a distribution requires either transport from below or additional energy deposition near the exobase. In response, Strobel [2008] and Yelle et al. [2008] argued that such an enhancement in the energy tail is supplied by collisional heating from hydrodynamically escaping molecules, and that nonthermal mechanisms (e.g. plasma-

induced escape) are not necessary to account for anticipated loss rates. To show this, Yelle et al. [2008] analyzed methane and argon mole fractions versus altitude as measured by the Huygens probe during it's decent through Titan's atmosphere and concluded that the observed mixing ratio was most likely explained by a substantial upward escape flux. In agreement, Strobel [2008] found that he could match the temperature and density profiles measured by the probe with a hydrodynamic model incorporating solar heating, in which escape is driven by slow adiabatic expansion due to EUV/UV absorption and emissive cooling throughout the atmosphere.

Cui et al. [2008] modeled the viscous energy loss to heavy background molecules implied by such a hydrodynamic model using a 13-moment approximation to the Boltzmann equation, which can in principle produce a Maxwellian with an enhanced tail for the heavy molecules. What they found, however, is that the viscous heating is insufficient to drive the outflow of heavy molecules, and that the H_2 velocity distribution is actually enhanced by *extracting* energy from the heavy molecules. Perhaps more importantly, the atmosphere above the exobase cannot be treated as a fluid since, by definition, it is no longer collisional there. Thus, an atomistic model of interactions in the exosphere is needed to bridge the gap between the two regimes. Tucker and Johnson [2009] used a direct simulation Monte Carlo (DSMC) code to model the kinetics of an N_2 + CH_4 atmosphere above the exobase using temperature, density, and heat flux boundary conditions determined from the analyses of Strobel [2008] and Yelle [2008] at the exobase. They found that the hydrodynamic model, when extended above the exobase,

31

overestimate the N_2 and CH_4 escape rates by orders of magnitude, suggesting non-thermal mechanisms are likely still relevant.

Furthermore, De La Haye et al. [2007] used plasma-induced sputtering and energy deposition rates simulated by Michael et al. [2005] and Michael and Johnson [2005], respectively, to conclude that the magnetosphere-ionosphere interaction is likely more important than pre-Cassini estimates suggested, as supported by IMS measurements of low-energy ions in the corona near the exobase. Such ions, probably associated with pick-up near the exobase and/or ionospheric outflow, can efficiently heat the atmosphere near the exobase via long-range ion-neutral interactions. Their inferred loss rates suggest that plasma-induced heating and sputtering may in fact be the leading loss mechanism for atmospheric methane and nitrogen after photochemical destruction, and the primary mechanism of permanent loss to the magnetosphere. It is therefore essential to establish abundances and energy distributions of heavy-ion populations near Titan—the focus of my doctoral work— so that both ion and neutral escape rates and thereby overall atmospheric loss can be accurately determined for the various magnetospheric environments that Titan encounters.

3. T40 Titan encounter data analysis

The following chapter is an adaptation of the material presented in

Woodson, A. K., Smith, H. T., Crary, F. J., & Johnson, R. E. (2014). Ion composition in Titan's exosphere via the Cassini Plasma Spectrometer I: T40 encounter. *Journal of Geophysical Research: Space Physics*.

3.1 Background

Prior to the Cassini mission there was considerable speculation about the extent to which Saturn's magnetospheric plasma interacts with Titan's upper atmosphere. Models based on Voyager data suggested that escape rates for nitrogen and carbon species were small (5×10^{26} amu/s) relative to the hydrogen escape rate (1–3×10^{28} amu/s) and that sputtering by magnetospheric N^+ and heavy molecular pickup ions contributed more to escape than did solar radiation [Michael et al., 2005; Michael and Johnson, 2005]. Moreover, Shematovich et al. [2003] and Smith et al. [2004] showed sputtered nitrogen to be the primary source for the anticipated neutral torus at Titan's orbit. However, subsequent analysis and modeling of Titan's thermosphere and corona by Yelle et al. [2008] and Strobel [2008], based on data acquired by Cassini's Ion and Neutral Mass Spectrometer (INMS) and the Huygens Atmospheric Structure Instrument, led to substantially larger estimates for the loss of heavy molecules (0.3–5×10^{28} amu/s) via hydrodynamic escape as opposed to plasma-induced escape. Meanwhile, De La Haye et

al. [2007] analyzed the energy distribution of the neutral atmosphere between 1200 and 2000 km, as measured by INMS, and found that precipitation of heavy, low-energy ions near the exobase can produce the nonthermal enhancement of the neutral energy distribution observed above the exobase, leading to escape rates of the same magnitude as those proposed by Yelle et al. [2007] and Strobel [2008].

At the highest rates suggested, Titan would have lost a significant portion of its present atmosphere over the lifetime of the solar system [Johnson et al., 2009]. In addition, evidence of the neutral nitrogen torus at Titan's orbit has been elusive [Smith et al., 2005, 2007] and Cassini has shown the degree of interaction between Titan's atmosphere and the ambient plasma to be highly variable [Rymer et al., 2009; Nemeth et al., 2011; Simon et al., 2013]. As such, the extent to which this interaction drives escape, precipitation and heavy-molecule formation, and the relative importance of those processes in regard to Titan's evolution, is still debated. Herein we analyze the composition of ions in Titan's wake during the T40 encounter so that we might better understand the nature of the interaction.

The Cassini spacecraft has now flown within a few thousand kilometers of Titan over 100 times since its 2004 orbital insertion, and the Ion Mass Spectrometer (IMS)—one of three instruments composing the Cassini Plasma Spectrometer (CAPS)—has acquired usable ion composition data during ~75 of those encounters. While CAPS science has contributed significantly to our understanding of the Kronian system, few

studies have been carried out to extract detailed compositional information from the wealth of data acquired by IMS near Titan.

The majority of CAPS IMS data analysis found in the literature focuses on calculating the moments of ion distributions in regions of the magnetosphere far from Titan. This is generally done in one of two ways. The first involves direct integration of total ion counts over a partially sampled velocity distribution that is filled in by assuming symmetry in the reference frame of the flowing plasma [Sittler et al., 2005; Thomsen and Delapp, 2005; Sittler et al., 2006; Thomsen et al., 2010; Szego et al., 2011; and Szego et al., 2012]. The second method fits either isotropic or anisotropic Maxwell distributions to energy- and angle-discriminated ion counts in order to extract moments from the fit parameters [Tokar et al., 2005 and 2006; Hill et al., 2008; Wilson et al., 2008; McAndrews et al., 2009; and Elrod et al., 2012]. In all of these cases the mass spectra are used primarily to determine relative abundances of H^+, H_2^+, He^{++} and the broad water group peak—consisting of unresolved O^+, OH^+, H_2O^+, and H_3O^+—in order to partition the total ion counts for moment calculations. One exception is the analysis of Martens et al. [2008] in which careful background- and peak-fitting was used to isolate O_2^+ from the rest of the broad water group peak in IMS spectra summed over 23 orbits.

A handful of studies have identified species outside of the light group and water group through visual inspection and model peak fitting of IMS mass spectra. Hartle et al. [2006a, 2006b] compared CAPS ion and electron measurements from the first Titan encounter with those made by Voyager 1 during a similar encounter in 1980. Although

individual abundances were not determined, they identified H^+, H_2^+, and a group

consisting of N^+/CH_2^+–CH_4^+ ions based on visual inspection of four different time-

integrated mass spectra. Smith et al. [2005, 2007] fitted a peak model based on

instrument calibration data to energy-discriminated mass spectra acquired between ~3.5

and ~13.5 Saturn radii to verify the presence of N^+ in Saturn's magnetosphere and its

abundance relative to the water group. Smith et al. [2008] then expanded the peak fitting

to determine whether ammonia or N_2^+ from Enceladus act as the parent molecules for the

observed N^+. By simultaneously fitting peaks for NH^+, NH_2^+, NH_3^+, NH_4^+ and N_2^+, as

well as an assortment of overlapping carbon- and oxygen-bearing species, they were able

to put upper limits on the relative amounts of molecular nitrogen and ammonia products

sourced from Enceladus. Sittler et al. [2010] performed a thorough decomposition on

IMS mass spectra acquired in Titan's wake during the T9 Titan encounter, for which they

fitted model peaks based on calibration data and determined abundances for H^+, H_2^+,

CH_3^+, CH_4^+, CH_5^+, NH_4^+, $HCNH^+$, and $C_2H_5^+$. In addition, they used their fitted

abundances to weight total ion counts and calculate ion moments for masses 1, 2, 17, and

29 amu/q, where q is the fundamental charge of the proton. Lastly, Coates et al. [2012]

analyzed Titan encounters T9, T63 and T75 and reported densities and velocities for

mass-to-charge values of 1, 2, 16, and 28 amu/q in regions where ionospheric outflow

was detected. Velocities were estimated by fitting 1-D Maxwell distributions to a subset

of the energy-discriminated ion counts, while densities for individual species were

determined by normalizing the associated mass peaks against the integrated distributions.

While I employ a different modeling technique, the thrust of my analysis follows
that of Smith et al. [2008] and Sittler et al. [2010]. In particular I have extracted relative
ion-group "fluences" (i.e., the number of ions entering IMS per 256-second collection
cycle) from CAPS IMS spectra acquired during the T40 encounter by fitting peak
functions derived from instrument calibration data, where I have based my range of fitted
mass peaks on the composition measured by INMS during the same encounter [Westlake
et al., 2012]. After sampling near ~1497 km INMS captured Titan's ionospheric outflow
on egress between ~2225 and ~3034 km due to a serendipitous reorientation of the
spacecraft. According to Westlake (personal correspondence, 2014) this is the only such
high-altitude ion measurement made by INMS for which concurrent IMS data exists,
providing amu-resolved ion densities in the mass-to-charge (M/Q) range covered by
CAPS IMS and within a complementary range of altitudes. In this analysis I refer to the
reported INMS composition to select model peaks for seven consecutive time- and
energy-integrated IMS mass spectra acquired during T40 ingress between ~2733 and
~12,541 km. Based on these fits I investigate changes in composition as a function of
spacecraft position. In addition, I present energy profiles and estimated velocities and
densities for the ion groups measured along the spacecraft trajectory.

3.2. Instruments

Cassini carries two mass spectrometers designed for optimal sampling in different
regions of Saturn's magnetosphere. INMS was devised primarily to gather data on the
composition, density and temperature of Titan's upper neutral atmosphere and ionosphere

while CAPS, including IMS, was designed to characterize hot diffuse plasmas throughout Saturn's magnetosphere. Extended specifications for CAPS IMS and INMS can be found in Young et al. [2004] and Waite et al. [2004], respectively. CAPS IMS will be described in fair detail here, as its operation is relevant to both the data analysis and the experimental work presented in Appendix A. For INMS, only characteristics relevant to the data analysis will be summarized here.

A schematic cross-section along the IMS axis of symmetry is shown in Figure 3.2.1. The IMS entrance collimator is divided into eight sectors each spanning 20° about the axis of symmetry. At the top of the figure, positive ions entering the Electrostatic Analyzer (ESA) through one of the eight sectors are selected or rejected based on their energy per charge (E/Q). The ESA is composed of concentric toroidal electrodes with a gap in between, such that a difference in voltage across the gap drives negative ions toward the outer electrode and positive ions toward the inner electrode. Thus, in order to clear the analyzer a positive ion's centripetal motion, determined by the centripetal force on the ion in the electric field between the electrodes, must match the curvature of the electrodes. An accepted ion is then accelerated by ~15 keV through a thin (~10 nm) carbon foil into the linear electric field (LEF) region below. Figure 3.2.2 indicates the arrangement of the carbon foils about the IMS axis of symmetry, where each carbon foil is located directly above a "Start MCP Anode" as labeled in the figure.
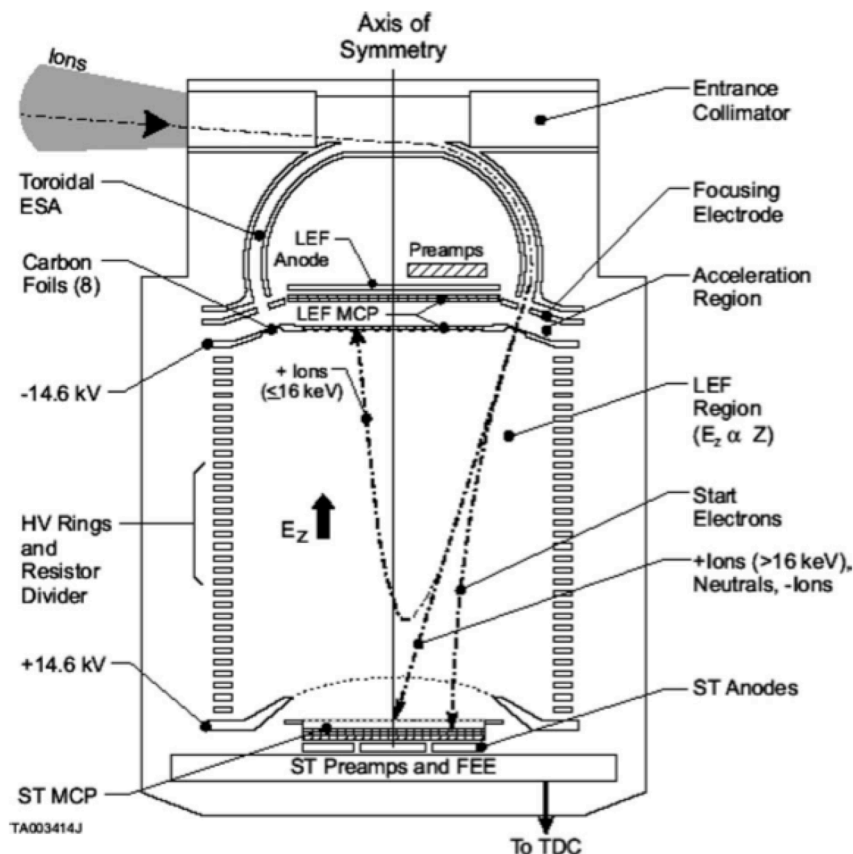
Figure 3.2.1 CAPS Ion Mass Spectrometer

Schematic diagram of IMS optics and detectors showing idealized ion and electron trajectories through the toroidal electrostatic analyzer (ESA) and within the linear electric field (LEF) region. See pages I–XI for attributions.

Molecular ions dissociate completely upon impact with the foil and each ion fragment exits the foil in a positive, negative, or neutral charge state with some associated probability. To detect these fragments, the IMS employs two microchannel plate detectors situated in a charge-separating electric field: an "LEF" detector that collects the reflected positive ion fragments and a "straight-through" or "ST" detector that collects

negative and neutral fragments as well as electrons emitted from the foils by the incident ions. Figure 3.2.2 shows the extent of each detector in cross-section. Each MCP is a semiconducting lead-glass disk etched with channels a few microns in diameter. Placing a suitable voltage across the disk drives a current in the channel walls such that each channel acts as a charge multiplier, producing a cascade of secondary electrons when struck by an incident particle with sufficient energy. The emerging cloud of electrons is then collected on anodes below the MCP. In the case of the ST MCP, a central anode collects the electron cascades produced by neutral and negative ion fragments, which are steered by the LEF toward the center or "stop" region of the ST MCP. Meanwhile, 8 sector-shaped anodes arranged about the central anode, as illustrated in Figure 3.2.2, gather the cascades induced by carbon foil electrons incident on the outer edge of the ST MCP, providing information about the angular distribution of the incoming molecular ions.

Figure 3.2.2 title, located below figure:

TA3414SS
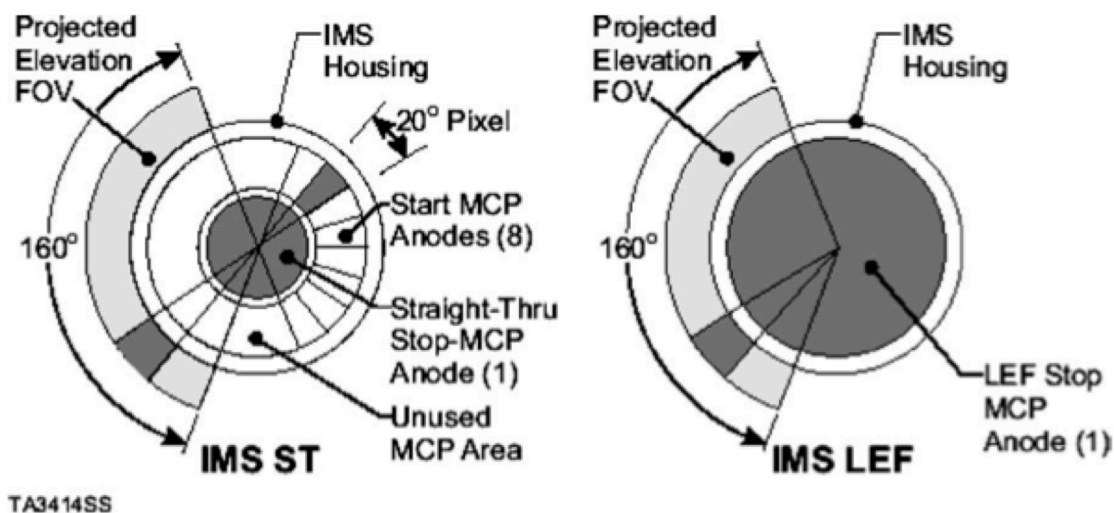
Figure 3.2.2 CAPS IMS detector arrangement

Schematic cross-sections through the IMS axis of symmetry showing the ST and LEF

detector layouts. Each of the eight anodes below the outer edge of the ST microchannel

plate (MCP) maps to the opposing sector of the entrance collimator's field of view (FOV)

as illustrated in the left panel. See pages I–XI for attributions.

      Electrons emitted from a foil by an incident ion are steered almost instantaneously

(relative to the ion fragments) through the LEF onto the ST detector where they trigger a

time-of-flight (TOF) clock for the parent ion fragments. The subsequent arrival of any

one of the ion fragments at the ST or LEF detector stops the TOF clock for the parent ion.

The selected E/Q and fragment TOF, combined with calibration data and an assumption

about the charge state of the initial ion, allow identification of the parent molecular ion in

the case of an ST detection, and of the ion fragment in the case of an LEF detection. Due

to the time-focusing nature of the LEF, the mass resolution for positive ion fragments is

optimized ($m/\Delta m \approx 60$) and the TOF for a given fragment is independent (to first order)

of its energy and the angle with which it exits the foil. The resolution for the ST detector, however, is degraded by path length differences arising from energy straggling within the foils and variation in fragment exit angle. Moreover, the efficiency of the LEF detector is ~20 times lower than that of the ST detector due to design limitations. Thus, while useful for identifying the presence or absence of ions, LEF spectra are too sparse for peak fitting unless summed over many collection cycles.

In contrast, even the best mass resolution of IMS is significantly lower than that of INMS, which is nominally capable of discriminating masses from 1–8 and 12–99 amu with very high resolution ($m/\Delta m = 10^6$). INMS also employs two different apertures to separately collect and analyze nonreactive neutrals and reactive neutrals and ions. Just beyond the ion aperture are four deflection plates and a switching lens that can be used to steer incident ions with energies up to 100 eV into a quadrupole spectrometer for Q/M analysis. In general, the comparably low mass resolution of IMS results in broad, overlapping mass peaks that cannot be isolated without either a priori knowledge of the composition or accurate peak-shape calibrations. In this study, therefore, INMS spectra acquired during the T40 encounter are consulted to select the range of mass peaks used to fit the IMS data.

In terms of its field of view (FOV) and energy range CAPS IMS provides much greater coverage than INMS. The INMS FOV is fixed with respect to the spacecraft and its ion aperture is highly restricted, subtending a ~9° half-angle. The CAPS sensors, on the other hand, are arranged on a platform that actuates back and forth through 208° at a

rate of ~1° per second. Each sector of the IMS entrance collimator subtends 20° parallel to the axis of rotation and 8° perpendicular to it, providing a 160°×8° FOV in any given orientation. Thus, when actuating fully the IMS FOV sweeps almost half the sky in less than three minutes. Moreover, the IMS energy range extends from 0 to ~50,000 eV—two and a half orders of magnitude higher than INMS—with a resolution $r_E = \Delta E/E \approx 17\%$, yielding a more complete picture of ion velocity distributions than INMS can provide.

3.3 T40 encounter geometry

Cassini's T40 encounter with Titan took place on January 5th, 2008 in the 12:00 SLT quadrant where Saturn's magnetosheath is closest to Titan. While Cassini was within ~10 Titan radii (R_T) of the moon's surface, both Saturn's position with respect to Titan and Titan's velocity vector varied by less than 3°. I therefore take the averages of these vectors to define the X- and Y-axes presented in Figure 3.3.1, with the Z-axis completing the right-handed system. Cassini approached on Titan's Saturn-facing night side, crossed the solar terminator into the sun-lit hemisphere at ~21:17:31 UTC, and entered Titan's thermosphere through the nominal exobase (1500 km) at ~21:25:03 UTC. Closest approach (CA) occurred at ~21:30:19 UTC at an altitude of ~1014 km and Cassini subsequently exited the thermosphere at ~21:35:35 UTC. I have calculated all ephemerides appearing in this thesis using the C_SPICE toolkit developed by NASA's Navigation and Ancillary Information Facility along with Cassini-specific SPICE kernel files listed at http://www-pw.physics.uiowa.edu/~jbg/kernels.txt.
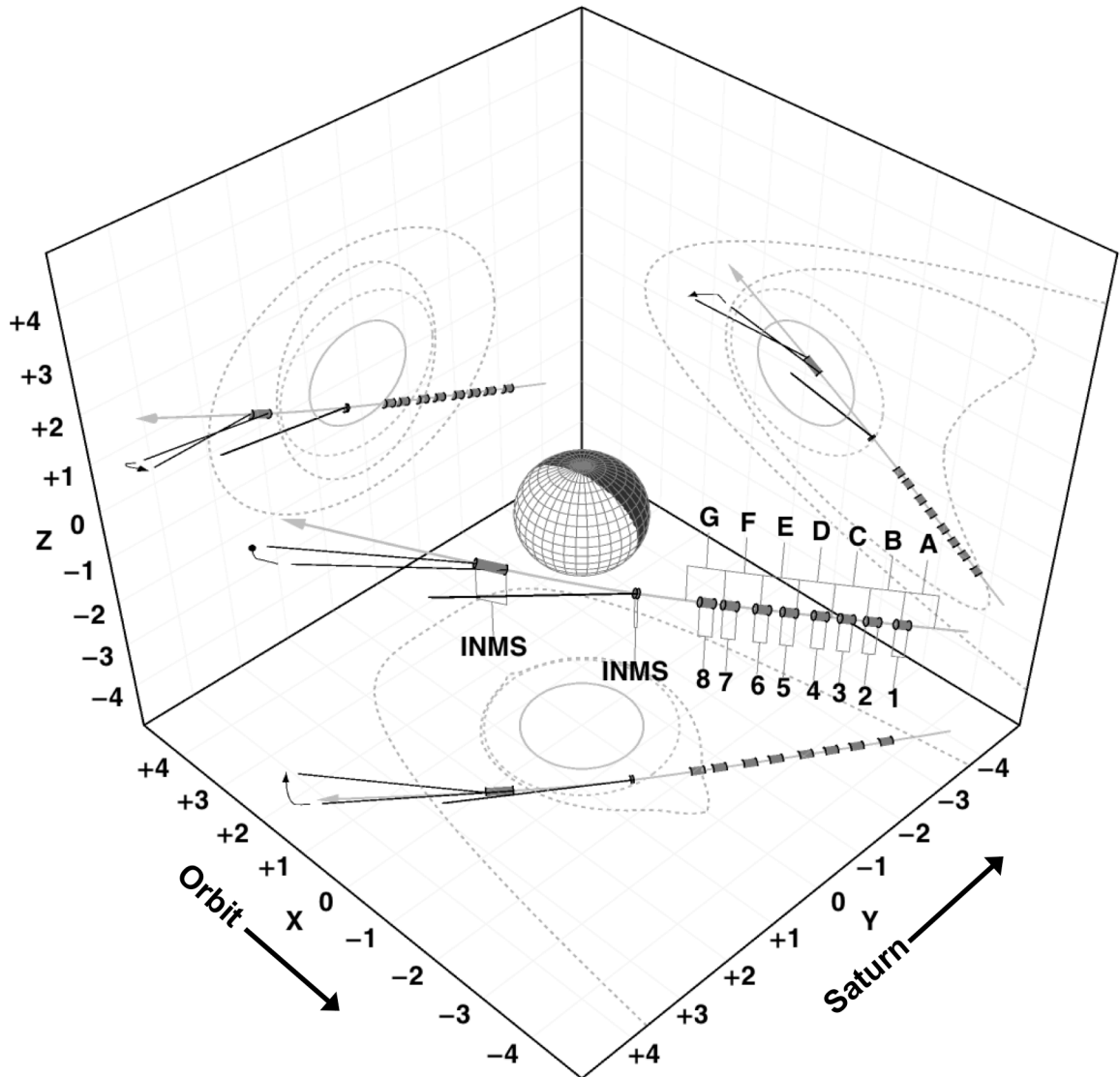
Figure 3.3.1 T40 encounter geometry

A plot of ephemeris data for the T40 encounter showing Cassini's trajectory with respect to Titan, INMS measurement intervals and associated pointing, and IMS B-cycles (letters) and A-cycles (numbers) during which ion counts peaked. Dashed lines, from outside to inside, represent the field-draping and mass-loading boundaries from Ulusen et al. [2012] and the nominal exobase. All dashed boundaries are projections of planar cross-sections through the origin. See pages I–XI for attributions.

3.4. T40 environmental conditions

Based on the analysis of Ulusen et al. [2012], dashed black contours in Figure 3.3.1 represent planar cross-sections of two boundaries that delineate Titan's interaction region. I have graphically extracted these boundaries from the paper cited and scaled them to fit several plots presented in this thesis. These cross-sections correspond to slices through the origin but I have projected them onto the perimeter in Figure 3.3.1 to prevent visual clutter. The outermost contour indicates the boundary where the simulated magnetic field strength is 20% greater than its upstream value. In other words, it is the boundary where field line draping (i.e. magnetic pileup) becomes significant according to the authors. Progressing inward, the second contour represents the boundary where the simulated bulk plasma velocity drops sharply from ~30 km/s to 1 km/s due to mass loading and ion-neutral collisions. These boundaries have been reprinted here for reference because environmental conditions during the T40 encounter were similar to conditions during the 9 encounters analyzed in Ulusen et al. [2012].

The boundaries are derived from a pure MHD simulation of Titan's interaction with the plasma sheet at 12:00 SLT, and the authors show that their results compare favorably with ion, electron, and magnetic field data gathered by Cassini between ~3.5 and ~1.7 Titan radii (R_T). Like the T40 encounter, the 9 encounters used for comparison all occurred in the noon SLT quadrant, demonstrate plasma corotation speeds in the vicinity of 120 km/s, and exhibit magnetic field signatures consistent with that of the plasma sheet as classified by Simon et al. [2013]. While the same study characterizes T40

as "sheet-like" only on egress and "unclassified" on ingress, Rymer et al. [2009] also report brief appearances of sheet-like (high energy and high density) electron populations embedded in a primarily "lobe-like" (high energy and low density) encounter. Despite this fragmented sheet-like signature I show in Section 3.10 that the appearance of the medium-mass group (12–19 amu) in the TOF spectra coincides well with the crossing of the field-draping boundary on ingress.

As a final check on the T40 environmental conditions I examined the solar wind dynamic pressure and associated magnetopause standoff to verify that Titan was neither in nor near the magnetopause during the encounter. Wei et al. [2011] used an MHD code to predict the solar wind dynamic pressure at Saturn for roughly the first half of 2008, including encounters T40 through T44. Although they did not explicitly analyze T40, careful inspection of their Figure 8 suggests a solar wind pressure well within the range 0.0015–0.0045 nPa throughout the encounter. Using the model developed by Arridge et al. [2006] I calculated the contour of Saturn's magnetopause at both ends of this pressure range and found Titan comfortably within the magnetosphere at least 10 Saturn radii (R_S) from the magnetopause at ~11:37 SLT. Although a more recent model by Kanani et al. [2010] improves upon the magnetopause model used here through a more detailed balancing of internal and external pressures, the difference appears primarily in the flaring of the magnetopause about it's axis and is not appreciable for the subsolar standoff distance near 12:00 SLT. Thus the Arridge et al. [2006] model is equally applicable for my study. In agreement with this observation, neither Simon et al. [2013] nor Rymer et al. [2009] report magnetosheath signatures during the T40 encounter.
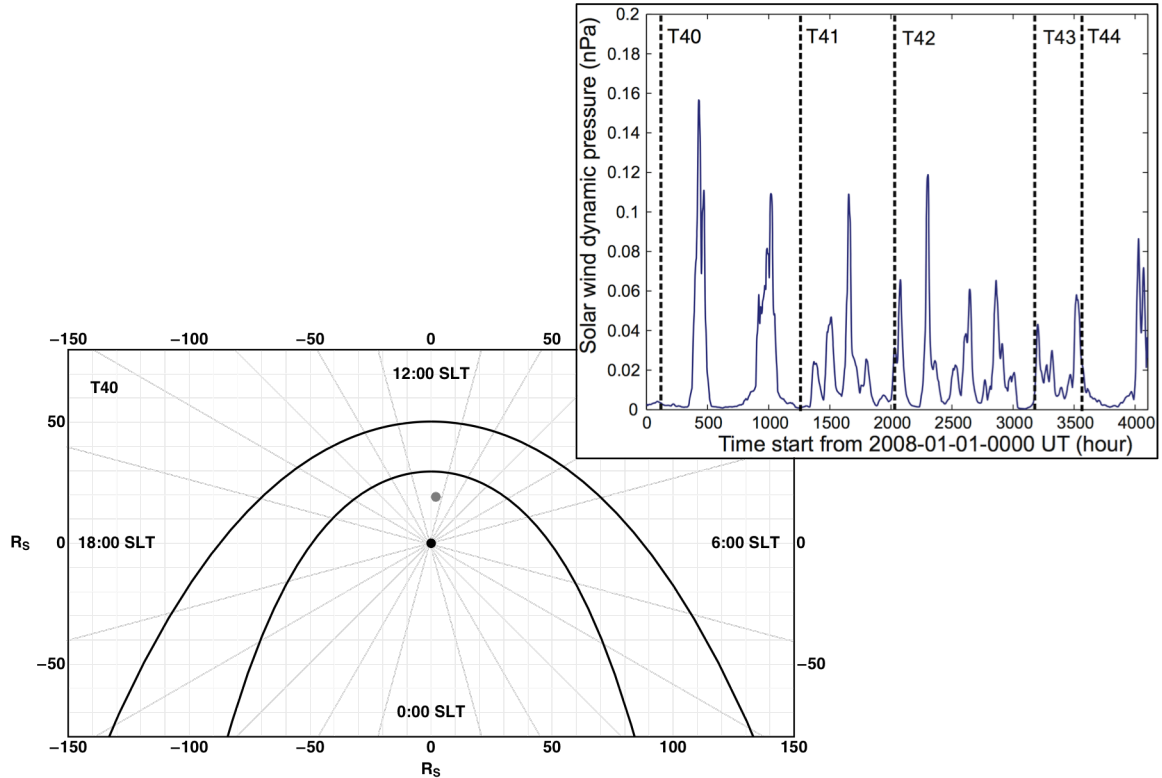
Figure 3.4.1 T40 magnetopause standoff

A plot of solar wind pressure at Titan's orbit (top right) for roughly the first half of 2008, and another plot (bottom left) showing the magnetopause standoff during T40. In the lower plot the black dot represents Saturn, the gray one represents Titan, and the thick black curves indicate upper and lower bounds on the standoff distance due to the uncertainty in the solar wind pressure extracted from the upper plot. See pages I–XI for attributions.

3.5 T40 INMS measurements

As explained by Westlake et al. [2012], INMS observed elevated ion counts during the T40 encounter both near the exobase at ~1497 km and on egress at altitudes between ~2225 and ~3034 km, with an intermediate gap in coverage due to a scheduled calibration scan. The compositional similarities between their low- and high-altitude spectra suggest that hydrocarbons in the range 12–42 amu are being transported from Titan's ionosphere into the wake, and the authors contend that chemical time scales and reaction pathways further support this assertion. At densities found near the exobase the time to generate terminal ions such as CH_5^+, $HCNH^+$, and $C_2H_5^+$ is ~2 orders of magnitude greater than the time required for them to reach the high-altitude region given the observed energies. Moreover, the production of these terminal ions requires multi-step reactions that are unlikely at the observed high-altitude densities.

Figure 3.5.1 (their Figure 4.3) shows that the CH_3^+, CH_4^+, CH_5^+, $HCNH^+$, $C_2H_5^+$, $C_2H_3^+$, $C_3H_3^+$ and $C_3H_5^+$ densities integrated over the entire high-altitude region are of similar magnitude to those sampled near the exobase, while the integrated H_2^+ densities are at least an order of magnitude larger. Moreover, mass groups 24–31 amu and 38–42 amu appear to decline in density more quickly with increasing altitude than mass group 12–19. In Figure 3.9.8 below I compare our ion-group velocity and density estimates with those calculated by Westlake et al. [2012].
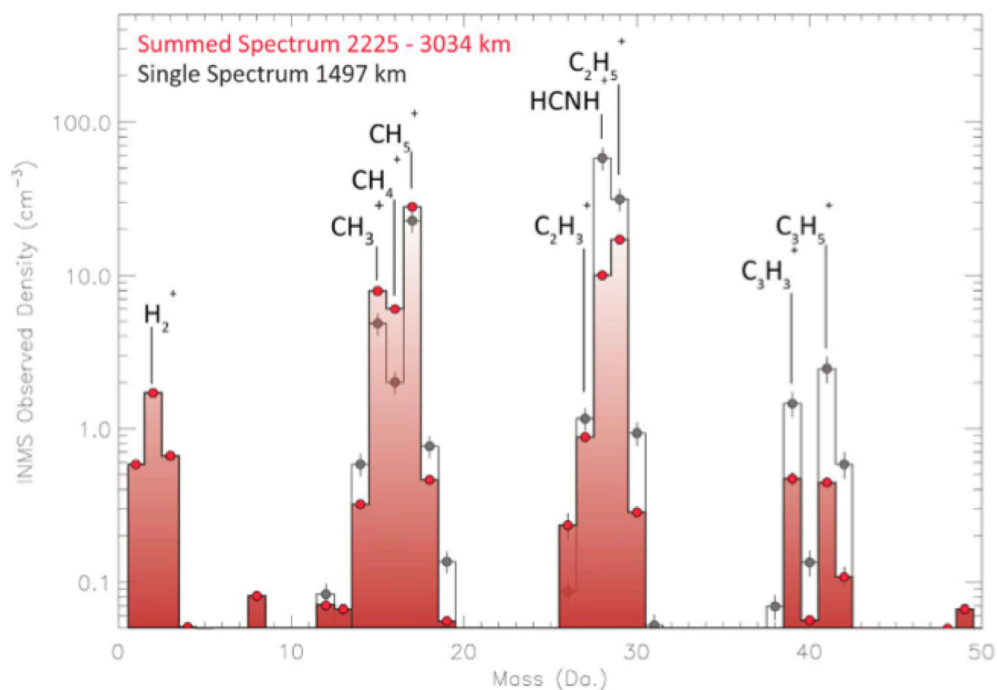
Figure 3.5.1 T40 INMS ion composition

Ion composition measured by INMS near the exobase (single spectrum) and integrated

between 2225 and 3034 km altitude on egress. See pages I–XI for attributions.

The authors also note that some amount of mass 28 is likely to be associated with

N_2^+, which INMS cannot distinguish from $HCNH^+$. However, the N_2^+ signal is closely

related to that of N^+, both of which are produced through photoionization of neutral N_2.

Given the low count rate for mass 14, they argue, the N_2^+ contribution to mass 28 must be

at least an order of magnitude less than what is measured, indicating that the majority of

the mass 28 counts are attributed to $HCNH^+$ which is relatively long-lived in Titan's

ionosphere. Likewise the NH_x^+ group overlaps with CH_x^+, and the CNH_x^+ and $N_2H_x^+$

groups overlap with $C_2H_x^+$ in the IMS ST spectra, making them indistinguishable from

one another. However, the NH_x^+ group is well separated in the IMS LEF spectra, as

labeled in Figure 3.7.3 below. Based on the scarcity of counts in those channels relative to the rest of the LEF spectrum a similar argument can be made for the absence of NH_x^+ and $N_2H_x^+$ in the sampled region, leading to my assertion that hydrocarbons dominate the ion composition in the T40 wake.

3.6 IMS data interpretation

IMS accumulates two types of ion data: ion counts per ST "start" anode, per ESA energy step; and ion counts per "stop" anode (ST or LEF), per each of 2048 TOF channels, per ESA energy step. The former counts are called "singles" or "SNG" counts and track the total number of ions passing through the carbon foils, while the latter are called "TOF" counts and comprise the mass-per-charge (M/Q) discriminated spectra from which ion composition is extracted. Moreover, SNG and TOF counts are accumulated over different lengths of time. The ESA sweeps through 63 logarithmically spaced voltage levels plus 1 "flyback" step every 4 seconds, lingering at each voltage level for $1/64^{th}$ of a second. SNG counts are integrated over 8 such energy sweeps, which comprise a single 32-second "A-cycle". Due to telemetry limitations and the lower detection efficiency for ions, TOF counts in each channel are integrated over longer intervals called "B-cycles" which may span 8, 16, or 32 A-cycles depending on telemetry mode. During Titan encounters including T40, however, B-cycles always span 256 seconds (8 A-cycles).

The time-integrated TOF spectra acquired during each B-cycle are further reduced before transmission to Earth. Within ~1 hour from CA to Titan, which applies to the IMS data analyzed here, 512 uniformly spaced channels are returned per B-cycle out of the 2048 TOF channels. Between ~1 and 2 hours out, only 256 channels are transmitted. Moreover, although the ESA steps through 63 voltage levels per A-cycle, both SNG and TOF counts are summed over even, odd, or adjacent levels such that only 32 energy bins are returned. For the subset of data analyzed here, *adjacent* energy levels were summed, *every other* ST channel starting with channel 41 was returned, and *every* LEF channel starting with channel 651 was returned. Note that we index channels from 1 to 2048 instead of from 0 to 2047 as is done in the raw TOF data files.

Although SNG counts were not used for peak fitting in this work, I did use them to determine the energy distribution of the collected ions as well as the direction of peak ion flow during each of the A-cycles analyzed. As such, it was necessary to correct the SNG counts for anode cross talk before their angular distribution could be extracted. This correction, determined from in-flight calibration using solar wind protons, accounts for those ions that enter the collimator in one sector but produce a "start" signal in a different sector. Mathematically the correction amounts to a matrix multiplication for each A-cycle that redistributes a portion of the counts in each sector to each of the other sectors. The matrix used here was obtained from the CAPS PDS Users's Guide by R. J. Wilson, F. Crary, L. K. Gilbert, D. Reisenfeld, J. T. Steinberg, and R. Livi, available at the Planetary Data System website: pds.nasa.gov.

3.7 T40 IMS Measurements

The seven TOF data collection cycles (a.k.a. "B-cycles") examined in this work

are designated "A" through "G" in Figure 3.3.1, with A representing the cycle occurring

farthest from Titan and G the one closest. Each cycle corresponds to the minimum

integration time required by IMS to produce a single mass-and-energy-discriminated

spectrum. The numbered intervals in Figure 3.3.1 above and 3.7.1 below indicate regions

where the IMS total ion count (a.k.a. the "singles" or "SNG" count) peaked, while the

intervals labeled "INMS" near CA and egress mark the regions where INMS sampled

Titan's ionospheric composition. Each panel in Figure 3.7.2 depicts the solid angle swept

out by the IMS FOV during the associated numbered interval, with the total energy-

integrated ion count in each sector indicated by the accompanying color scale. For

comparison, Figure 3.3.1 also shows the pointing of the relatively narrow INMS FOV at

low and high altitudes.

Figure 3.7.2 reveals the anisotropy of the measured ion velocity distributions.

Each peak is contained within ~96° of actuation, and the direction of the peak flow varies

with altitude over ingress. The smallest of the peaks appear to coincide with Titanward,

radial pointing at higher altitudes (intervals 1, 3, and 4), while the largest coincide with

pointing that is into corotation (5 and 6) or into corotation with a substantial northward

component (8) at lower altitudes, possibly indicating a magnetic connection to the

ionosphere along highly draped field lines. Appropriately, the three B-cycles with the

fewest counts (A, C, and D) encompass the smallest of the SNG peaks (1, 3, and 4), and

the two B-cycles with the highest counts (E and G) encompass the largest of the SNG

peaks (5, 6, and 7).
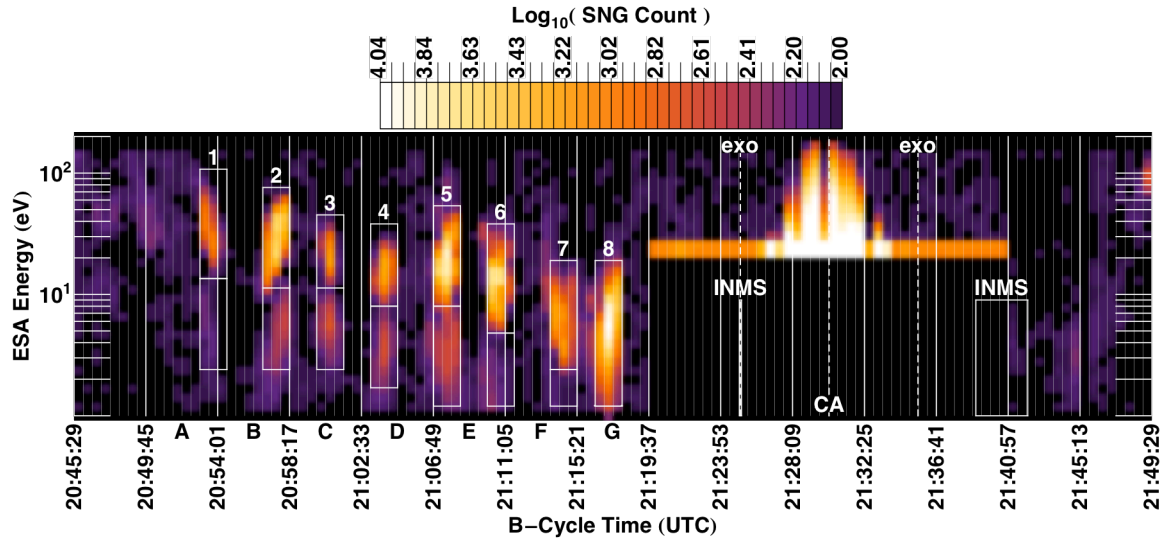
Figure 3.7.1 T40 IMS SNG spectrogram

Sector-summed SNG counts versus energy acquired on ingress during the T40 encounter.

Lettered and numbered intervals correspond to those labeled in Figure 3.3.1. White boxes

indicate the lower-energy light ion peaks (1, 2, and 3 amu) and the higher-energy heavy

ion peaks (12–19 and 24–32 amu) detected by IMS. Boxes labeled "INMS" indicate the

regions sampled by INMS. Exobase crossings and closest approach are indicated by

dashed lines. See pages I–XI for attributions.
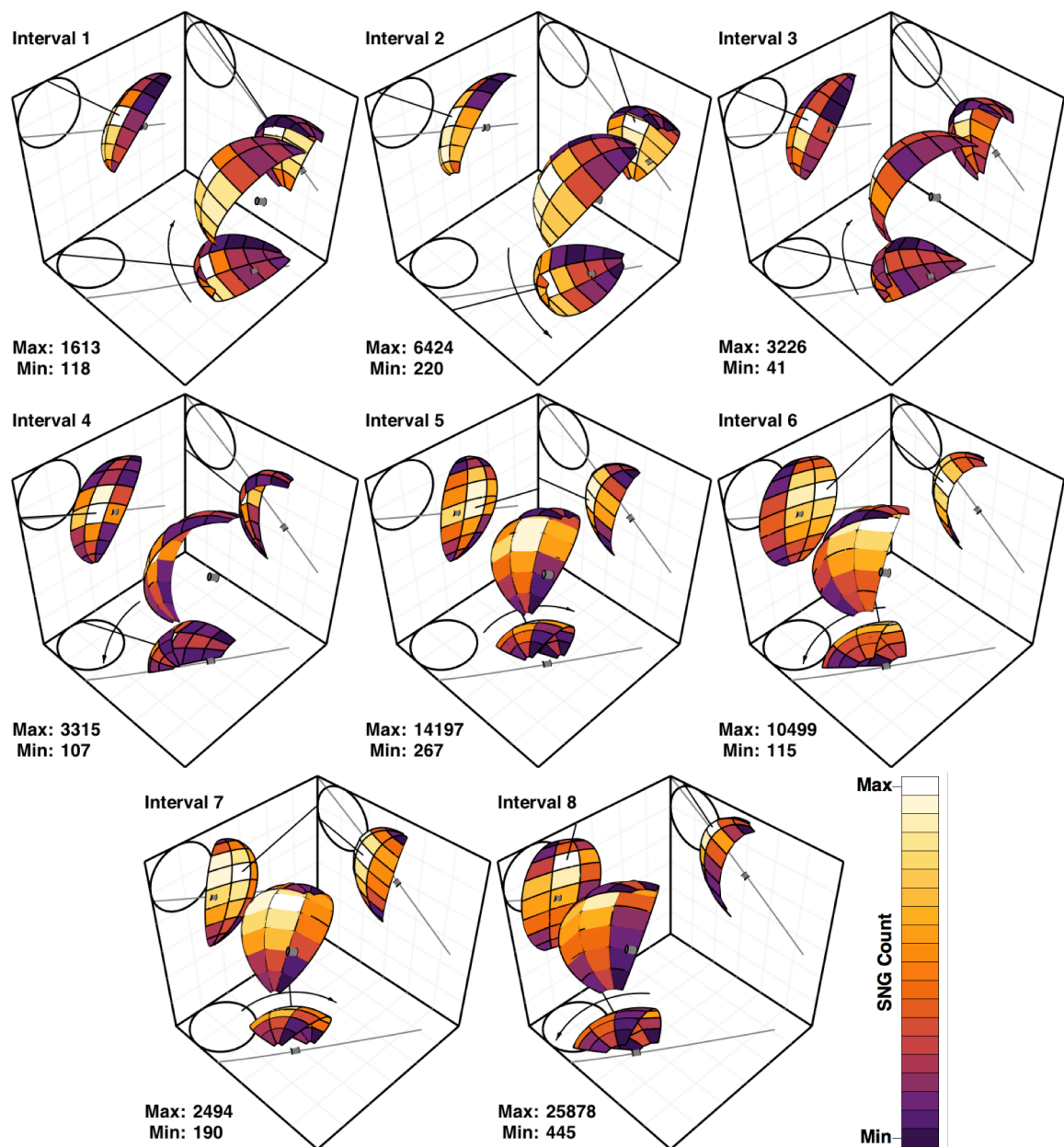
Figure 3.7.2 IMS FOV during T40 encounter

Panels correspond to the numbered intervals in Figure 3.3.1. Each FOV represents eight entrance sectors by 3 A-cycles of coverage. Axes and scales are the same as in Figure 3.3.1. Colors indicate energy-summed, cross-talk corrected SNG counts. Black circles indicate Titan's position in projection and black arrows in the XY plane indicate the sense of CAPS actuation. See pages I–XI for attributions.

Intervals 2 and 7 and their concurrent cycles, B and F, are exceptions to the above trend. During interval 2 IMS sweeps beyond Titan farther into the anti-Saturn direction than it does during intervals 1 or 3 and simultaneously sees a spike in counts. In contrast, counts plummet during interval 7 despite upstream pointing similar to neighboring intervals. In the case of interval 2 this may indicate a flow of pickup ions from Titan's anti-Saturn hemisphere toward it's Saturn-facing hemisphere as discussed in Ledvina et al. [2012], while interval 7 may simply reflect the discontinuous structure of the wake. As seen in Figures 3.7.3, however, the relative predominance of the heavy-ion peak beyond TOF channel 750 during B-cycles E and G implies that those ions are confined to the interior of Titan's Saturnward wake more so than the medium-mass ions represented between TOF channels 400 and 750. Adopting the notation of Ledvina et al. [2012] I hereafter refer to the light-ion group (H^+, H_2^+ and H_3^+) between ST TOF channels 1 and 400 as $\boldsymbol{L}^+$, the medium-mass group (masses 12–19 amu) between channels 400 and 750 as $\boldsymbol{M}^+$, and the heavy-ion group (masses 24–32 amu) above channel 750 as $\boldsymbol{H}^+$. Bold italics are used to distinguish the group $\boldsymbol{H}^+$ from the hydrogen ion, H^+.

A survey of individual TOF spectra reveals that all T40 $\boldsymbol{L}^+$, $\boldsymbol{M}^+$ and $\boldsymbol{H}^+$ counts are associated with energies below 200 eV, which can be seen in the sector-summed SNG spectrogram plotted in Figure 3.7.1 and the TOF spectrograms plotted in Figure 3.7.3. Since count accumulation over a B-cycle is typically low for a given energy level, the TOF spectra have been energy-summed for peak fitting. Moreover, since the calibration peak shapes used for fitting are insensitive to changes in energy below 200 eV, as will be discussed in Section 3.8, any smearing due to this sum is negligible. Thus the integrated

TOF spectra in Figure 3.7.3 effectively represent the summation of TOF counts up to 200 eV for each of the targeted B-cycles.

It is important to note that the dearth of counts in the LEF spectra near channel 1100 is evidence that water group ions are largely absent in this part of the wake. This observation is consistent with the explanation given by Hartle et al. [2006a] that O^+ flowing past Titan at distances smaller than the ion's ambient gyrodiameter (~11,200 km) are collisionally removed by the atmosphere. This is critical for the peak fitting performed here because the broad water-group peak, often present in spectra acquired outside of the interaction region, would overlap with the M^+ peak between ST channels 400 and 750 making unambiguous identification intractable.

In Figure 3.7.4 I have plotted the anode-summed SNG energy profiles for intervals 1 through 8 as they relate to spacecraft altitude. Each profile represents a slice through the spectrogram at a single 32-second A-cycle, which corresponds to the minimum integration time required for IMS to produce a single energy-discriminated SNG spectrum. However, while the spectrogram has been binned the profiles have not, so that each ESA energy bin is represented individually.
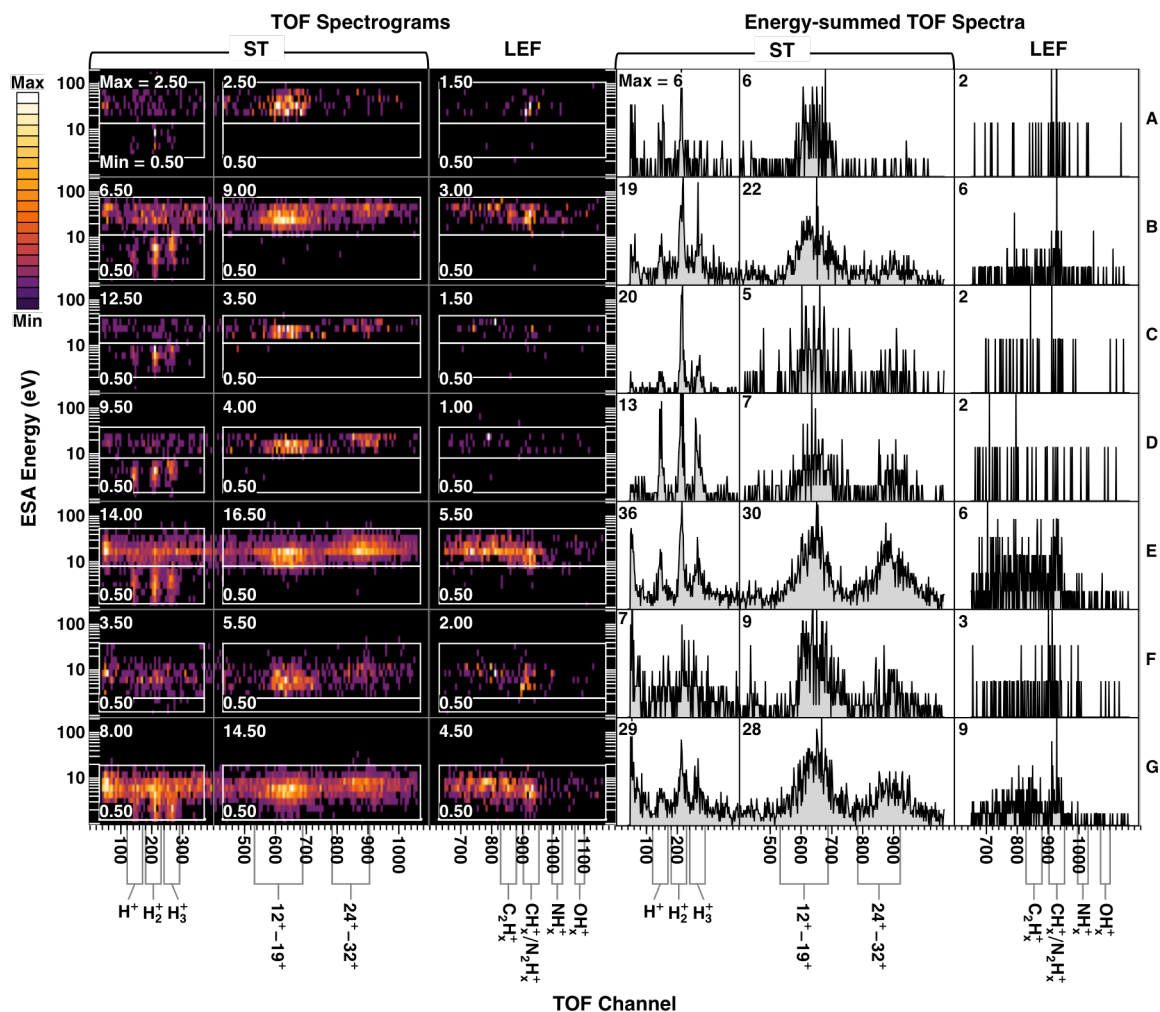
Figure 3.7.3 T40 IMS TOF spectra

TOF spectrograms (left) and energy-summed TOF spectra (right) for T40 B-cycles A through G. Each spectrogram is scaled to the entire range of colors with min and max counts indicated in the lower and upper left corners, respectively. White boxes indicate energy ranges spanned by the light and heavy ion groups as in Figure 3.7.1. Fractional counts result from mapping the collapsed TOF counts back to the full range of channels and energy bins and are summed to integer values on the right. See pages I–XI for attributions.
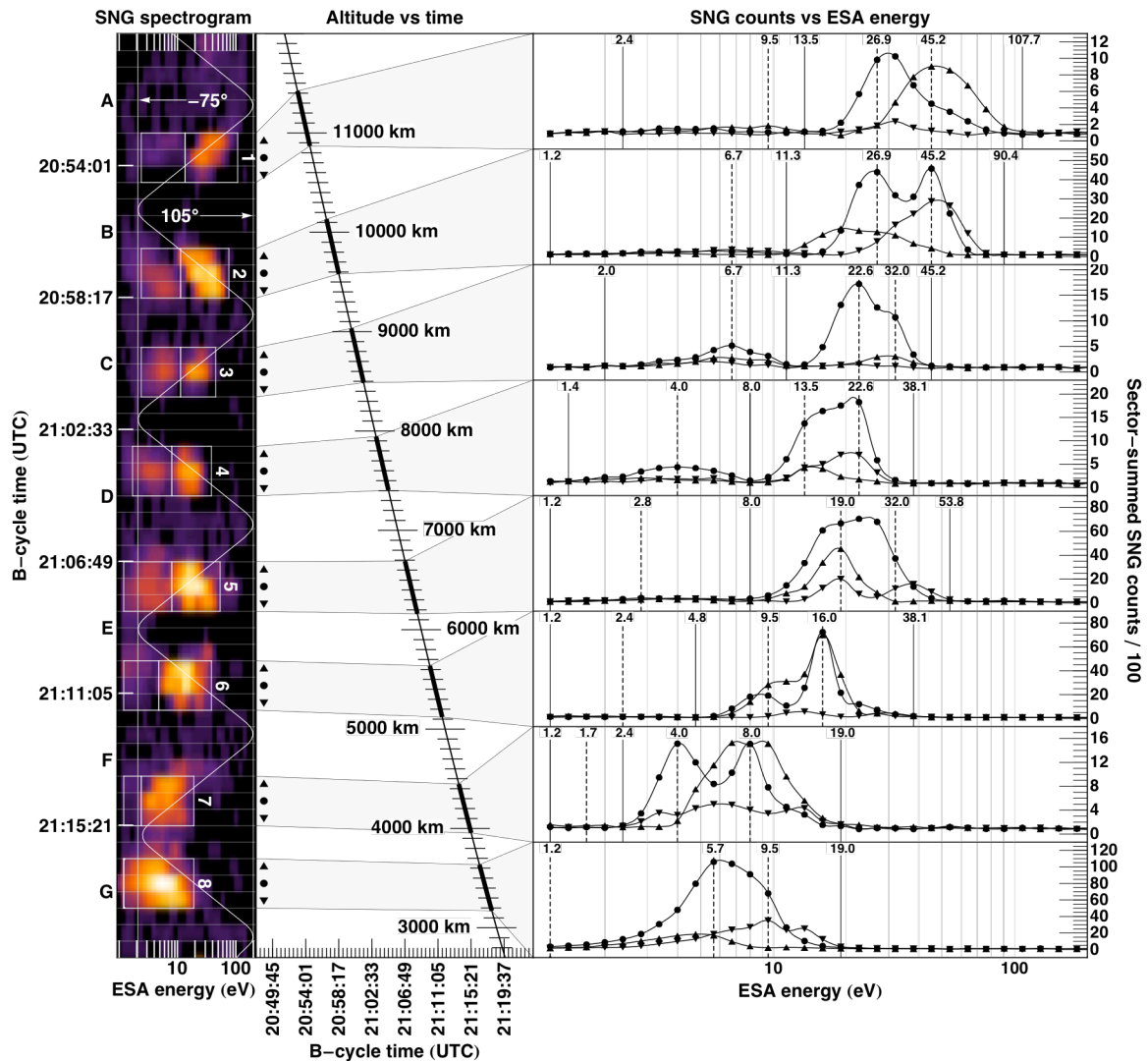
Figure 3.7.4 T40 ion energy profiles

Sector-summed SNG counts vs. energy for each of the numbered intervals in Figure 3.3.1. The spectrogram at left is a cropped and rotated copy Figure 3.7.1 with the CAPS actuation angle superimposed. The middle panel indicates time and altitude and connects each interval with the corresponding set of energy profiles on the right as denoted by the plot markers. Data points are joined by second-order polynomial splines. Boxed energy ranges on the left are spanned by solid vertical lines on the right. See pages I–XI for attributions.

Comparing the SNG spectrogram in Figure 3.7.1 to the TOF spectrograms and integrated TOF spectra in Figure 3.7.3, it is clear that the lower-energy, light red SNG peaks consist entirely of L^+ ions while the dominant peaks consist primarily of M^+ and H^+. In each energy profile the L^+ population is evident as the set of small peaks to the left while the M^+ and H^+ populations comprise the set of large peaks to the right. In almost all cases the leading profile (indicated by upward triangles) in the upper energy range develops a shoulder or splits into two peaks (circles) as the actuator sweeps through the flow. This is suggestive of overlapping populations with flow velocities that are separated by less than ~32° or a single population with a bimodal velocity distribution. Although not obvious, the overlapping-population interpretation is supported by the TOF spectrograms in Figure 3.7.3. Notice that in spectrograms B, C, D, E and G the tail of the M^+ energy distribution and that of the H^+ distribution stretch in opposing directions. This same behavior can be observed in the energy profiles in Figure 3.7.4, and will help in future efforts to deconvolve the energy profiles.

While we have not undertaken a full deconvolution of the energy profiles in this study, velocity estimates for the three fitted ion groups will be given in Section 3.9 for comparison with the INMS data and model results. In calculating these values I have assumed that the peak SNG count measured during each numbered interval corresponds to the bulk component of the sampled velocity distribution and that the ion temperature is comparatively small. This is difficult to confirm near Titan where Cassini's plasma environment can change faster than IMS can perform a full angular survey. However, for compact peaks that are well centered within the FOV, like most of those plotted in Figure

3.7.2, it is reasonable to assume that the full distribution has been sampled and that the plasma is well collimated along the peak direction.

Several SNG peaks (1, 2, 7, and 8) are clearly observed to shift up or down in energy concurrent with the actuation of the instrument, which is most easily observed in the SNG spectrogram in Figure 3.7.4. While apparently related to the actuation, the reason for this shift remains unclear. In addition, measured ion energies are influenced by spacecraft charging which is difficult to quantify in general but has been reported by Coates et al. [2012] to vary between 0 and -2 V near Titan. The spacecraft potential will be revisited in Section 3.9 as it relates to lower and upper limits on the ion group velocities and densities presented there.

3.8 Background and peak fitting techniques

As stated above, after mapping the collapsed raw data back to the full range of 2048 TOF channels and 63 energy levels, I ascertained that all counts collected within 10 R_T of Titan's surface during the T40 encounter fell below 200 eV. The spectra for each B-cycle were then summed over energy and the results smoothed using a Savitzky-Golay filter [Savitzky and Golay, 1964], which replaces the value at the center of its sliding window with the value at the center of a polynomial that best fits the windowed data. It was determined by visual inspection that a window length of 9 and a polynomial order of 2 sufficiently reduces noise while best preserving the shapes of the narrow TOF peaks below channel 400, and a window length of 17 and a polynomial order of 1 works best

for the broad peaks above channel 400. Figure 3.8.1 shows an example of the Savitzky-Golay filter applied to the ST TOF counts for a single energy-summed B-cycle.
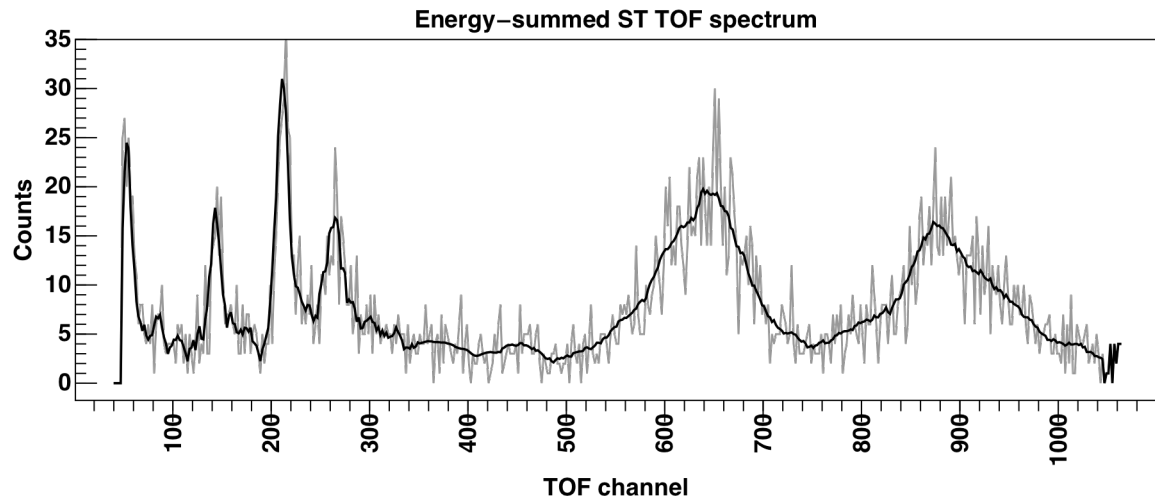
Figure 3.8.1 Savitsky-Golay smoothing filter

An example of the Savitsky-Golay smoother applied to an energy-integrated ST TOF spectrum for a single B-cycle. See pages I–XI for attributions.

Rather than fit a constant background to the data, as was done in prior analyses, I derived the background model used here from the TOF data itself. Since IMS was designed for low-density measurements, both the ST and LEF detectors saturate due to high count rates at low Titan altitudes. These saturated spectra approximate the spectrum of all possible ion and electron scattering events within the instrument, and are relatively smooth and devoid of peaks, exhibiting power-law behavior at low TOF channels that transitions to linear behavior at higher channels as seen in the bottom panel of Figure 3.8.2. To fit this behavior I first integrated all saturated ST and LEF spectra acquired below ~2200 km between 2004 and 2012 and reduced the 16-channel repeating pattern

61

noise that is ubiquitous throughout the TOF data. This pattern is thought to arise from slight impedance mismatches along the length of the delay-line used in the ion-timing circuit. The mismatch leads to a consistent set of "tick-length" differences between the 16 taps along the line, where each tick corresponds to the duration of a single TOF channel (~0.781 ns). Thus, ions detected near the interfaces between consecutive ticks may be improperly binned in a manner that repeats every 16 channels within a given spectrum.

To determine the pattern correction I first fit a line to the integrated LEF background spectrum, normalized the spectrum to the fitted line, and averaged consecutive 16-channel intervals to obtain the single array of 16 coefficients shown in the top panel of Figure 3.8.2. Minding the ST data reduction explained above, the coefficient array was then divided into each 16-channel interval of the integrated ST spectrum to reduce the contribution due to the pattern noise. Finally, the part of the integrated ST spectrum below channel 200 was fit with a power-law while that above channel 600 was fit to a line. In the region between the two points where the functions intersect, the background was taken to be the average of the two functions. This piecewise construction is illustrated in the bottom panel of figure 3.8.2.

This correction is only effective when the pattern is well resolved, which requires far more accumulation than occurs during a typical B-cycle. Therefore, no attempt was made to remove the pattern from each individual spectrum. However, since the pattern manifests as pairs of neighboring pits and spikes about some intermediate value, the smoothing performed by the Savitzky-Golay algorithm amounts to an averaging similar

to the straight-line fit shown in the top panel of Figure 3.8.2. Moreover, the 9 and 17

point sliding windows used to smooth the data are sufficient to span 1 and 2 pattern

lengths, respectively, in the collapsed ST data.
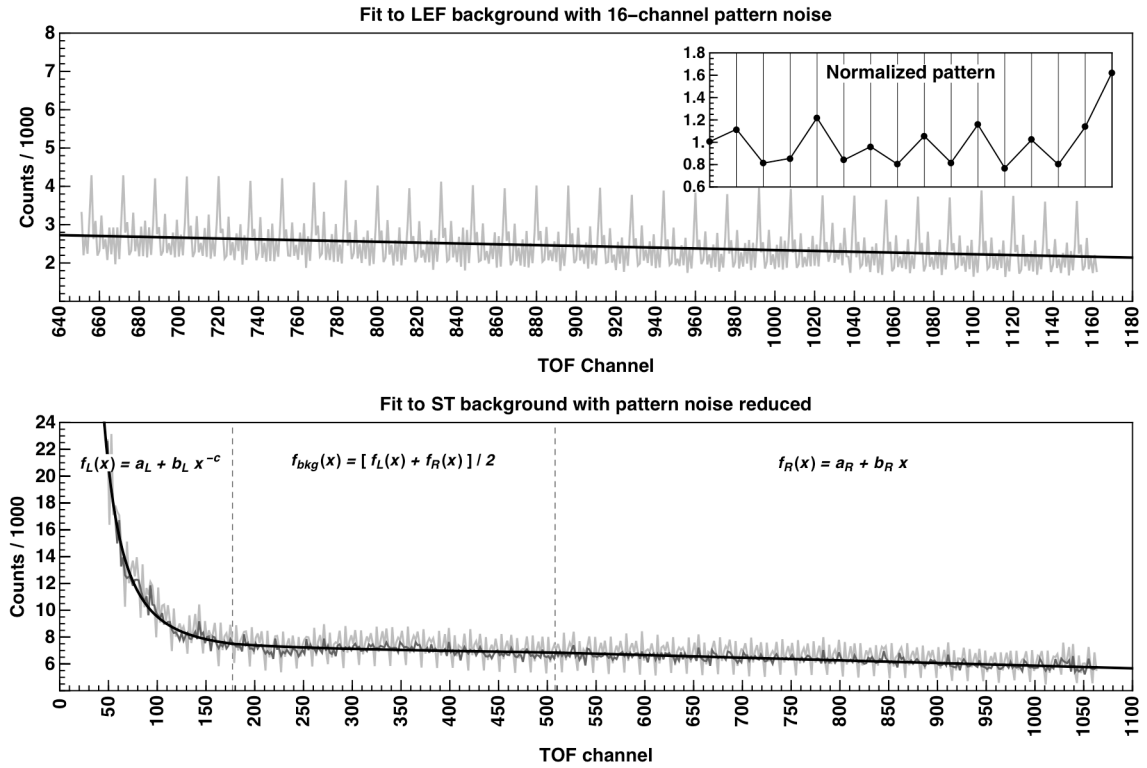
Figure 3.8.2 IMS TOF background model determination

The top panel characterizes the 16-channel pattern noise based on a linear fit to the sum

of all LEF TOF spectra acquired below ~2200 km at Titan. The bottom panel shows the

background function obtained from a piecewise fit to the smoothed, analogously-summed

ST TOF spectrum. See pages I–XI for attributions.

    The peak model used for fitting is that derived from IMS calibration

measurements carried out with the flight instrument at Los Alamos National Laboratory,

and more extensive measurements conducted with the IMS prototype at NASA's

Goddard Space Flight Center. In each case spectra were acquired experimentally using a

variety of incident ions, ion energies, and angles of incidence and the position and shape

of each ion fragment's peak was fit to a four-parameter Logistic Power Peak (LPP)

model,

$$LPP(x; a, b, c, d) = a\,(d+1)^{\frac{d+1}{d}}\,e^{(x-b)/c}\,[1 + d\,e^{(x-b)/c}]^{-\frac{d+1}{d}}, \quad (3.8.1)$$

where *a* is the peak height, *b* the peak position, *c* controls the peak width and its sign

determines the orientation of the peak's tail, and *d* controls the peak asymmetry. Care

must be taken in using the calibrations to interpret the data since differences between

laboratory and in situ conditions are unavoidable. Calibration peak widths, for example,

tend to underestimate in situ peak widths by ~20% (D. Reisenfeld et al., unpublished

data, 2007), and calibration peak positions have been found to differ significantly

between the IMS prototype and flight model (D. Reisenfeld et al., unpublished data,

2005). Given this uncertainty in the calibration parameters, as well as the peak overlap

discussed in the instrument description, it is difficult to extract individual ion peaks even

with a priori information about the composition.

In order to account for possible systematic differences between the calibration and

data peaks, I have augmented the LPP equation with group parameters so that sets of

peaks can be scaled, shifted, or widened in unison. The modified LPP equation used in

my fitting algorithm thus becomes

$$LPP\left(x; \boldsymbol{g}_i, \boldsymbol{p}_{ij}\right) = \tag{3.8.2}$$

$$\alpha_i\, a_{ij}\, (\delta_i\, d_{ij} + 1)^{\frac{\delta_i\, d_{ij}+1}{\delta_i\, d_{ij}}}\; e^{\frac{x-(\beta_i+b_{ij})}{\gamma_i\, c_{ij}}}\; \left[1 + \delta_i\, d_{ij}\, e^{\frac{x-(\beta_i+b_{ij})}{\gamma_i\, c_{ij}}}\right]^{-\frac{\delta_i\, d_{ij}+1}{\delta_i\, d_{ij}}},$$

where, essentially, each LPP peak parameter is multiplied by a group-specific scale factor. The set of group parameters $\boldsymbol{g}_i = \{\alpha_i, \beta_i, \gamma_i, \delta_i\}$ corresponds to $\boldsymbol{g}_i \in \{\mathrm{H}^+, \mathrm{H}_2^+, \mathrm{H}_3^+, \boldsymbol{M}^+, \boldsymbol{H}^+\}$ and the set of peak parameters $\boldsymbol{p}_{ij} = \{a_{ij}, b_{ij}, c_{ij}, d_{ij}\}$ corresponds to the jth peak within the group $\boldsymbol{g}_i$.

For peak fitting I employ a variant of the Differential Evolution (DE) algorithm of Storn and Price [1997] to minimize the sum of squared residuals between the IMS TOF data and the sum of the background and peak functions. DE is a stochastic global function minimizer that uses an evolutionary strategy to iteratively modify a population of candidate minima so that members of subsequent generations converge to the global minimum. Moreover, as a minimization progresses, candidates that are nearer to the *global* minimum help to extricate others from *local* minima by sharing their superior "genes". This method was chosen over more traditional derivative-based searches in order to avoid the pitfalls associated with those searches; namely, divergence and local-minimum trapping. Unlike many derivative-based minimization routines, such as the Levenberg-Marquardt algorithm that others have used to fit the TOF data, DE easily accommodates parameter constraints that prevent the divergence of candidate minima from one generation to the next and allow for fine-tuning of the minimization process.
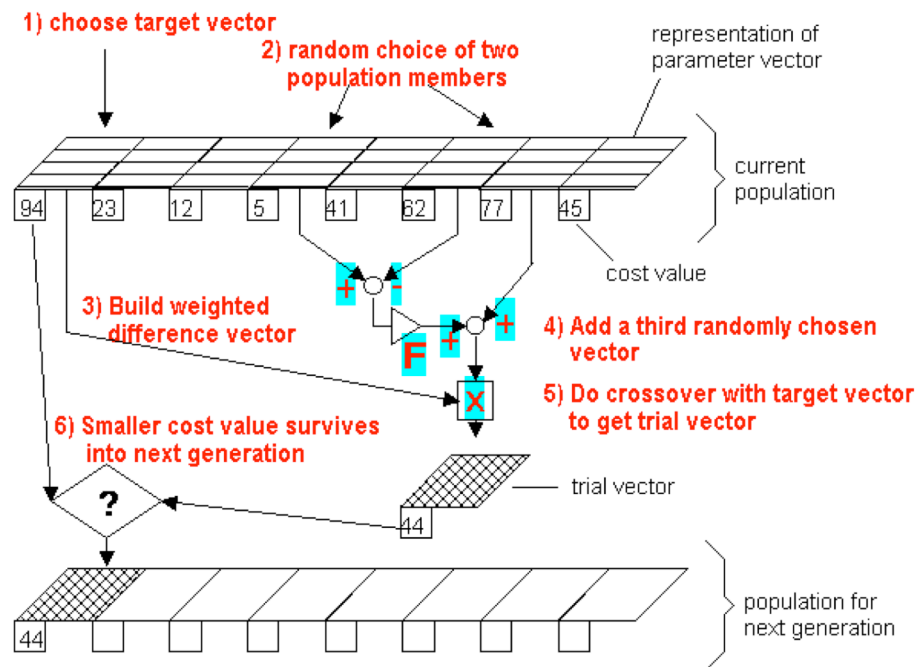
Figure 3.8.3 Differential Evolution algorithm

The flow chart shows a single iteration of the algorithm. At each generation, a new

population of parameter vectors is generated by crossing each "target" member of the

current population with a "mate" constructed from a linear combination of randomly

chosen vectors from the same population. The resultant "trial" vector is then compared to

the target and the one with the lowest cost enters the new population as the "offspring" of

the target and mate vectors. See pages I–XI for attributions.

Figure 3.8.3 illustrates a single iteration of the algorithm, which is repeated until

specified stopping criteria are met. Optimal linear combinations and crossover schemes,

corresponding to steps 3–4 and 5 in the figure, respectively, vary depending on the

complexity of the data and that of the model used to fit the data. After trying a variety of

different schemes I found that for all spectra fitted, and almost all randomly generated

initial parameter-vector populations, the algorithm converged to a minimum in under

1000 generations using a population size of 250, binomial crossover with probability

$C = 0.9$, and mate vectors constructed from the linear combination

$$\boldsymbol{p}_{mate} = \boldsymbol{p}_{best} + F\left(\boldsymbol{p}_{rand\,2} - \boldsymbol{p}_{rand\,1}\right). \qquad (3.8.3)$$

For each mate vector generated, $F \in (0, 1]$ is a uniformly distributed random scale factor,

$\boldsymbol{p}_{rand\,1}$ and $\boldsymbol{p}_{rand\,2}$ are randomly selected vectors from the current generation, and $\boldsymbol{p}_{best}$

represents the current lowest-cost parameter vector. With binomial crossover, a uniform

random number r_j is generated for each component, $(\boldsymbol{p}_{off})_j$, of the offspring vector. If

$r_j > C$ then the jth component of the offspring vector is set to the jth component of the

target vector, or $(\boldsymbol{p}_{off})_j = (\boldsymbol{p}_{targ})_j$. Otherwise it is set to the jth component of the mate

vector: $(\boldsymbol{p}_{off})_j = (\boldsymbol{p}_{mate})_j$. Binomial crossover is so named because the number of

parameters borrowed from the mate vector follows a binomial distribution.

Although the DE algorithm has proven adept at finding global minima for a

variety of different functions [Vesterstrom and Thomsen, 2004], there is yet no analytical

proof of its convergence. In addition, a fit that minimizes the cost function may not be the

fit that best represents the true ion composition if parameters are allowed to vary too

generously. The parameter constraints applied here to the TOF fits are based on the valid

ranges for each of the LPP parameters and the uncertainty in their calibrated values. For

each fitted spectrum, the LPP amplitude parameter, a, is constrained to lie between zero

and the maximum unsmoothed count. Both the width parameter, c, and the asymmetry

parameter, d, are checked after initialization and after each crossover operation to ensure non-negative, non-zero values, and the tail-direction parameter, s, is normalized to -1 or $+1$ depending on its sign. All relevant TOF calibration peak positions, expressed by the b parameter, vary less then 8 channels as a function of energy between 0 and 200 eV, and peak widths vary by less than 2% over the same range. I therefore restricted all peak positions to lie within ± 10 channels of their calibration values at 100 eV. Keeping in mind the roughly 20% uncertainty in calibration widths mentioned above, I similarly restricted each peak width parameter, c, to lie between 0.5 and 1.5 times its calibration value at 100 eV. Figure 3.8.4 plots the calibration peak positions and peak widths as a function of ESA energy for the ion species fitted in this study.

Each fit was restricted to the subset of channels containing the neutral-fragment peaks for the observed ion groups: channels 115–305 for the L^+ group, 747–753 for M^+, and 753–1039 for H^+. This was done to prevent the low-amplitude, negative-fragment peaks from the M^+ group, found between channels 300 and 500, from influencing the background and neutral-fragment fits. Due to this restriction, however, attempts to fit both the background and peak functions simultaneously via the DE algorithm resulted in background levels that, while minimizing the cost function, were clearly too large to represent the true background. Instead, for each B-cycle I took the subset of unsmoothed data points with the n lowest amplitudes and used a simple gradient descent algorithm to minimize the sum of squared residuals between the points and the background function to six decimal places. Starting from $n = 1$ I incremented n and selected the best fit by visual inspection. The selected background levels were then treated as fixed parameters

in subsequent peak fits. The raw data points yielding the best background fit for each B-cycle are shown in Figure 3.8.5.

Since the *L+* peaks are relatively well separated from one another and from the *M+* and *H+* peaks, I fitted each of the *L+* peaks individually. However, although the *M+* and *H+* groups do not overlap substantially, their constituent peaks do. While I hope to explore the individual peak fits in a future study, I have here restricted my analysis to "group" fits, allowing the fitting algorithm to vary each group's constituent-peak parameters in tandem (within the ranges described above) to achieve the best overall fit to each of the broad *M+* and *H+* peaks.
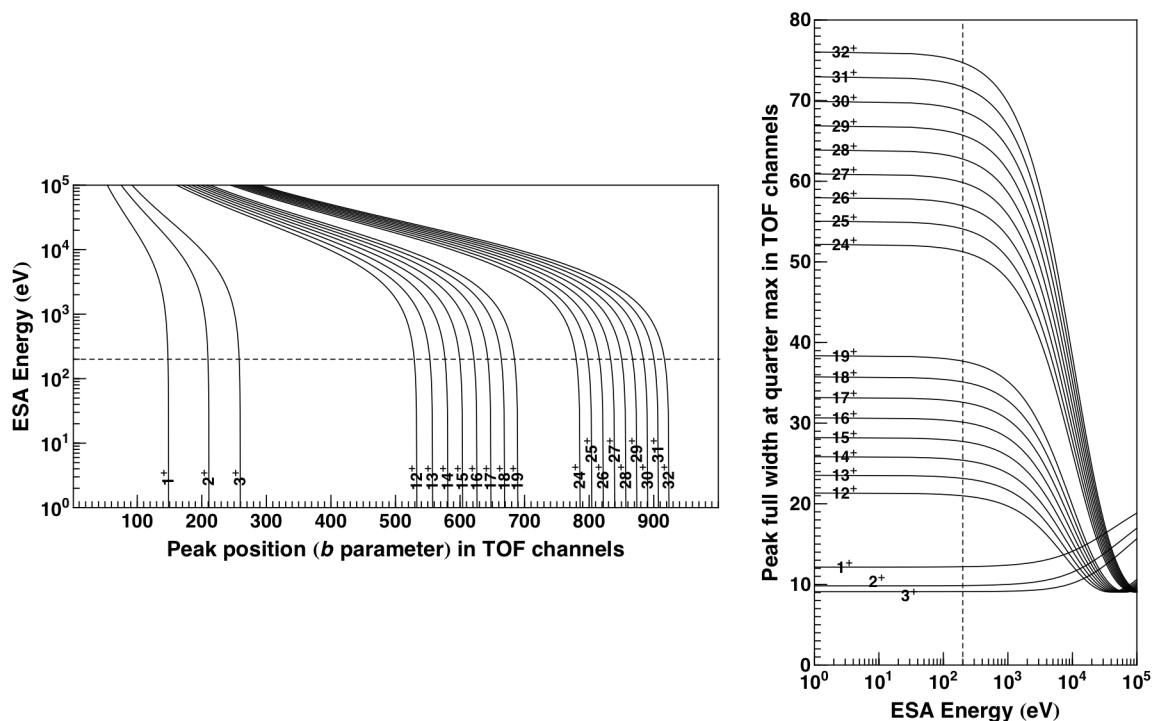
Figure 3.8.4. LPP parameters versus ESA energy

The change in peak position (left) and in peak FWQM (right) versus energy for all fitted ion peaks. Curve labels indicate the associated ion charge and mass, and a dashed line in each plot indicates the upper limit on the measured ion energies (200 eV) as discussed in the text. Note that below this upper limit the peak characteristics (position and width) represented by the curves in each plot remain relatively constant. See pages I–XI for attributions.

After fitting the background, the *L*+ fit was performed 100 times with different seed values for the DE algorithm's random number generator while holding the *L*+ peak widths and asymmetries at their calibration values. The resulting peak positions were then averaged and input as fixed parameters in subsequent fits. This was done to prevent the algorithm from homing in on nearby background fluctuations of similar size in

70

spectra having low **L+** counts. I then performed an omit-one Jackknife statistical analysis on each group to obtain best-fit values and standard errors for the rest of the fitted parameters, using the same seed value for each fit. For the **L+** jackknife analysis only the peak amplitudes were varied while the peak positions were set to their previous best-fit values and the widths and asymmetries held at their calibration values. Similarly, **M+** and **H+** peak amplitudes were varied individually while positions and widths were varied in tandem within each group and only the asymmetries were restricted to their calibration values. Since the tail of the broad **M+** peak influences the leading edge of the broad **H+** peak, **H+** group fits were carried out with the **M+** peak parameters set to their best-fit values. A given fit was considered to have converged when the sum of squared residuals and each parameter of the best candidate for minimum varied by less than 10^{-6} over ten consecutive generations. Fit results for each B-cycle are plotted in Figure 3.8.5.
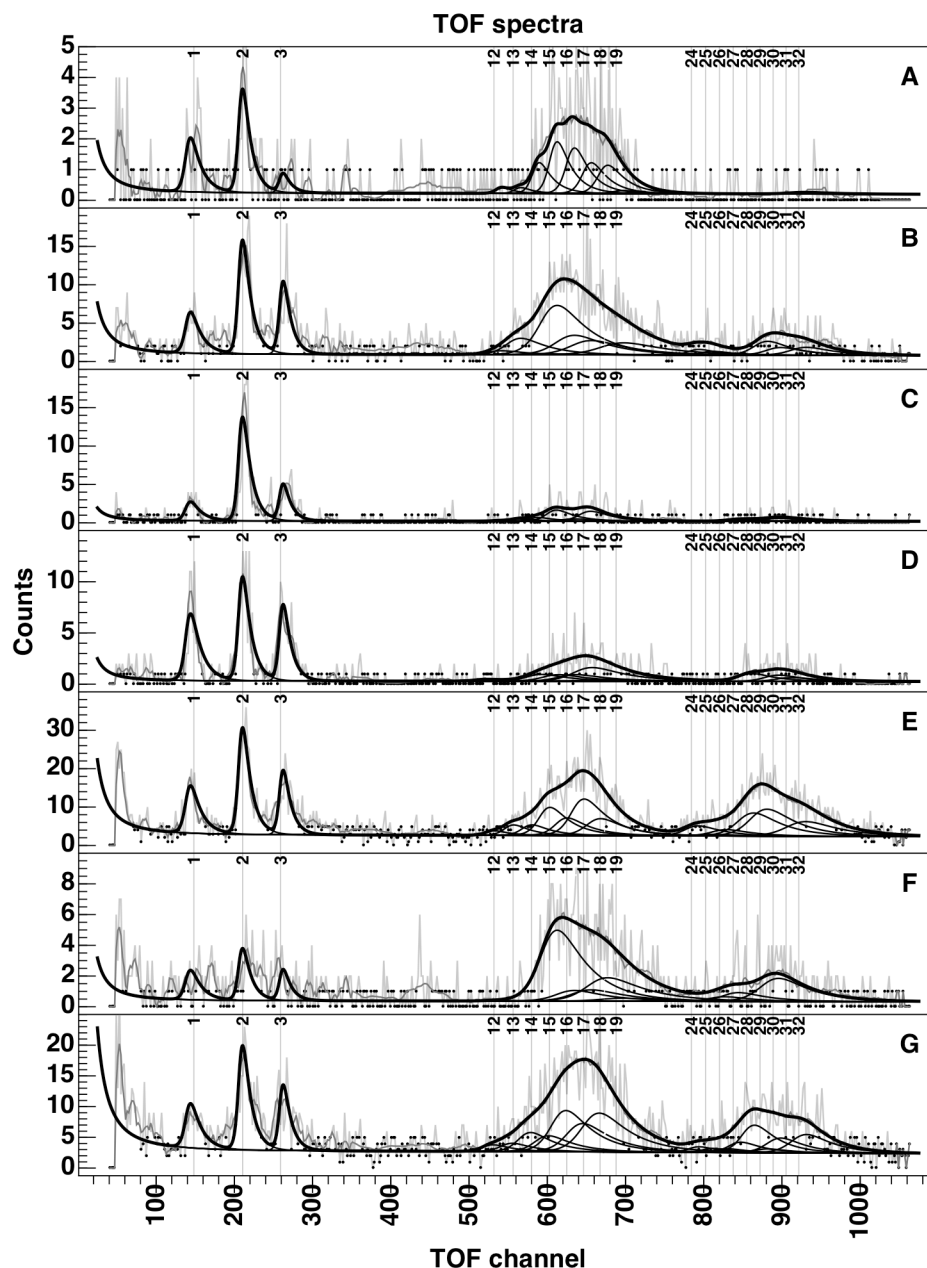
Figure 3.8.5 T40 fit results

For each fitted B-cycle, thin and thick black lines represent individual model fits and their sums, respectively. Discrete peaks are shown for illustrative purposes since only group sums were utilized in this study. Raw and smoothed data are rendered in light and dark gray, respectively, while black points indicate the raw data used to fit the background as explained in the text. For reference, vertical lines indicate calibration peak positions at 100 eV. See pages I–XI for attributions.

3.9. Estimating ion group velocity and density

TOF counts for a particular ion group, g, are converted to fluences via the

formula

$$N(g) = \sum_k \frac{C(g, E_k)}{\Gamma(E_k)\, \varepsilon(g, E_k)},$$ (3.9.1)

where $N(g)$ is the total number of g ions entering the IMS collimator during a given

B-cycle, $C(g, E)$ is the number of g ions *detected* at energy level E, $\varepsilon(g, E)$ is the

detection efficiency for g ions with energy E, and

$$\Gamma(E) = \frac{G(1, E)}{a_0\, \Omega_0\, r_E},$$ (3.9.2)

can be considered the geometric *efficiency* of the IMS collimator and energy

analyzer. Here, $a_0 \approx 6.5$ cm^2 is the entrance area of a single sector of the collimator

(D. Reisenfeld et al., unpublished data, 2007) and $\Omega_0 \approx 0.05$ sr is the solid angle

subtended by a single sector. The IMS geometric factor over n sectors has been

simulated numerically (D. Reisenfeld et al., unpublished data, 2007) and is given by

$$G(n, E) = \frac{n}{8}\left[0.00427 + 0.00169\left(\frac{E}{1000}\right)^{-0.1379}\right] \text{cm}^2 \text{ sr eV/eV},$$

where E is the ESA energy level in eV/q.

In order to place upper and lower bounds on the relative fluences, R, we have calculated them using the lowest and highest geometric efficiencies and detection efficiencies over the range of energies considered. In other words

$$R_\mp(\boldsymbol{g}_i) = \frac{N_\mp(\boldsymbol{g}_i)}{\sum_j N_\mp(\boldsymbol{g}_j)},\tag{3.9.4}$$

where

$$N_\mp(\boldsymbol{g}_i) = \frac{C(\boldsymbol{g}_i)}{\Gamma_\pm\,\varepsilon_\pm(\boldsymbol{g}_i)},\tag{3.9.5}$$

$$C(\boldsymbol{g}_i) = \sum_j \frac{A(\overline{\boldsymbol{p}}_{ij})}{A_{bkg} + \sum_k A(\overline{\boldsymbol{p}}_{ik})}\,C_{tot},\tag{3.9.6}$$

and

$$A(\overline{\boldsymbol{p}}_{ij}) = \int_1^{2048} LPP\big(x;\overline{\boldsymbol{g}}_i,\overline{\boldsymbol{p}}_{ij}\big)\,dx\,.\tag{3.9.7}$$

In the equations above, $\Gamma_- = \Gamma(200\text{ eV})$ is the minimum and $\Gamma_+ = \Gamma(1\text{ eV})$ the maximum geometric efficiency over the range 1–200 eV, $\varepsilon_\mp(\boldsymbol{g}_i)$ is the minimum/maximum detection efficiency out of all member of the group $\boldsymbol{g}_i$ over the same energy range, $\overline{\boldsymbol{g}}_i$ and $\overline{\boldsymbol{p}}_{ij}$ are the jackknife-averaged parameters for group $\boldsymbol{g}_i$ and peak $\boldsymbol{p}_{ij}$, $A(\overline{\boldsymbol{p}}_{ij})$ represents the area under the LPP function evaluated at the set of group parameters $\overline{\boldsymbol{g}}_i$ and peak parameters $\overline{\boldsymbol{p}}_{ij}$, A_{bkg} is the area under the background function, and C_{tot} is the total number of TOF counts summed over a particular spectrum. Note that in Eq. 3.9.5 above, using lower and upper bounds for the

terms in the denominator has removed their energy dependence with respect to the sum while in the numerator the sum over energies is subsumed in the calculation of C_{Tot}, and the energy dependence of the peak areas is negligible over the range 1–200 eV as explained previously.
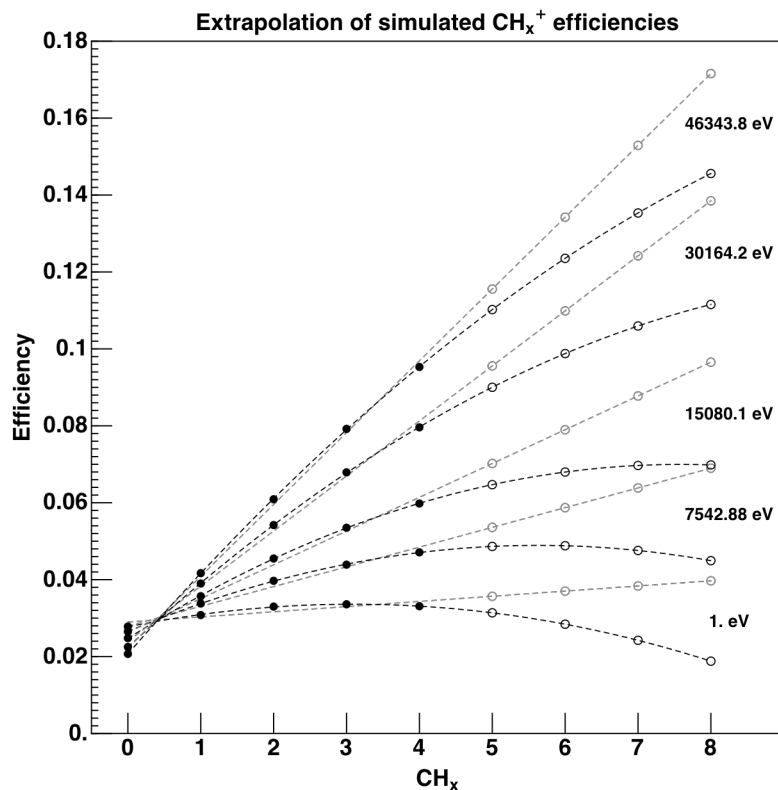
Figure 3.9.2 Extrapolation of simulated CH$_x$$^+$ detection efficiencies

A plot showing the detection efficiencies for CH$_5$$^+$, CH$_6$$^+$, CH$_7$$^+$, and CH$_8$$^+$ (open circles) extrapolated from the simulated values for CH$_0$$^+$, CH$_1$$^+$, CH$_2$$^+$, CH$_3$$^+$, and CH$_4$$^+$ (filled circles) at 4 of the 32 simulated energies. Dashed black lines represent quadratic extrapolations and dashed gray lines indicate linear extrapolations. See pages I–XI for attributions.

A limited set of simulated neutral-fragment detection efficiencies, $\varepsilon(S, E)$, for S = H$^+$, H$_2{}^+$, C$^+$–CH$_4{}^+$, N$^+$–NH$_3{}^+$, O$^+$, N$_2{}^+$, and O$_2{}^+$ at 32 different logarithmic energy levels (D. Reisenfeld, personal correspondence, 2014) were extrapolated in order to obtain efficiency ranges for ion masses 12–19 and 24–32 amu. At each energy level I fit the numerical efficiencies for C$^+$–CH$_4{}^+$ and N$^+$–NH$_3{}^+$ to both an upward-trending line and a downward-trending quadratic in order to extrapolate upper and lower bounds on the efficiencies for CH$_5{}^+$–CH$_8{}^+$ and NH$_4{}^+$–NH$_5{}^+$. An example of this extrapolation for CH$_5{}^+$–CH$_8{}^+$ is shown in Figure 3.9.2. The linear and quadratic fit coefficients for each ion were then interpolated in energy by natural cubic splines to yield analytic expressions for each species as a function of energy. The minimum efficiency out of all 12–19 amu ions over the energy range 1–200 eV was then selected as the lower bound for the $\boldsymbol{M^+}$ group and the maximum value was selected as the upper bound. For the 24–32 amu group I linearly extrapolated the differences in efficiency between O$^+$ and O$_2{}^+$, and between N$^+$ and N$_2{}^+$, to obtain the difference between C$^+$ and C$_2{}^+$ at each energy level and interpolated the resulting values as before. Efficiencies for C$_2{}^+$–C$_2$H$_8{}^+$ and N$_2{}^+$–N$_2$H$_4{}^+$ were then constructed by adding the corresponding differences to the C$^+$–CH$_8{}^+$ and N$^+$–NH$_4{}^+$ efficiencies. In other words,

$$\varepsilon(C_2H_x^+, E) = \varepsilon(CH_x^+, E) + \Delta\varepsilon_{C^+ \rightarrow C_2^+}(E)$$

and   (3.9.8)

$$\varepsilon(N_2H_x^+, E) = \varepsilon(NH_x^+, E) + \Delta\varepsilon_{N^+ \rightarrow N_2^+}(E)$$

where the Δ terms on the right-hand side represent the differences in efficiency, as functions of energy, between C^+ and C_2^+ and between N^+ and N_2^+, respectively. The minimum and maximum values out of all 24–32 amu ions over the energy range 1–200 eV were again chosen to represent lower and upper efficiency bounds for the $\boldsymbol{H^+}$ group. Efficiencies for H_3^+ were similarly extrapolated from the H^+ and H_2^+ efficiencies using only linear fits, and upper and lower bounds were chosen for each of H^+, H_2^+ and H_3^+ independently over the same energy range. All interpolated efficiencies and bounding ranges are illustrated in Figure 3.9.3.

The simulated detection efficiencies, $\varepsilon(S, E_k)$, discussed above incorporate what litte data there is on electron emission from thin, amorphous carbon foils over the range of energies and ion species measured by IMS. Improving on this body of knowledge is the goal of the experimental design presented in Appendix A, and the way in which the electron emission statistics figure into the detection efficiencies is explained in detail there.
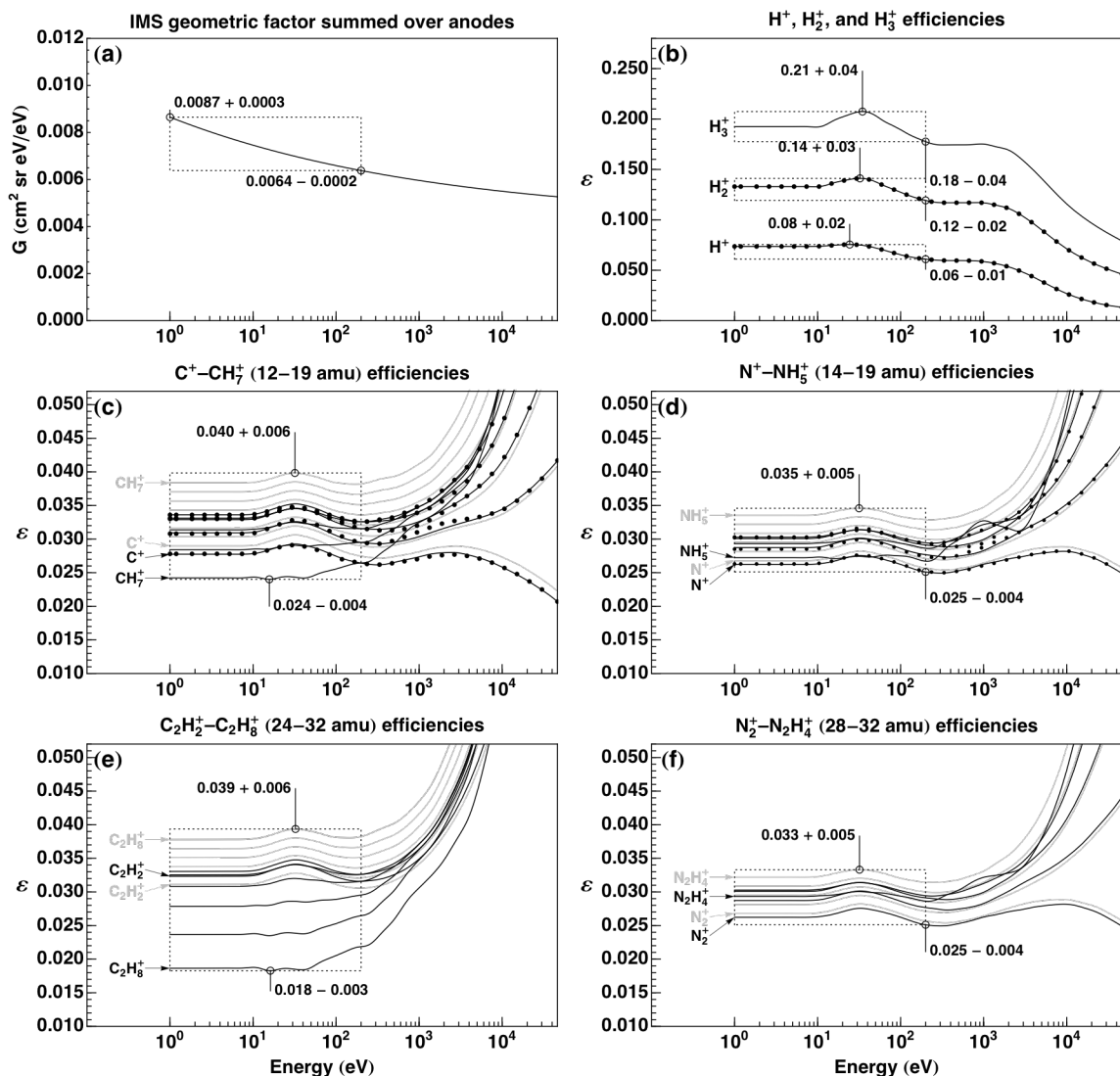
Figure 3.9.3. IMS TOF detection efficiencies

Geometric factor **(a)** and neutral-fragment efficiencies **(b)**–**(f)** versus energy for all fitted mass groups. Black points represent available simulated data. Gray curves denote linear extrapolations of the simulated data, which overestimate the true efficiencies, and black curves indicate quadratic extrapolations, which underestimate them. Dashed boxes indicate the relevant energy range and efficiency bounds for each ion group. Vertical lines represent the error in the lower and upper bounds based on the uncertainty in the efficiencies noted in the text. See pages I–XI for attributions.

The errors in the $N_{\mp}(\boldsymbol{g}_i)$ and $R_{\mp}(\boldsymbol{g}_i)$ from equations (3.9.5) and (3.9.4), respectively, were determined from the errors in the various efficiencies as well as those for the fitted background and peak areas. The relative error in the geometric factor—calculated from high-resolution numerical instrument simulations—is very low at $r_G \approx \pm 3\%$ while the error for the neutral-fragment detection efficiencies range from $r_\varepsilon \approx \pm 22\%$ to $\pm 26\%$ (D. Reisenfeld, personal correspondence, 2014). Since my efficiency extrapolation likely under/overestimates the true lower/upper bound by ~10% already, I use a somewhat smaller value of $r_\varepsilon = \pm 15\%$ for the additional error in my efficiency bounds. Relative errors in the fitted background and peak areas were calculated from our jackknife samples and added in quadrature with r_G and r_ε to obtain relative errors, $r_{N\mp}(\boldsymbol{g}_i)$, for the ion fluences of equation (4). Finally, relative errors for the *relative* fluences, $r_{R\mp}(\boldsymbol{g}_i)$, were propagated in quadrature from the $r_{N\mp}(\boldsymbol{g}_i)$ in accordance with equation (3.9.5). Individual values for the $r_{N\mp}(\boldsymbol{g}_i)$ are printed in Figure 3.9.4 along with relative errors in total ion fluence, $r_{N_{tot}\mp}(\boldsymbol{g}_i)$, for each B-cycle.
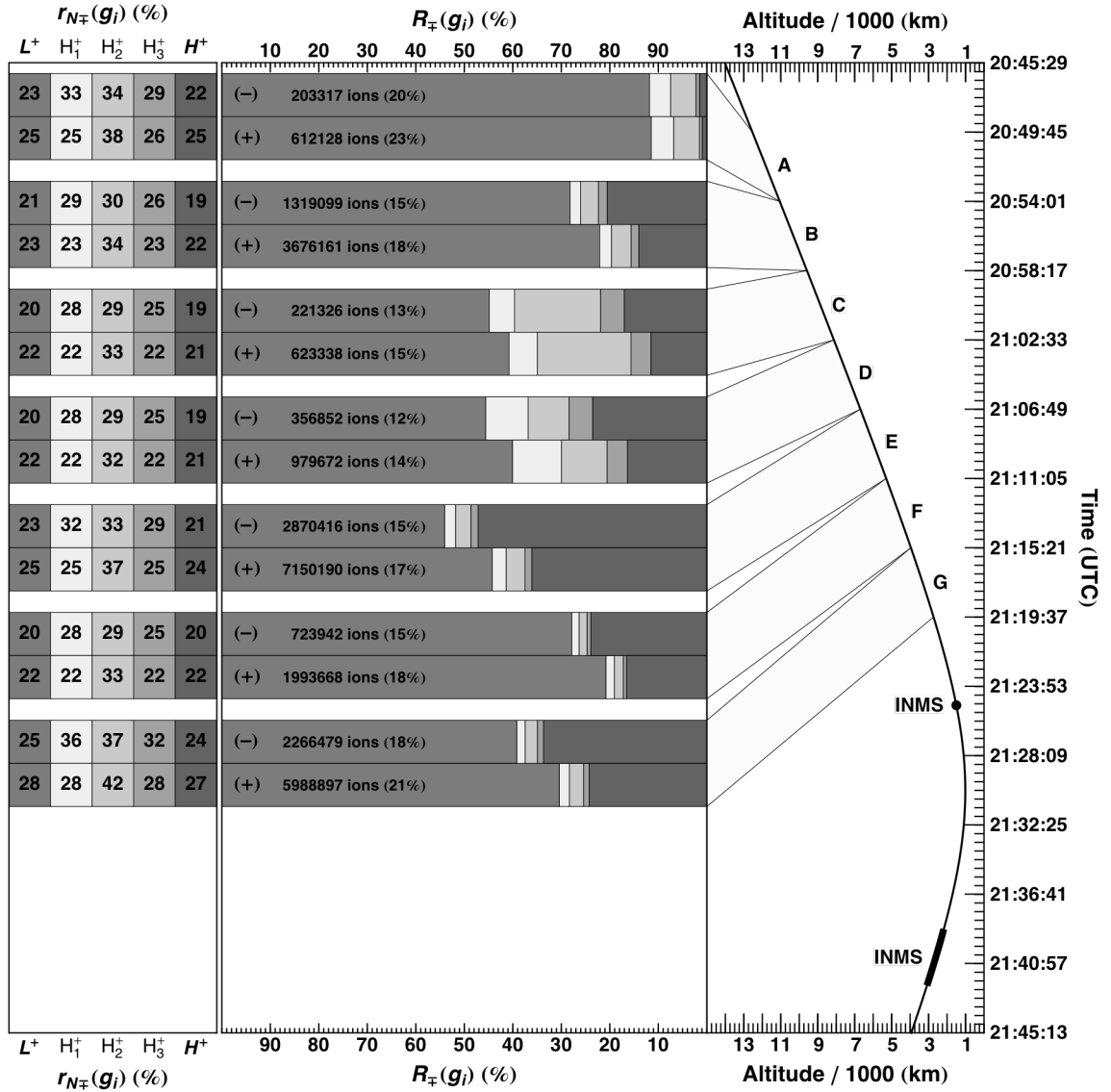
Figure 3.9.4. T40 relative ion group fluences

Relative fluences for each fitted ion group normalized to total fluence for each B-cycle. Relative errors for the $N_{\mp}(\boldsymbol{g}_i)$ from equation (3.9.5) are printed at left and altitude ranges are plotted at right. The center panel plots the $R_{\mp}(\boldsymbol{g}_i)$ of equation (3.9.4), where each relative fluence is measured as the width of the corresponding bar and group shading is indicated in the left panel. Lower and upper bounds on the total fluence for each B-cycle have been overlaid in the center panel with relative errors given in parentheses. See pages I–XI for attributions.

In this study, ion group densities are estimated from

$$n_{\mp} = N_{\mp}/(\tau \, v_{\pm} \, a_{\mp}) \,, \qquad\qquad (3.9.9)$$

where n is the number of ions per unit volume, N is the total number of ions

collected during a given B-cycle from equation (3), τ is the collection time, $v =$

$\sqrt{2\,E/m}$ is a representative ion velocity, a is the energy-dependent effective area of

the IMS entrance aperture, and the subscripts again indicate lower and upper

bounds. Lower and upper bounds on N were described above. Based on the extent of the

SNG peaks plotted in Figure 3.7.1, I assume that ions were collected only during

intervals 1 through 8, each of which spans 3 A-cycles. The collection time, $\tau = 9.1875$

seconds, thus corresponds to the dwell time (minus dead time) for 7 energy levels over 3

A-cycles, where 7 energy levels is the approximate maximum peak width in the energy

profiles in Figure 3.7.4. Since I have not yet determined the velocity distribution

associated with each ion group, I instead calculate representative velocities using the

average mass of each group and energies indicated by the vertical dashed lines in Figure

3.7.4. For the L^+ group I set $E_- = E_+$ since there is only one energy peak per interval.

However, for the bimodal portion of each spectrum, associated with M^+ and H^+, E_- and

E_+ are taken to be the energy levels nearest to the lower and upper peaks, respectively.

Finally, I estimate the minimum and maximum effective entrance areas from the

geometric efficiency of equation (1) as

$$a_- = 1\ \Gamma(E_+)\ a_0$$

and   (6)

$$a_+ = 5\ \Gamma(E_-)\ a_0\ ,$$

where two sectors to either side of the peak encompasses the majority of ions entering the collimator based on the angular distributions in Figure 3.7.2.

Furthermore, I assume limiting values for the energy imparted to ions by the surface potential of the charged spacecraft. The spacecraft is approximated as a point conductor at potential $-2\ \mathrm{V} \leq U_{sc} \leq 0\ \mathrm{V}$ such that singly charged positive ions are accelerated toward it through a potential difference of $-U_{sc}$ and gain an amount of kinetic energy equal to $q\ U_{sc}$, where q is the fundamental charge of the proton. Figure 3.9.5 illustrates the range of velocities obtained by various ions accelerated in this way. The expression for the velocity of a singly charged positive ion with mass m_{ion} entering a particular sector of the IMS entrance collimator is approximated as

$$\boldsymbol{v}_{ion} = \sqrt{\frac{2\ (E_{ESA} + q\ U_{sc})}{m_{ion}}}\,(-\boldsymbol{d}_j) + \boldsymbol{v}_{sc}\ ,\qquad(3.9.11)$$

where $\boldsymbol{v}_{sc}$ is the spacecraft velocity vector and the square root term is the velocity of the ion relative to the spacecraft, including the contribution from the spacecraft charging potential, U_{sc}. The energy setting of the electrostatic analyzer, E_{ESA}, is associated with the relative ion velocity, and $\boldsymbol{d}_j$ is a unit vector pointing outward

along the axis of the collimator's *j*th sector. For each three-A-cycle measurement interval we select *j* to correspond to the sector in which the total ion counts peaked during that interval. These sectors are colored white in Figure 3.7.2 and denoted by thick gray line segments in Figure 3.9.6.
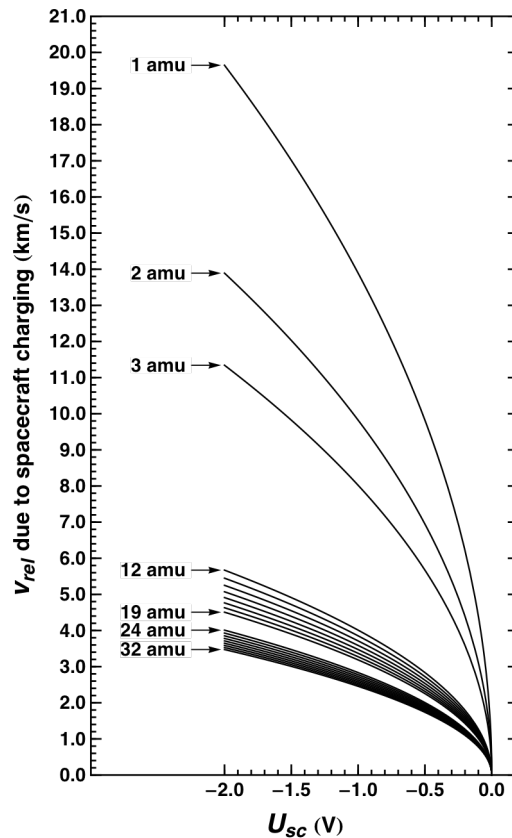
Figure 3.9.5 Ion velocities due to spacecraft charging potential

Estimated ion velocities, relative to the spacecraft, resulting from spacecraft-charging electric potentials between 0 and -2 V. A curve is provided for each fitted ion. The spacecraft is approximated as a point-source at potential $U_{sc} \leq 0$ V such that positive ions are accelerated toward the spacecraft through a potential difference of $-U_{sc}$. See pages I–XI for attributions.

Spacecraft velocity and IMS pointing
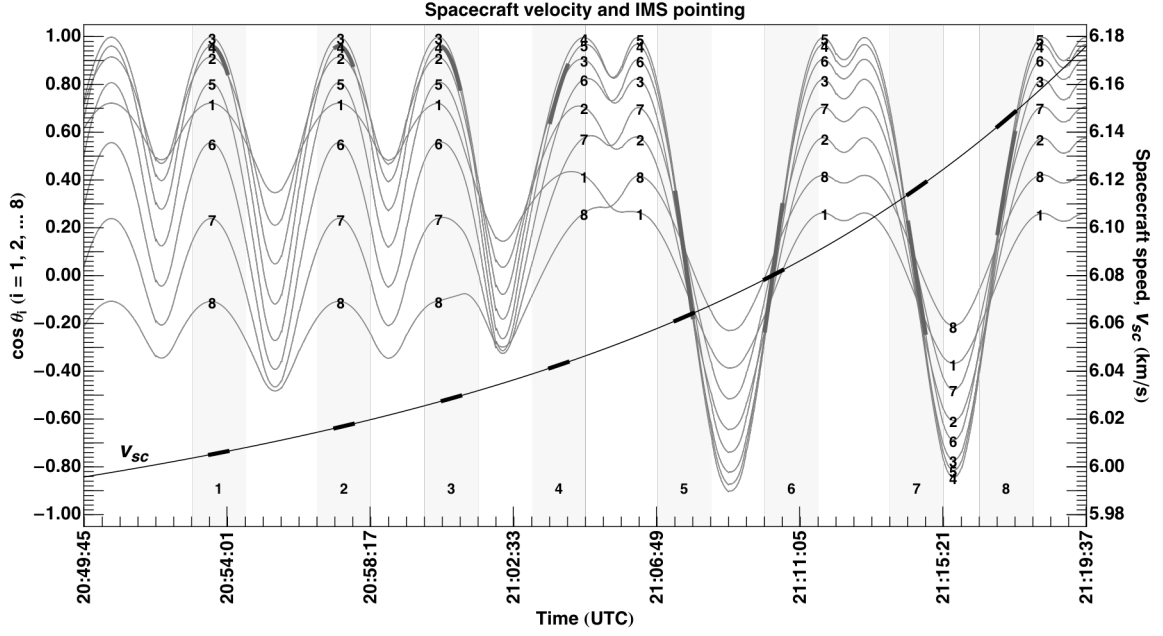
Figure 3.9.6. Spacecraft velocity and IMS pointing

Plot of the spacecraft speed (black curve) and the cosine of the angle between the

spacecraft velocity and each sector of the IMS entrance collimator (light gray curves).

The cosine curve for each of the 8 sectors is labeled with the corresponding index. For

each of the 8 numbered measurement intervals in Figure 3.3.1 a thick gray line segment

indicates the sector and A-cycle in which the total ion count peaked, which is also

geometrically depicted in Figure 3.7.2. Similarly, thick black segments correspond to the

spacecraft speed during each of the peak A-cycles. See pages I–XI for attributions.

    Based on Eq. 3.9.11 the ion speed is given by

$$v_{ion} = \sqrt{v_{sc}^2 + \frac{2\,(E_{ESA} + q\,U_{sc})}{m_{ion}} - 2\,v_{sc}\sqrt{\frac{2\,(E_{ESA} + q\,U_{sc})}{m_{ion}}}\cos\theta_j}\,, \qquad (3.9.12)$$

84

where θ_j is the angle between $\boldsymbol{v}_{sc}$ and $\boldsymbol{d}_j$. Figure 3.9.6 plots the spacecraft speed and

$\cos \theta_j$ for each sector of the entrance collimator as a function of time for the duration of

the encounter. Equation (3.9.12) is averaged over the peak A-cycle of each interval, as

shown in Figure 10, using all combinations of $E_{ESA} \in \{E_-, E_+\}$ and $U_{sc} \in \{U_-, U_+\}$

with $U_- = \max(-2 \text{ V}, -E_{ESA}/q)$ and $U_+ = 0 \text{ V}$. The expression for U_- reflects the

requirement that energy imparted by the spacecraft charging potential cannot

exceed the total measured energy of the ion. Figure 3.9.8 shows the lowest and highest

velocities obtained in this way, which converge to the light-ion velocities calculated by

Westlake et al. [2012], but are slightly higher than their medium- and heavy-ion

velocities. Relative errors for these velocity and density limits were calculated from

$$r_{v\pm} = \frac{1}{v_\pm} \sqrt{s_v^2 + \left(\left| \frac{\partial v}{\partial E} \right|_{E_\pm} \frac{r_E \, E_\pm}{2} \right)^2} \qquad (3.9.13)$$

$$r_{n\mp} = \sqrt{r_{N_\mp}^2 + r_{v_\pm}^2 + r_{a_\mp}^2} \,, \qquad (3.9.14)$$

where s_v is the standard error in the average of Eq. 3.9.12 over a given interval, the

$\partial v / \partial E$ term is the error associated with the energy resolution, and $r_{a\,-/+} = r_G$. In

calculating the density limits for intervals 5 and 6 I have partitioned the ions collected

during B-cycle E in proportion to the SNG counts in those intervals, resulting in slightly

larger error bars. The final velocity and density limits are plotted against time and altitude

in Figure 3.9.8. As a check on methodology I compared total electron densities calculated

from concurrent CAPS ELS measurements against my estimated IMS densities. These electron densities were graphically extracted from Figure 3.9.7, at 1-minute intervals over the reliable regions indicated by the green line, and plotted against the estimated densities in the right half of Figure 3.9.8. This juxtaposition will be discussed further in the next section.
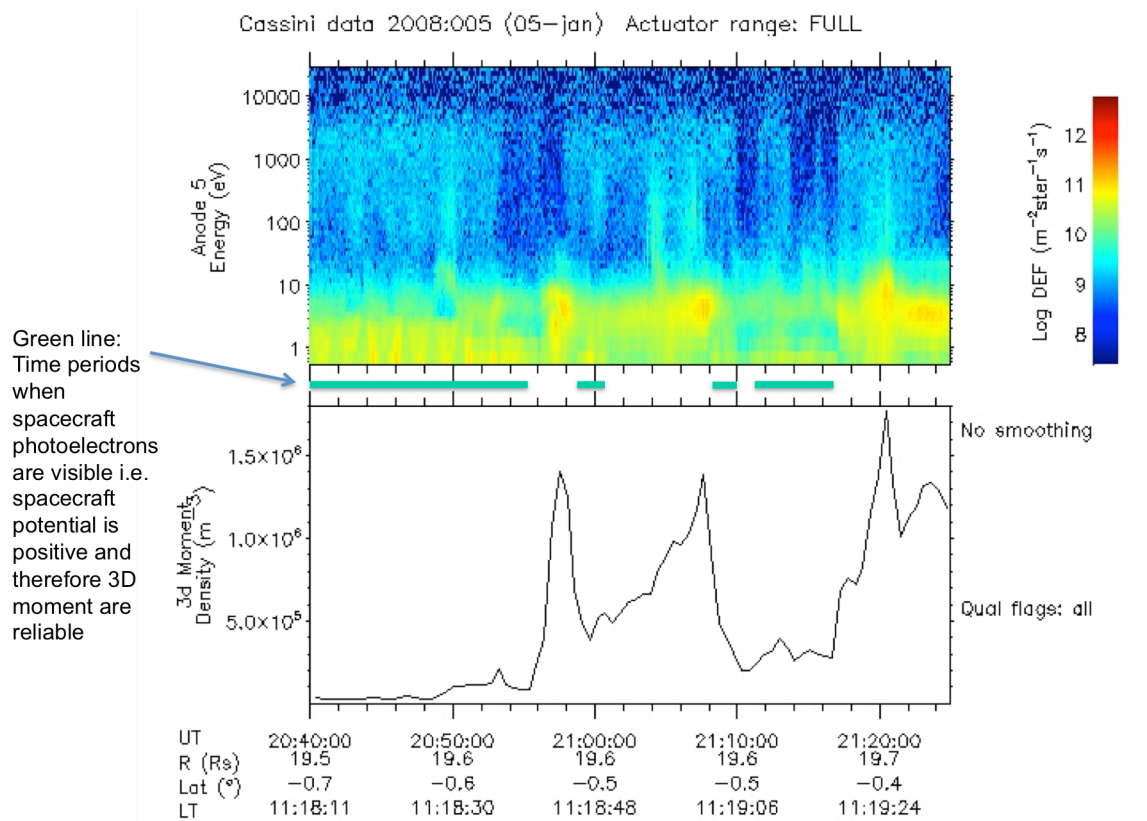
Figure 3.9.7. CAPS ELS electron densities

Electron densities calculated by A. Wellbrock from CAPS Electron Spectrometer data acquired on ingress during the T40 Titan encounter. See pages I–XI for attributions.
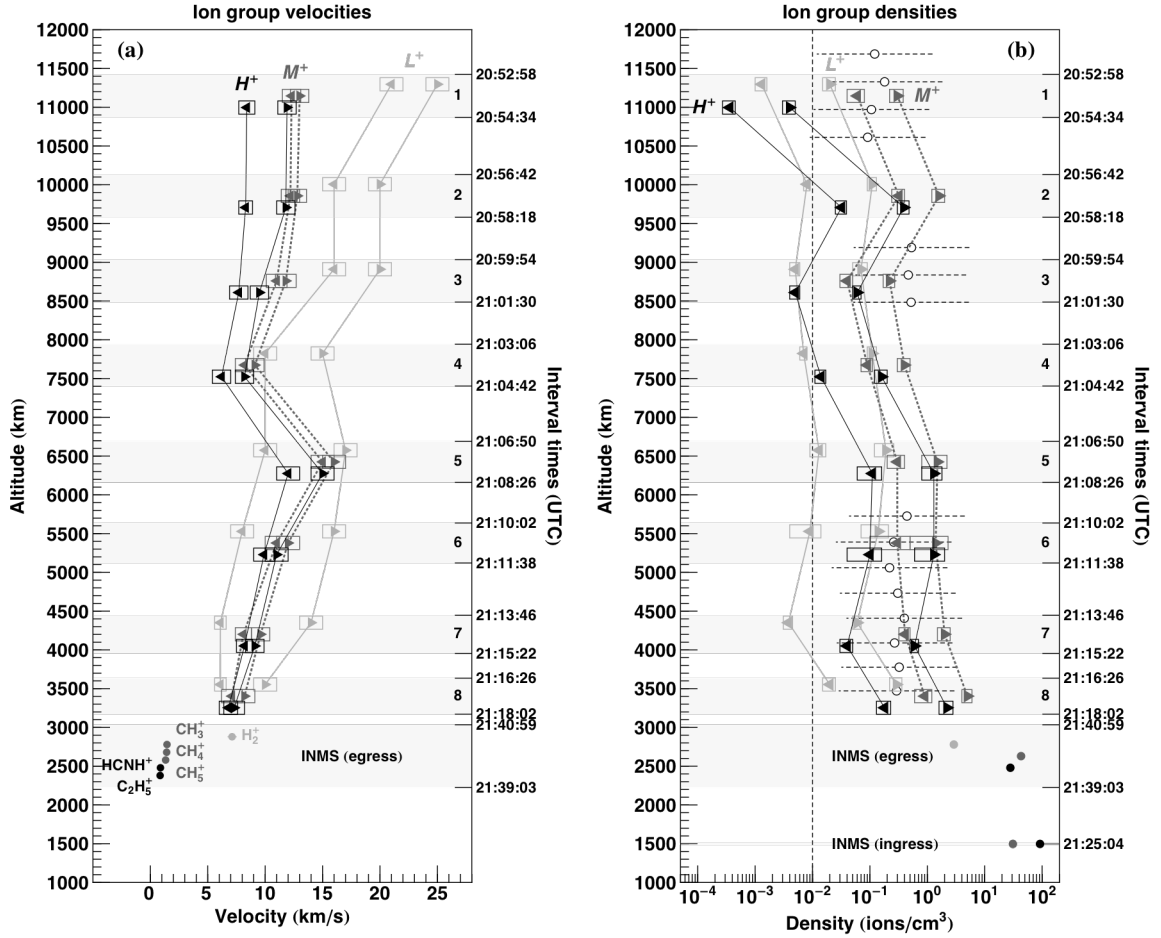
Figure 3.9.8 T40 Ion group velocities and densities extracted from IMS data

(a) Lower bounds (leftward triangles) and upper bounds (rightward triangles) for L^+ (solid, light gray), M^+ (dotted, gray) and H^+ (solid, black) group velocities averaged over each shaded interval. The error in each value is indicated by the width of the associated rectangle. INMS velocites (filled circles) were calculated by Westlake et al. [2012] at 2863 km on egress. **(b)** Lower and upper bounds on L^+, M^+ and H^+ ion group densities. INMS densities from Westlake et al. [2012] have been group-summed for comparison (filled circles) and ELS electron densities at various altitudes along ingress are plotted as open circles with horizontal dashed lines indicating one order of magnitude to either side. A vertical dashed lines indicates the density corresponding to black in L2012. See pages I–XI for attributions.

3.10 Comparing data to interaction models

The interaction between Titan's upper atmosphere and Saturn's magnetospheric fields and plasma have been modeled by Sillanpää et al. [2006] and Ledvina et al. [2012]—hereafter S2006 and L2012 respectively—based on the ambient conditions of the Voyager 1 flyby, which were similar to those during the T40 encounter. However, under the same conditions the S2006 model predicts an ion tail that leans Saturnward while the L2012 model predicts an anti-Saturnward orientation. Presumably, then, a difference in implementation between the two models leads to divergent tail structures that can be validated or invalidated against a sufficient body of CAPS IMS data acquired in Titan's wake. Here I will very briefly summarize a number of the similarities and differences between the models, but the readier is referred to the articles cited for further details.

Both simulations employ self-consistent, quasi-neutral hybrid models that treat ions as kinetic particles and electrons as a massless, charge-neutralizing fluid. However, in addition to spatial resolution, the implementations differ in a number of key elements. In the S2006 model the local effects of charged particles on electric and magnetic fields are omitted, while in the L2012 model the frictional drag produced by ion-neutral collisions is allowed to alter electric and magnetic fields below the exobase through changes in the local conductivity. S2006, in contrast, treats Titan's exobase as an absorbing, fully conducting boundary from which ions with mass 28 amu are emitted uniformly with an assumed density and temperature. A second source generates mass 16

ions through exospheric photoionization using a Chamberlain function to describe the exospheric density profile. The L2012 model, on the other hand, simulates ion production due to ion-neutral chemistry and collisions at altitudes between 750 and 2700 km. The model uses a simplified chemistry network that groups similar species into macrospecies, including the L^+ and M^+ groups referenced throughout this study as well as two "heavy" groups—$H1^+$ and $H2^+$—consisting of $C_2H_5^+$ and $CHNH^+$, respectively. Moreover, photoionization rates are computed for dayside L^+, M^+ and $H1^+$ ions as a function of altitude and solar zenith angle using a solar minimum flux, and electron impact ionization due to Maxwellian electrons moving along magnetic field lines generates their night-side counterparts.

In both models the authors take the ambient magnetic field to be 5 nT in the southward direction and employ consistent, anti-Saturnward corotation electric fields. In S2006 the incident plasma consists of a single species with the average mass of hydrogen and nitrogen as weighted by their relative abundances in the plasma. Plasma ions are introduced with a bulk velocity of 120 km/s in the orbital direction and a velocity distribution consistent with a hot, subsonic flow. In L2012, however, the incident plasma is taken to consist of warm electrons in addition to cold (highly collimated) O+ ions corotating at 120 km/s.

Although not exact, conditions during the T40 encounter were similar to the ambient conditions utilized in these simulations. As discussed in Section 3.4 both Rymer et al. [2009] and Simon et al. [2013] characterize the ambient magnetic field as partially

sheet-like, having a southward orientation, on average, near the orbital plane. Based on the model of Wei et al. [2011] also discussed in section 3.4 it is unlikely that the plasma sheet would have been highly distorted by the solar wind during the T40 encounter, so that the southward ambient field direction implemented in both models coincides with the direction perpendicular to both the plasma sheet and Titan's orbital plane. Moreover, plasma moments obtained from Los Alamos National Laboratory (www.caps.lanl.gov/sur_anl_tool.html) confirm an average plasma corotation velocity of ~140 km/s similar to that used in the models, and an average (warm) velocity of ~35 km/s transverse to corotation. Lastly, both S2006 and L2012 simulated Titan's interaction at 12:00 SLT in accordance with the T40 encounter, which took place near 11:30 SLT.

In Figure 3.9.1 I have overlaid Cassini's path along with the IMS-derived ion densities onto the S2006 and L2012 model results. Figures have been graphically extracted from their respective articles and carefully cropped and rescaled for comparison. In addition, the figures from S2006, shown in panels (a) and (b), have been rotated by 180° and negated so that black indicates minimum density and white maximum density as it does in the figures extracted from L2012. Solid yellow lines are planar projections of Cassini's path, while the dashed yellow lines represent cross-sections of the nominal exobase and field-draping and mass-loading boundaries from Ulusen et al. [2012] (hereafter U2012). While the spacecraft trajectory was not confined to the orbital plane during the encounter, it's inclination was less than 30° and all measurements were acquired within ~2 R_T of the orbital plane as can be seen in Figure 3.3.1. Note that in the density plots presented in S2006 black corresponds to a density of

zero while in those from L2012 black represents a density $\leq$ 0.01 ions/cm^3.

Since I have not determined individual ion densities I instead compared the IMS-derived $\boldsymbol{M}^+$ densities with the CH_4^+ densities from S2006, and the IMS-derived $\boldsymbol{H}^+$ densities with both the $\boldsymbol{H1}^+$ and $\boldsymbol{H2}^+$ densities from L2012. In the black regions where L2012 shows no tail structure and indicates densities below 0.01 ions/cm^3 the IMS-derived upper-bound $\boldsymbol{L}^+$, $\boldsymbol{M}^+$, and $\boldsymbol{H}^+$ densities exceed that threshold by a few times to several orders of magnitude in all intervals except the first, during which the $\boldsymbol{M}^+$ upper-bound densities fall below the threshold. Moreover, while the IMS-derived lower-bound $\boldsymbol{L}^+$ densities fall predominantly below the threshold, the lower-bound $\boldsymbol{H}^+$ densities exceed it over all but two intervals and the lower-bound $\boldsymbol{M}^+$ densities exceed it everywhere by at least an order of magnitude. Note as well that the majority of the IMS-derived density estimates are within an order of magnitude of the electron densities measured by CAPS ELS during T40 ingress as seen in Figure 3.9.7 (A. Wellbrock, personal correspondence, 2014). Meanwhile, all densities are within the range of values presented in S2006.

The preceding comparison demonstrates that the S2006 interaction model reproduces an ion tail geometry for T40-like encounters that is consistent with the data in the half of the wake sampled by IMS. In further support of this conclusion, note that the first appearance of the $\boldsymbol{M}^+$ group in the TOF spectra agrees well with both the edge of the S2006 ion tail and the field-draping boundary predicted by U2012. However, a more thorough comparison is to be conducted using multiple encounters and more precise calculations of the IMS ion densities in order to verify the ubiquity of these results.
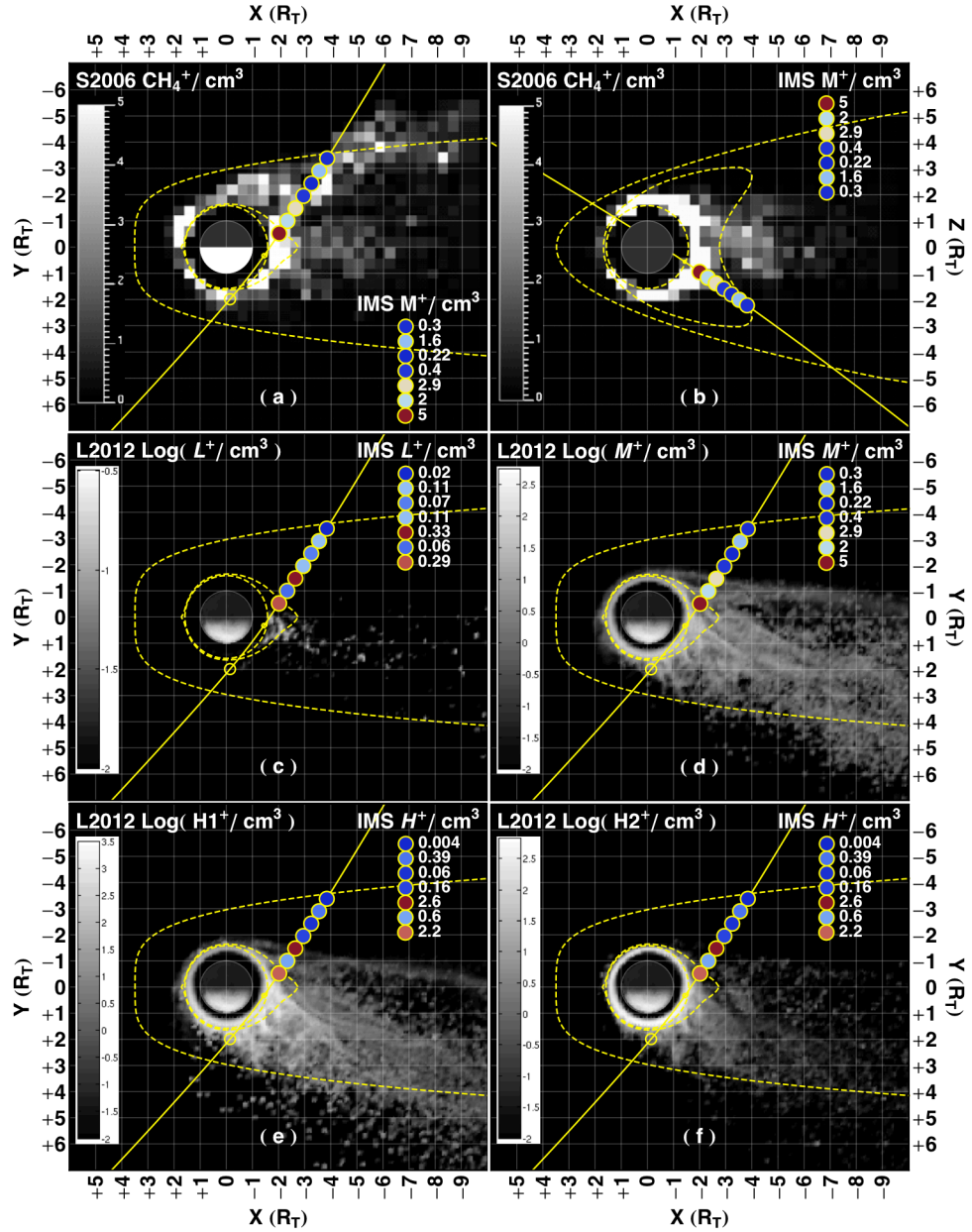
Figure 3.10.1 Comprison of simulated and measured ion densities

Colored circles indicate upper-bound ion densities per B-cycle based on the IMS data. **(a)** and **(b)** are taken from S2006 and **(c)**–**(f)** from L2012. All panels except **(b)** represent model densities in the orbital (XY) plane. Densities in the XZ plane were not reported in L2012. Yellow lines indicate Cassini's trajectory, the nominal exobase, and the boundaries of U2012. Open circles pinpoint the INMS measurements. See pages I–XI for attributions.

4. Future Work

As discussed, this research ultimately seeks to quantify atmospheric loss at Titan in each of the magnetospheric environments that the moon encounters. In this section I briefly discuss how the methods developed herein will be extended and applied in order to achieve this goal.

4.1 Fitting the IMS SNG spectra

In this thesis I estimated ion group densities using "representative" velocities; that is, velocities calculated at the peak energies in the T40 SNG spectra and using the instrument pointing associated with those peaks. However, a more accurate ion group density can be calculated by generalizing Eq. 3.9.9 and integrating over the partial velocity distribution for each group,

$$n(\boldsymbol{g}) = \sum_j \sum_i \frac{N(\boldsymbol{g}, E_i, \boldsymbol{d}_j)}{v(E_i)\, a(E_i)\, \tau(E_i)}, \qquad (4.1.1)$$

where $\{E_i\}$ is the set of energies sampled by the ESA, $\{\boldsymbol{d}_j\}$ is the set of A-cycle averaged pointing vectors for each sector of the IMS collimator, $\tau(E_i)$ is the A-cycle integrated dwell time at energy E_i, $v(E_i)$ is the ion velocity relative to the spacecraft , $a(E_i)$ is the energy-dependent effective aperture area for a single sector of the collimator, and $N(\boldsymbol{g}, E_i, \boldsymbol{d}_j)$ is the number of $\boldsymbol{g}$ ions with energy E_i moving in direction $\boldsymbol{d}_j$ relative to the

spacecraft. Using this method, the $N(\boldsymbol{g}, E_i, \boldsymbol{d}_j)$ will be determined by weighting the $N(\boldsymbol{g})$

of equation 3.9.5 with the SNG counts,

$$N(\boldsymbol{g}, E_i, \boldsymbol{d}_j) = \frac{C(\boldsymbol{g}, E_i, \boldsymbol{d}_j)}{C_{Tot}} N(\boldsymbol{g}). \qquad (4.1.2)$$

where $C(\boldsymbol{g}, E_i, \boldsymbol{d}_j)$ is the number of SNG counts associated with ion group $\boldsymbol{g}$ at energy

level E_i coming from direction $\boldsymbol{d}_j$. Recall that since $N(\boldsymbol{g})$ represents the number of ions

entering IMS during a given B-cycle, C_{Tot} must be the sum of SNG counts over all A-

cycles occurring within that B-cycle.

Similar to the way in which the $C(\boldsymbol{g})$ of Eq. 3.9.6 are determined by partitioning

TOF counts according to ion-group peak fits, as shown in Figure 3.8.5, the $C(\boldsymbol{g}, E_i, \boldsymbol{d}_j)$

can be determined by partitioning the SNG counts according to each group's fitted energy

peak. This task will be accomplished in a straightforward manner with few modifications

to the numerical tools that I have already developed; namely, the addition of a suitable

model function. As mentioned in Section 3.1, Tokar et al. [2005] used an isotropic,

convective Maxwellian—so called because the Maxwellian is isotropic in a frame

moving at the bulk flow velocity—to model water-group ions in SNG spectra acquired

near Saturn's main rings. Similarly, Nemeth et al. [2011] used a Maxwell-like model

consisting of a sum of exponential functions of the form

$$f(x) = A_0 + A_1 \exp[-A_3 (x - A_2)^2] + A_4 \exp[-A_6 (x - A_5)^2] \qquad (4.1.3)$$

where no assumptions were made about bulk velocity and the coefficients, $A_0 \cdots A_6$, were allowed to very as needed to fit each spectrum. Figure 4.1.1 shows their fit results for the T39 encounter.
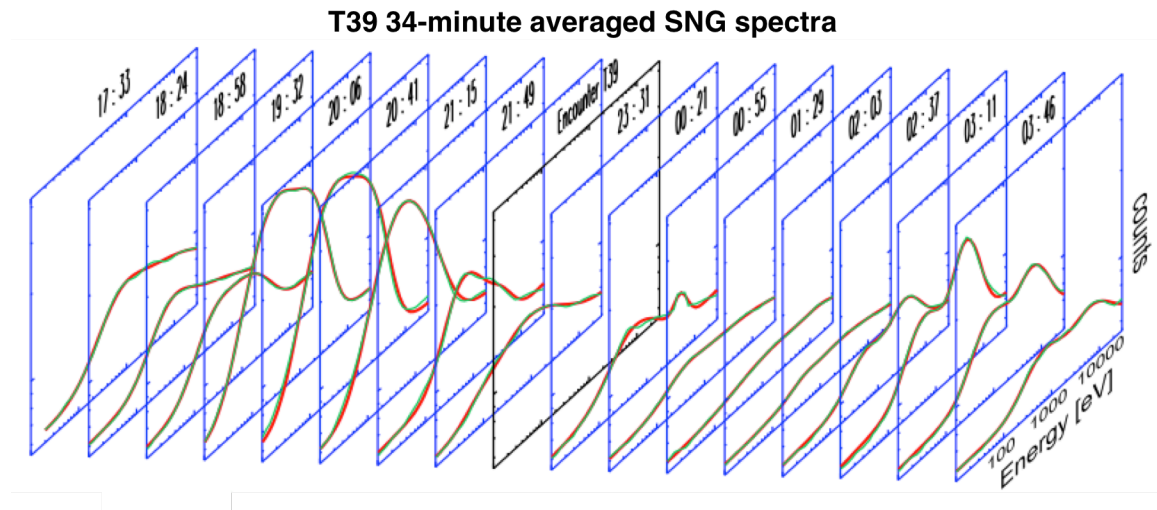
Figure 4.1.1 SNG peak fitting example for T39

Several time-averaged SNG spectra fitted with a sum of Maxwell-like exponential functions. See pages I–XI for attributions.

As a first approximation I intend to use a general sum of Maxwell-like functions similar to Eq. 4.1.3 but with the addition of one or more exponentials to account for hydrogen peaks. The T40 SNG spectra from Figure 3.7.4 have been replotted in Figure 4.1.2 for comparison with the T39 spectra above. Along with the TOF fits, these SNG fits will then be used to calculate improved ion group densities and velocities for each Titan encounter, with higher temporal resolution than those calculated in Section 3.9.
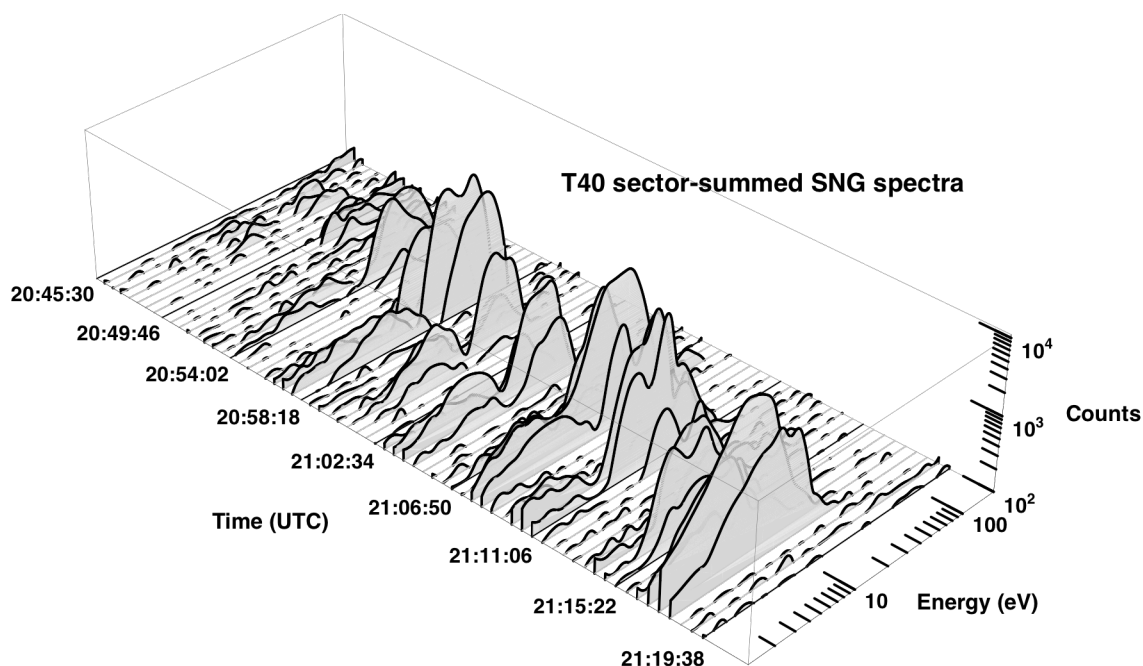
Figure 4.1.2 3D rendering of T40 SNG spectra

See pages I–XI for attributions.

4.2 Analysis of all Titan encounters

Figure 4.2.1 shows sector-summed SNG spectra acquired within ~1 hour of Titan during all encounters for which both SNG and TOF data exist. Gray panels in the figure indicate encounters for which either SNG or TOF data is missing. Although CAPS was turned off temporarily between encounters T76 (May 8th, 2011) and T83 (May 22nd, 2012), and then shut down permanently after T83, I have plotted encounters up to T88 for symmetry.
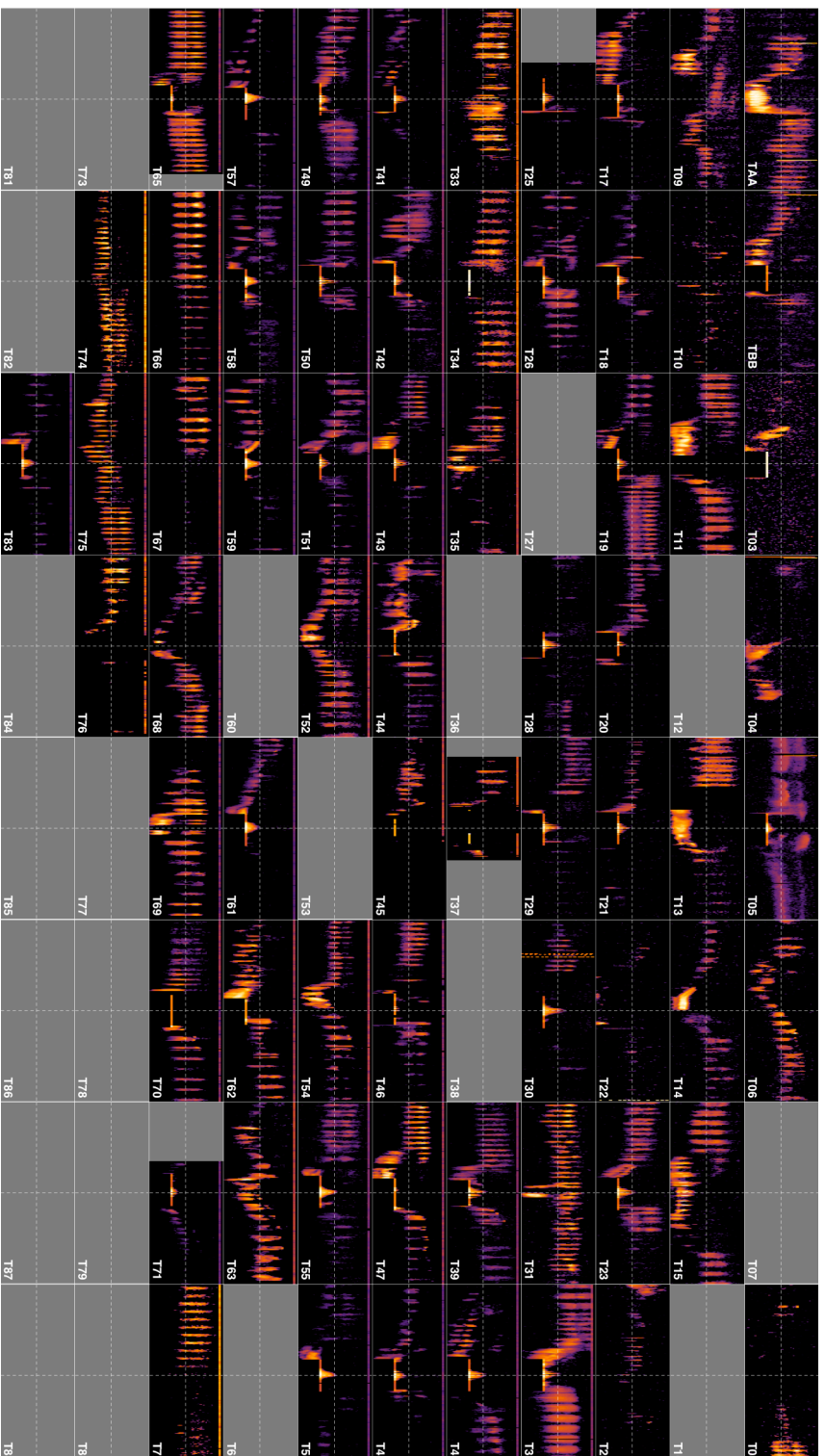
Figure 4.2.1 Sector-summed SNG spectra acquired near Titan

A collage of all available SNG spectra within ~1 hour of closest approach (CA). In each panel, CA is denoted by a vertical dashed ine and a horizontal one indicates an ESA energy of 200 eV. The energy scale is logarithmic and runs from 1 eV at the bottom to 50 keV at the top of each panel. Gray indicates missing data. See pages I–XI for attributions.

At the center of each spectrum a vertical dashed line denotes closest approach (CA), and a horizontal dashed line indicates an energy of 200 eV. In most cases a substantial drop in the ambient ion energy is observed around CA, delimiting a transition from the high-energy, corotating water-group population to the lower-energy hydrocarbon population and back again. In some cases (e.g. T15) the boundary between the two populations is obvious, while in other cases it may be more difficult to discern (e.g. T69). In the latter cases, however, the location of the boundary becomes clear from looking at the energy-integrated TOF spectra. Figure 4.2.2 illustrates this for the case of T69 where Cassini crosses the boundary from water group to hydrocarbons between 2:13:32 and 2:17:48 UTC on ingress, and from hydrocarbons back to water group between 2:30:36 and 2:34:52 UTC on egress.

Using plots like the one shown in Figure 4.2.2 I have surveyed all of the Titan encounters and selected the B-cycles in which only hydrocarbon peaks are observed above ST TOF channel 350, revealing that all such ions have energies below ~200 eV. This allows the methods developed in this thesis to be applied to all of the encounters shown in Figure 4.2.1. Specifically, since the LPP peak calibrations are insensitive to changes in energy below ~200 eV as shown in Figure 3.8.4, and since the LPP parameter ranges input to the DE algorithm are energy dependent, I can use a single DE parameter file to process all of the selected B-cycles. I will then use the resulting TOF fits, combined with the SNG fits described in Section 4.1, to calculate the range of heavy-ion velocities and densities in Titan's exosphere. These velocities and densities will, in turn, be used to estimate heating due to ion-neutral collisions in Titan's upper thermosphere

which, according to De La Haye et al. [2007], may be the primary mechanism of permanent atmospheric loss at Titan.
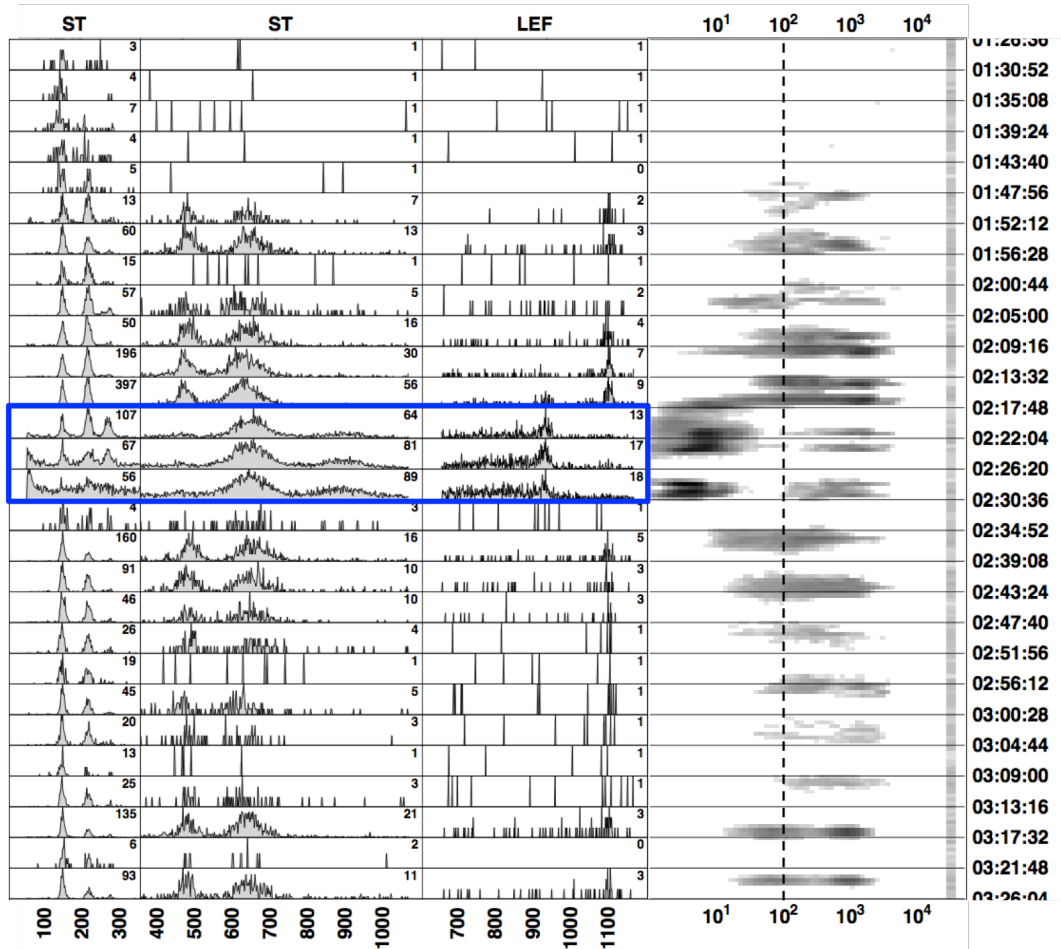
Figure 4.2.2 T69 TOF spectra and SNG spectrogram

Energy-summed TOF spectra per B-cycle within ~1 hour of CA, juxtaposed with the sector-summed SNG spectrogram. Each spectrum is scaled for best viewing. The B-cycles between 2:17:48 and 2:30:36 UTC (blue box) are comprised of hydrocarbons above ST channel 500, while the adjacent cycles show clear evidence of water group peaks between ST channesl 350 and 550, and near LEF channel 1100. See pages I–XI for attributions.

99

5. Conclusion

One impetus for studying this particular Titan encounter was the realization that the INMS had fortuitously sampled the wake composition during the same encounter. Here I have used the INMS composition measured during the T40 encounter as a guide in selecting model peaks for data fitting. Of particular interest are carbon- and nitrogen-bearing ions in mass ranges 12–19 (M^+) and 24–32 (H^+) that were seen by both instruments. In addition to these masses I have quantified the abundance of H^+, H_2^+ and H_3^+ (L^+) present in the TOF spectra and mapped all abundances against time and altitude. Hydrocarbons are first detected by CAPS IMS on ingress at an altitude of ~11,000 km in good agreement with both the field-draping boundary modeled by U2012 and the O^+ "clearing region" observed by Hartle et al. [2006a] in their analysis of the TA encounter.

Notably, I observe a clear peak in the TOF spectra associated with H_3^+, which has not been reported previously in Titan's interaction region. While the H_3^+ peak overlaps with a known ghost peak that results from H^+ scattering inside the instrument, the height of the ghost peak is typically a small fraction (1–10%) of the primary H^+ peak height (M. Shappirio et al., unpublished data, 2007) and its asymmetry is opposite that of ST peaks, neither of which is true for the H_3^+ peak identified here. This molecular ion is likely formed in a region of significant H_2 density and then carried into the far wake by the ionospheric outflow.

I have shown that the CAPS IMS data supports the Saturnward ion tail predicted by the hybrid interaction model of S2006 and agrees with the wake boundary position predicted by the pure MHD model of U2012 for T40-like encounters. In terms of the boundary location, M^+ first appears in the CAPS IMS data when Cassini crosses the field-draping boundary, which is most easily inferred from the geometry in Figure 3.3.1, and the appearance of M^+ coincides well with the edge of the CH_4^+ distribution plotted in S2006. I have also calculated lower- and upper-bound densities for L^+, M^+ and H^+ based on IMS data and compared those estimates with the simulated densities. The IMS-derived upper-bound densities in the Saturnward flank of Titan's wake are several times to several orders of magnitude larger than those predicted by L2012 and of similar magnitude to those predicted by S2006, while in most cases the lower-bound densities exceed those of L2012 as well. Furthermore, nearly all of the extracted density values fall within an order of magnitude of the electron densities measured by CAPS ELS during T40 ingress. I expect that a rigorous moment calculation incorporating the data's full angle and energy distribution will more precisely constrain the densities between these lower and upper bounds.

A visual survey of all TOF spectra within 10 R_T of Titan suggests that the methods used here can be applied to most Titan encounters. The energy ranges of ions in Titan's wake lie predominantly below a few hundred eV where the model peak shapes and positions are relatively insensitive to changes in energy. This allows ST spectra to be integrated over energy to obtain sufficient counts for fitting and model peaks to be characterized by the median energy of the observed ions. Deconvolution of the energy

profiles in Figure 3.7.4, combined with similar analyses of multiple Titan encounters, will

yield a more comprehensive picture of the ion composition in Titan's wake, estimates for

atmospheric loss due to ion-neutral collisions in the upper thermosphere, and better

constraints with which to evaluate models of Titan's plasma interaction.

5. References

Arrale, A. M., et al. "Model of the contamination effect in ion-induced electron emission." *Nuclear Instruments and Methods in Physics Research Section B: Beam Interactions with Materials and Atoms* 89.1 (1994): 437-442.

Arridge, C. S., et al. "Modeling the size and shape of Saturn's magnetopause with variable dynamic pressure." *Journal of Geophysical Research: Space Physics (1978–2012)* 111.A11 (2006).

Atreya, S. K., R. D. Lorenz, and J. H. Waite. "Volatile origin and cycles: nitrogen and methane." *Titan from Cassini-Huygens*. Springer Netherlands, 2010. 177-199.

Aumayr, F., G. Lakits, and H. Winter. "On the measurement of statistics for particle-induced electron emission from a clean metal surface." *Applied surface science* 47.2 (1991): 139-147.

Benka, O., A. Schinner, and T. Fink. "Distribution of the number of emitted electrons for MeV H+-and He 2+-ion impact on metals." *Physical Review A* 51.3 (1995): 2281.

Bertucci, C., et al. "The magnetic memory of Titan's ionized atmosphere." *Science* 321.5895 (2008): 1475-1478.

Billebaud, A., et al. "Ion-by-ion measurements of backward secondary electron emission of carbon foilsunder the impact of MeV H^+, H^0, H^-, and H_2^+ projectiles." *Physical Review A* 55.2 (1997): 1124.

Canup, R. M. "Origin of Saturn/'s rings and inner moons by mass removal from a lost Titan-sized satellite." *Nature* 468.7326 (2010): 943-926.

Charnoz, S., et al. "Accretion of Saturn's mid-sized moons during the viscous spreading of young massive rings: Solving the paradox of silicate-poor rings versus silicate-rich moons." *Icarus* 216.2 (2011): 535-550.

Clerc, H-G., et al. "Heavy-ion induced secondary electron emission—A possible method for Z-identification." *Nuclear Instruments and Methods* 113.3 (1973): 325-331.

Coates, A. J., et al. "Cassini in Titan's tail: CAPS observations of plasma escape." *Journal of Geophysical Research: Space Physics (1978–2012)* 117.A5 (2012).

Cravens, T. E. *Physics of Solar System Plasmas, pp. 495. ISBN 0521611946. Cambridge, UK: Cambridge University Press, November 2004.*

Cui, J., R. V. Yelle, and K. Volk. "Distribution and escape of molecular hydrogen in Titan's thermosphere and exosphere." *Journal of Geophysical Research: Planets (1991–2012)* 113.E10 (2008).

De La Haye, V., et al. "Cassini Ion and Neutral Mass Spectrometer data in Titan's upper atmosphere and exosphere: Observation of a suprathermal corona." *Journal of Geophysical Research: Space Physics (1978–2012)* 112.A7 (2007).

Dietz, L. A., and J. C. Sheffield. "Secondary electron emission induced by 5–30-keV monatomic ions striking thin oxide films." *Journal of Applied Physics* 46.10 (1975): 4361-4370.

Ding, L., et al. "Coincidence studies of electron emission statistics in ion surface interactions: a new experimental study." *PHILOSOPHICAL TRANSACTIONS-ROYAL SOCIETY OF LONDON SERIES A MATHEMATICAL PHYSICAL AND ENGINEERING SCIENCES* (1999): 1381-1390.

Dones, L., et al. "Icy satellites of Saturn: Impact cratering and age determination." *Saturn from Cassini-Huygens*. Springer Netherlands, 2009. 613-635.

Dubus, A., et al. "Comparison between theory and experiments for the electron emission statistics induced by protons incident on thin carbon foils." *Nuclear Instruments and Methods in Physics Research Section B: Beam Interactions with Materials and Atoms* 125.1 (1997): 45-48.

Elrod, M. K., et al. "Seasonal variations in Saturn's plasma between the main rings and Enceladus." *Journal of Geophysical Research: Space Physics (1978–2012)* 117.A3 (2012).

Hartle, R. E., et al. "Preliminary interpretation of Titan plasma interaction as observed by the Cassini Plasma Spectrometer: Comparisons with Voyager 1." *Geophysical research letters* 33.8 (2006a).

Hartle, R. E., et al. "Initial interpretation of Titan plasma interaction as observed by the Cassini plasma spectrometer: Comparisons with Voyager 1." *Planetary and Space Science* 54.12 (2006b): 1211-1224.

Hill, T. W., Thomsen, M. F., Henderson, M. G., Tokar, R. L., Coates, A. J., McAndrews, H. J., ... & Young, D. T. (2008). Plasmoids in Saturn's magnetotail. *Journal of Geophysical Research: Space Physics (1978–2012)*, *113*(A1).

Hansen, C. J., et al. "Enceladus' water vapor plume." *Science* 311.5766 (2006): 1422-1425.

Hansen, C. J., et al. "Water vapour jets inside the plume of gas leaving Enceladus." *Nature* 456.7221 (2008): 477-479.

Johnson, R. E. "The magnetospheric plasma-driven evolution of satellite atmospheres." *The Astrophysical Journal Letters* 609.2 (2004): L99.

Johnson, R. E., et al. "Mass loss processes in Titan's upper atmosphere." *Titan from Cassini-Huygens*. Springer Netherlands, 2010. 373-391.

Kanani, S. J., et al. "A new form of Saturn's magnetopause using a dynamic pressure balance model, based on in situ, multi-instrument Cassini measurements." *Journal of Geophysical Research: Space Physics (1978–2012)* 115.A6 (2010).

Kozochkina, A. A., V. B. Leonas, and V. E. Fine. "Statistics of heavy particle-induced electron emission from a foil." *Ionization of solids by heavy particles*. Springer US, 1993. 223-237.

Ledvina, S. A., S. H. Brecht, and T. E. Cravens. "The orientation of Titan's dayside ionosphere and its effects on Titan's plasma interaction." *Earth, planets and space* 64.2 (2012): 207-230.

Ma, Y. J., et al. "Time-dependent global MHD simulations of Cassini T32 flyby: From magnetosphere to magnetosheath." *Journal of Geophysical Research: Space Physics (1978–2012)* 114.A3 (2009).

Matson, D. L., et al. "The Thermal Evolution and Internal Structure of Saturn's Mid-Sized Icy Satellites." *Saturn from Cassini-Huygens*. Springer Netherlands, 2009. 577-612.

Mauk, B. H., et al. "Fundamental plasma processes in Saturn's magnetosphere." *Saturn from Cassini-Huygens*. Springer Netherlands, 2009. 281-331.

McComas, D. J., et al. "Ultrathin (~10 nm) carbon foils in space instrumentation." *Review of scientific instruments* 75.11 (2004): 4863-4870.

Mechbach, W., G. Braunstein, and N. Arista. "Secondary-electron emission in the

      backward and forward directions from thin carbon foils traversed by 25-250 keV

      proton beams." *Journal of Physics B: Atomic and Molecular Physics* 8.14 (1975):

      L344.

Meyer-Vernet, N. *Basics of the solar wind*. Vol. 7. Cambridge: Cambridge University

      Press, 2007.

Michael, M., et al. "Ejection of nitrogen from Titan's atmosphere by magnetospheric ions

      and pick-up ions." *Icarus* 175.1 (2005): 263-267.

Michael, M., and R. E. Johnson. "Energy deposition of pickup ions and heating of Titan's

      atmosphere." *Planetary and Space Science* 53.14 (2005): 1510-1514.

Martens, H. R., et al. "Observations of molecular oxygen ions in Saturn's inner

      magnetosphere." *Geophysical Research Letters* 35.20 (2008).

Mcandrews, H. J., et al. "Plasma in Saturn's nightside magnetosphere and the

      implications for global circulation." *Planetary and Space Science* 57.14 (2009):

      1714-1722.

Németh, Z, et al. "Ion distributions of different Kronian plasma regions." *Journal of*

      Geophysical Research: Space Physics (1978–2012) 116.A9 (2011).

Ogawa, H., et al. "Secondary-electron emission from thin carbon foils by H^0 and H^+ in

      frozen-charge states." *Physical Review A* 65.5 (2002): 052902.

Porco, C. C., et al. "Cassini observes the active south pole of Enceladus." *Science*

      311.5766 (2006): 1393-1401.

Ritzau, S. M., and R. A. Baragiola. "Electron emission from carbon foils induced by keV

      ions." *Physical Review B* 58.5 (1998): 2529.

Rothard, H., et al. "Differential multi-electron emission induced by swift highly charged gold ions penetrating carbon foils." *Nuclear Instruments and Methods in Physics Research Section B: Beam Interactions with Materials and Atoms* 258.1 (2007): 91-95.

Rymer, A. M., et al. "Discrete classification and electron energy spectra of Titan's varied magnetospheric environment." *Geophysical Research Letters* 36.15 (2009).

Savitzky, A., and M. J. E. Golay. "Smoothing and differentiation of data by simplified least squares procedures." *Analytical chemistry* 36.8 (1964): 1627-1639.

Schröder, S. E., E. Karkoschka, and R. D. Lorenz. "Bouncing on Titan: Motion of the Huygens probe in the seconds after landing." *Planetary and Space Science* 73.1 (2012): 327-340.

Shematovich, V. I., et al. "Nitrogen loss from Titan." *Journal of Geophysical Research: Planets (1991–2012)* 108.E8 (2003).

Sigmund, P. "Particle-Induced Electron Emission: Open Questions, Pitfalls, and a Few Attempts at Answers." *Ionization of solids by heavy particles*. Springer US, 1993. 59-78.

Sillanpää, I., et al. "Hybrid simulation study of ion escape at Titan for different orbital positions." *Advances in Space Research* 38.4 (2006): 799-805.

Simon, S., et al. "Three-dimensional multispecies hybrid simulation of Titan's highly variable plasma environment." *Annales Geophysicae*. Vol. 25. No. 1. 2007.

Simon, S., et al. "Structure of Titan's induced magnetosphere under varying background magnetic field conditions: Survey of Cassini magnetometer data from flybys TA–T85." *Journal of Geophysical Research: Space Physics* 118.4 (2013): 1679-1699.

Sittler, E. C., et al. "Preliminary results on Saturn's inner plasmasphere as observed by Cassini: Comparison with Voyager." *Geophysical research letters* 32.14 (2005).

Sittler, E. C., et al. "Cassini observations of Saturn's inner plasmasphere: Saturn orbit insertion results." *Planetary and Space Science* 54.12 (2006): 1197-1210.

Sittler, E. C., et al. "Saturn's magnetospheric interaction with Titan as defined by Cassini encounters T9 and T18: New results." *Planetary and Space Science* 58.3 (2010): 327-350.

Smith, H. T., R. E. Johnson, and V. I. Shematovich. "Titan's atomic and molecular nitrogen tori." *Geophysical research letters* 31.16 (2004).

Smith, H. T., et al. "Discovery of nitrogen in Saturn's inner magnetosphere." *Geophysical research letters* 32.14 (2005).

Smith, H. T., et al. "Enceladus: The likely dominant nitrogen source in Saturn's magnetosphere." *Icarus* 188.2 (2007): 356-366.

Smith, H. T., et al. "Enceladus: A potential source of ammonia products and molecular nitrogen for Saturn's magnetosphere." *Journal of Geophysical Research: Space Physics (1978–2012)* 113.A11 (2008).

Spencer, J. R., et al. "Cassini encounters Enceladus: Background and the discovery of a south polar hot spot." *science* 311.5766 (2006): 1401-1405.

Storn, R., and K. Price. "Differential evolution–a simple and efficient heuristic for global optimization over continuous spaces." *Journal of global optimization* 11.4 (1997): 341-359.

Strobel, D. F. "Titan's hydrodynamically escaping atmosphere." *Icarus* 193.2 (2008): 588-594.

Szego, K., et al. "The plasma environment of Titan: The magnetodisk of Saturn near the encounters as derived from ion densities measured by the Cassini/CAPS plasma spectrometer." *Journal of Geophysical Research: Space Physics (1978–2012)* 116.A10 (2011).

Szego, K., et al. "Location of the magnetodisk in the nightside outer magnetosphere of Saturn near equinox based on ion densities." *Journal of Geophysical Research: Space Physics (1978–2012)* 117.A9 (2012).

Thomsen, M. F., and D. M. Delapp. "Numerical moments computation for CAPS/IMS." *CAPS TEAM/Los Alamos National Labs Public Release* (2005).

Thomsen, M. F., et al. "Survey of ion plasma parameters in Saturn's magnetosphere." *Journal of Geophysical Research: Space Physics (1978–2012)* 115.A10 (2010).

Tokar, R. L., et al. "Cassini observations of the thermal plasma in the vicinity of Saturn's main rings and the F and G rings." *Geophysical research letters* 32.14 (2005).

Tokar, R. L., et al. "The interaction of the atmosphere of Enceladus with Saturn's plasma." *Science* 311.5766 (2006): 1409-1412.

Tucker, O. J., and R. E. Johnson. "Thermally driven atmospheric escape: Monte Carlo simulations for Titan's atmosphere." *Planetary and Space Science* 57.14 (2009): 1889-1894.

Ulusen, D., et al. "Comparisons of Cassini flybys of the Titan magnetospheric interaction with an MHD model: Evidence for organized behavior at high altitudes." *Icarus* 217.1 (2012): 43-54.

Vesterstrom, J., and R. Thomsen. "A comparative study of differential evolution, particle swarm optimization, and evolutionary algorithms on numerical benchmark

problems." *Evolutionary Computation, 2004. CEC2004. Congress on*. Vol. 2. IEEE, 2004.

Vicanek, M, and H. M. Urbassek. "Statistics of light-ion-induced kinetic electron emission: The sum of Poisson distribution." *Physical Review B* 47.12 (1993): 7446.

Waite, J. H., et al. "The Cassini ion and neutral mass spectrometer (INMS) investigation." *The Cassini-Huygens Mission*. Springer Netherlands, 2004. 113-231.

Waite, J. Hunter, et al. "Liquid water on Enceladus from observations of ammonia and [40]Ar in the plume." *Nature* 460.7254 (2009): 487-490.

Wei, H. Y., et al. "Unusually strong magnetic fields in Titan's ionosphere: T42 case study." *Advances in Space Research* 48.2 (2011): 314-322.

Westlake, J. H., et al. "The observed composition of ions outflowing from Titan." *Geophysical Research Letters* 39.19 (2012).

Wilson, R. J., et al. "Cassini plasma spectrometer thermal ion measurements in Saturn's inner magnetosphere." *Journal of Geophysical Research: Space Physics (1978–2012)* 113.A12 (2008).

Woodson, A. K., et al. "Ion composition in Titan's exosphere via the Cassini Plasma Spectrometer I: T40 encounter." *Journal of Geophysical Research: Space Physics* (2014).

Yelle, R. V., J. Cui, and I. C. F. Müller‐Wodarg. "Methane escape from Titan's atmosphere." *Journal of Geophysical Research: Planets (1991–2012)* 113.E10 (2008).

Young, D. T., et al. "Cassini plasma spectrometer investigation." *The Cassini-Huygens Mission*. Springer Netherlands, 2004. 1-112.

Appendix A.

1. Abstract

Including the recent Maven mission to Mars and New Horizons mission to Pluto, thin, amorphous carbon foils (~2-17 nm nominal thickness) have been used in at least 20 different instruments on 18 spacecraft since 1990 [McComas et al., 2004]. The foils are commonly used in mass spectrometers, such as the Ion Mass Spectrometer (IMS) aboard Cassini, to generate start signals for time-of-flight (TOF) measurements. An ion passing through a carbon foil may, with some probability, emit electrons in both the forward and backward directions. Due to their relative mass, the electrons can be collected in a fraction of the incident ion's TOF, and so are used to trigger a TOF clock for the parent ion. For instruments that employ microchannel plate (MCP) detectors, such as Cassini's Ion Mass Spectrometer (IMS), ion detection depends on the multiplicity of electrons simultaneously incident on the MCP, and thereby the number simultaneously emitted from the foil. The distribution of this multiplicity is described by the electron number statistics (ENS), and while these statistics figure prominently in the conversion of IMS counts to ion densities, the available data is quite limited, particularly over the range of energies and ion species measured by IMS. In this appendix I describe my design and partial implementation of an apparatus for the measurement of ENS from thin carbon foils, with the ultimate goal of better calibrating IMS and other foil-based TOF mass spectrometers.

2. Background and justification

Section 3.2 above discusses the operation of IMS at some length and provides a reference for further details. Since detection and identification of an ion entering IMS is contingent upon prior detection of the electrons it emits from the carbon foil, and since each electron is detected with a probability $0.3 \leq p \leq 0.4$ (Reisenfeld et al., unpublished data, 2007), it is important to characterize the number of electrons that can be expected for a given ion. In particular, an ion that emits no electrons will not be counted and so the zero-emission probability, P_0, determines the spectrometer's counting loss. The species- and energy-dependent probability of detection for an ion entering the IMS collimator is given by

$$\eta(S, E) = \Gamma(E)\, \varepsilon_{\mathrm{SNG}}(S, E)\, \varepsilon_{\mathrm{TOF}}(S, E)$$

where Γ is the geometric efficiency defined in Eq. 3.9.2, $\varepsilon_{\mathrm{SNG}}$ is the probability that at least one electron is emitted from the carbon foil and detected at one of the ST "start" anodes, and $\varepsilon_{\mathrm{TOF}}$ is the probability that one of the parent ion fragments generates a "stop" at either the LEF anode or the central ST anode.

The electron "start" efficiency can be expanded into the following expression:

$$\varepsilon_{\mathrm{SNG}} = P_1\, p + P_2\, [2\, p\, (1 - p) + p^2] + P_3\, [3\, p\, (1 - p)^2 + 3\, p^2\, (1 - p) + p^3] + \cdots$$

$$= \sum_{n=1}^{\infty} P_n \sum_{j=1}^{n} \frac{n!}{j!\,(n-j)!} p^j (1-p)^{n-j} \,.$$

Here, P_n is the probability that an ion simultaneously emits n electrons from the foil in the forward direction and $p = T_{\text{grids}}\, \eta_{\text{elec}}(E)$ is the probability that a single electron is detected, as introduced above. Here, $T_{\text{grids}} \approx 0.74$ is the likelihood of transmission through various grids positioned in front of the ST MCP, and $0.4 \leq \eta_{\text{elec}}(E) \leq 0.54$ is the probability that a single electron incident on the ST MCP generates a "start" pulse [Reisenfeld et al, unpublished data, 2007].

The set $\{P_n\}_{n=0}^{\infty}$ constitutes the electron number statistics (ENS) and is a function of multiple parameters including ion species, ion energy, angle of incidence and carbon foil thickness. Given a set of ENS the average electron yield per ion can be written

$$\gamma = \sum_{n=1}^{\infty} n\, P_n$$

with

$$\sum_{n=0}^{\infty} P_n = 1$$

where the lower equation is the standard normalization condition.

The ENS currently used by the CAPS team were estimated by combining limited data from two separate studies and extrapolating the P_n based on a model that is not consistent with the data. The P_0 used by Reisenfeld et al. [unpublished data, 2007] in the calculation of the detection efficiencies discussed in Section 3.9 were estimated by averaging P_0 values inferred by Kozochkina et al. [1993] with those derived from the average yields of Ritzau and Baragiola [1998] assuming a Poisson distribution:

$$P_n = \gamma^n\, e^{-\gamma}/n! \;\Longrightarrow\; P_0^{RB} = e^{-\gamma_{RB}}.$$

Letting $\langle P_0 \rangle$ represent this average value, the P_n were then estimated by setting $P_0 = \langle P_0 \rangle$ and constraining the rest of the P_n such that

$$\gamma_{RB} = \sum_{n=1}^{\infty} n\, P_n\, .$$

Although ion-induced electron *yields* for carbon foils have been documented extensively in the literature, and to a lesser extent emission *statistics* for solid surfaces, only a handful of ENS measurements have been carried out with carbon foils [Clerc et al., 1973; Kozochkina et al., 1993; Billebaud et al., 1997; Ogawa et al., 2002; Rothard et al., 2007]. Of these studies, only Kozochkina and colleagues addressed the energy range relevant for the IMS, and only for four different ions: H^+, He^+, O^+, and S^+. Numerous authors [Dietz and Sheffield, 1975; Aumayr et al., 1991; Sigmund, 1993; Benka et al., 1995; Dubus et al., 1997; Ding et al., 1999] have noted that the ENS are not consistent

with Poisson statistics, particularly when yields are low. Some have suggested that the ENS are better described by a negative binomial (a.k.a. Polya) distribution [Benka et al., 1995; Dubus, et al. 1997; Ding et al. 1999] or a sum of Poisson distributions [Vicanek and Urbassek, 1993] based on emission from solid surfaces. To demonstrate this inconsistency, Figure A.1.1 juxtaposes the P_n reported by Kozochkina et al. [1993] with the Poisson functions calculated from their average yields. In all cases, agreement is poorest for low values of n and seems to worsen with increasing atomic number.

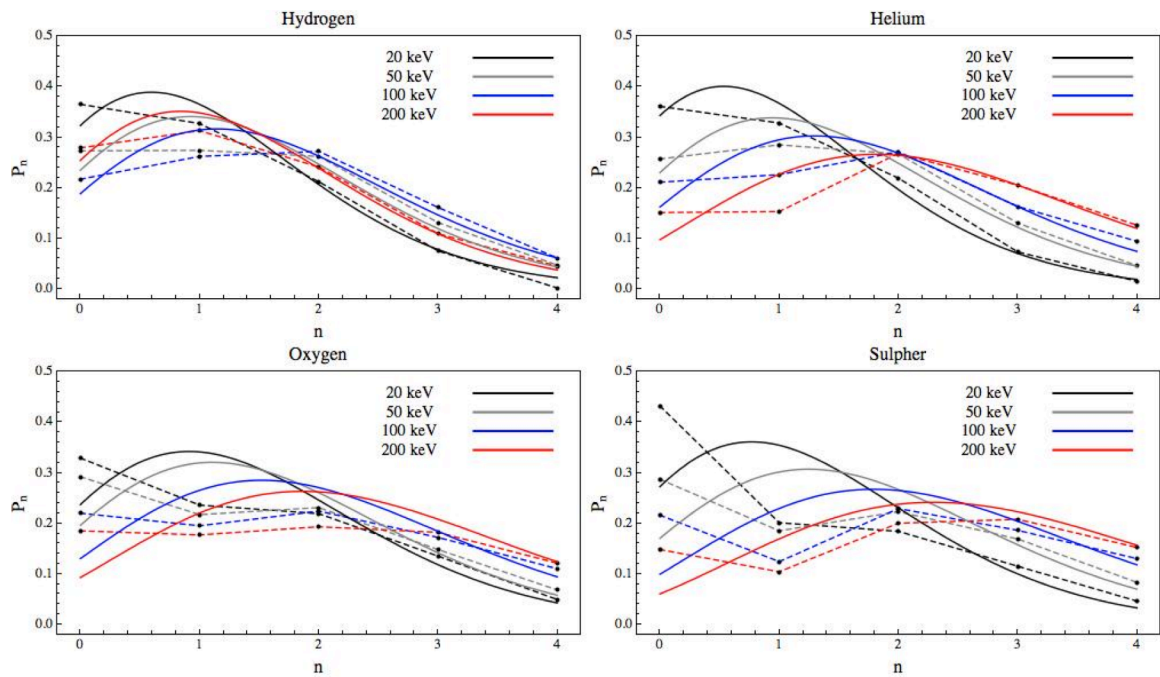**Figure A.2.1 Comparison of measured ENS with Poisson distribution**

A summary of the forward ENS measrued by Kozochkina et al. [1993]. Black points connected by dashed lines represent their reported values and solid curves are the Poisson distributions calculated from their reported yields. The color of each dashed line matches that of the corresponding Poisson curve. See pages I–XI for attributions.

The average yields measured by Ritzau and Baragiola [1998] using $\sim$1.4 μg/cm^2 carbon foils are several times larger than those reported by Kozochkina et al. [1993] for slightly thinner foils (nominally 0.5 μg/cm^2 or $\sim$2 nm thick). These larger yields imply P_0 values between 0.007 and 0.14, whereas the smaller ones imply P_0 values between 0.15 and 0.43. A number of factors can influence the inference of this zero-detection probability. Holes in the foil, for example, arising from mechanical shock, temperature fluctuations or radiation damage may increase the chances that an ion misses the foil altogether. In this case, the P_n from Kozochkina et al. [1993] fail to satisfy the normalization condition mentioned above, suggesting that their MCP efficiencies were not properly calibrated, leading to inaccurate ion counts. Moreover, R. Weller at Vanderbilt University (private communication) observed that foil thicknesses on the order of the electron attenuation length ($\sim$5 nm for low-energy electrons but not well known) reduced the efficiency of his TOF spectrometer by a factor of $\sim$3, presumably due to an increase in the number of zero-emissions, consistent with the differences noted above.

Contaminants have also been shown to reduce carbon foil yields in some cases [Ritzau and Baragiola, 1998] and enhance them in others by lowering the work function at the foil's surface [Arrale et al. 1994]. Ritzau and Baragiola used x-ray photoelectron spectroscopy to detect sodium adsorbed to their foils, a remnant of the water-soluble separating agent that allows the foil to be removed from the glass slide on which it's deposited. They found that the electron yield increased to a threshold value as the

contaminant was removed by keV sputtering and remained stable even after the foil was exposed to atmosphere.

In order to resolve these issues and expand upon the available data, I designed and constructed an apparatus to measure the number of forward-emitted electrons induced by 0–100 keV ions passing through 0.5-1.5 µg/cm^2 carbon foils. Section A.3 below presents the design of the apparatus as well as the construction and calibration of several components.

3. Design and partial implementation

Figure A.3.1 is a schematic diagram of the accelerator beam line on which the ENS experiment was installed. The Veeco-Accelerators Inc. ion implanter in the Laboratory for Atomic and Surface Physics at UVa is capable of producing ion fluxes on the order of 10^{13} ions cm^{-2} s^{-1} and energies up to, nominally, 300 keV per charge. Neutral gases are injected into a quartz glass tube and excited by an alternating RF voltage, which ionizes the gas through collisions with free electrons. A solenoid surrounding the quartz tube acts to enhance the rate of collision by coupling the plasma to its magnetic field. A positive probe voltage placed on an anode at the end of the glass tube reflects plasma ions toward an aperture at the front of the tube where they encounter a negative extraction voltage. The extracted ions are subsequently focused by an Einzel lens and accelerated by an array of ring-shaped electrodes.
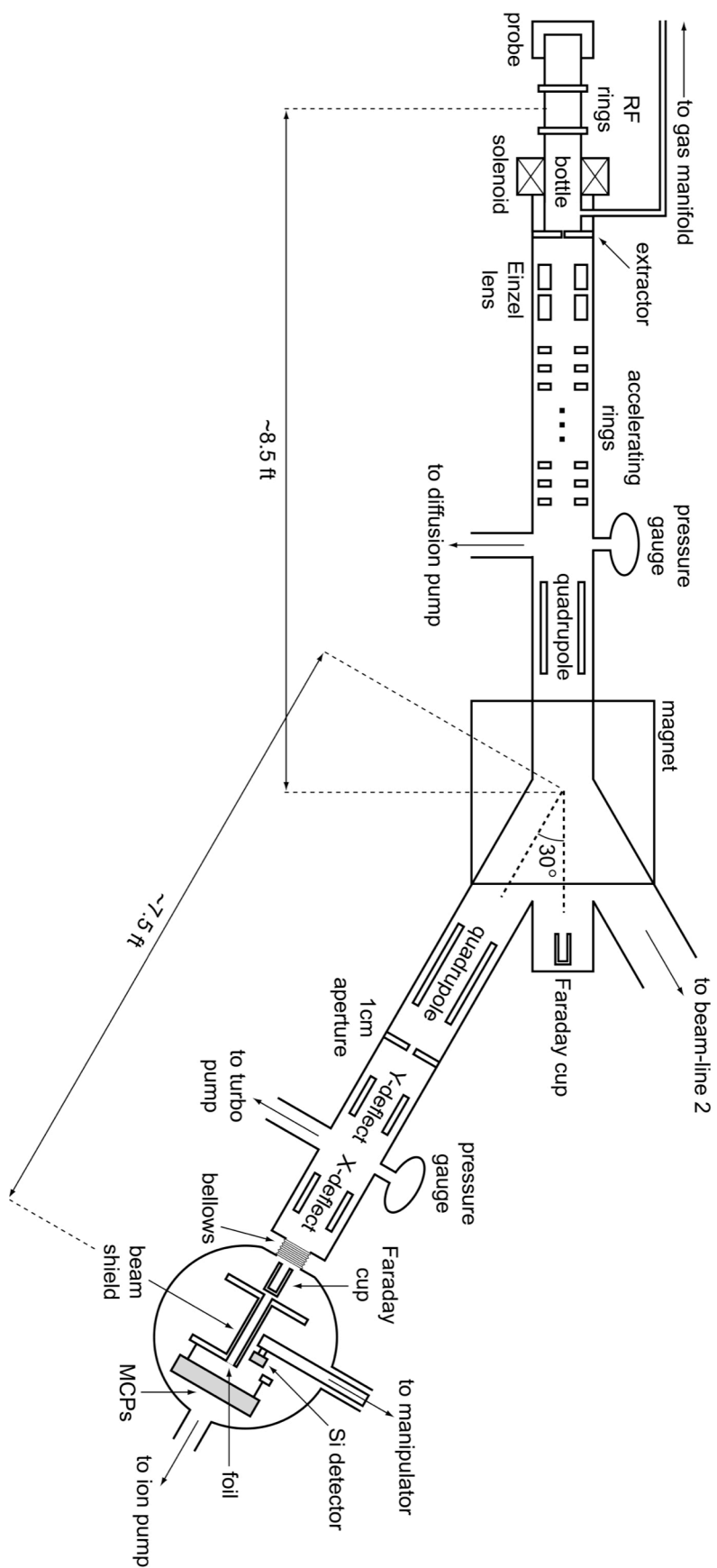
Figure A.3.1 Schematic diagram of ion accelerator, beam line, and experiment chamber

See pages I–XI for attributions.

120

After the acceleration stage the beam is maximized on a Faraday cup at $0^°$ to the primary beam direction, and then mass-selected and steered down one of two beam-lines by an electromagnet capable of producing a uniform field up to ~4 kG. A second quadrupole and a set of deflection plates after the magnet allow further steering and rastering before the ions enter the target chamber. The accelerator is maintained at ~10^{-6} Torr by a backed diffusion pump and separated from the experiment chamber by a 1 cm diameter differential aperture. On the low-pressure side of the differential, a backed turbo-molecular pump between the aperture and target chamber reduces the pressure by approximately half while an ion pump achieves ~10^{-7} Torr within the experiment chamber itself. Pressures are continuously monitored at the accelerator and directly above the turbo pump by Bayard-Alpert ionization gauges, while the ion pump controller reports the pressure within the target chamber.

Once the ion beam has been maximized on the $0^°$ Faraday cup, the mass-selecting magnetic field is increased until the desired ion is detected in the second, retractable Faraday cup at the entrance to the target chamber, as depicted in Figure A.3.1. The beam is then centered on this cup using the second quadrupole and the deflection plates. Finally, the beam is reduced to the desired level by manipulating the probe and extractor voltages and the solenoid current, and by rastering the beam with the deflection plates. Beyond the second Faraday cup the beam traverses a set of reducing apertures and a tube that shields it from the electron-steering potential. At the end of the tube the ions pass through the carbon foil and strike the MCP detector, while the ejected electrons are drawn onto an ion-implanted Si charged-particle detector floating at 30 kV. Figure A.3.2

shows a schematic drawing of the detector assembly inside the experiment chamber as seen from above.
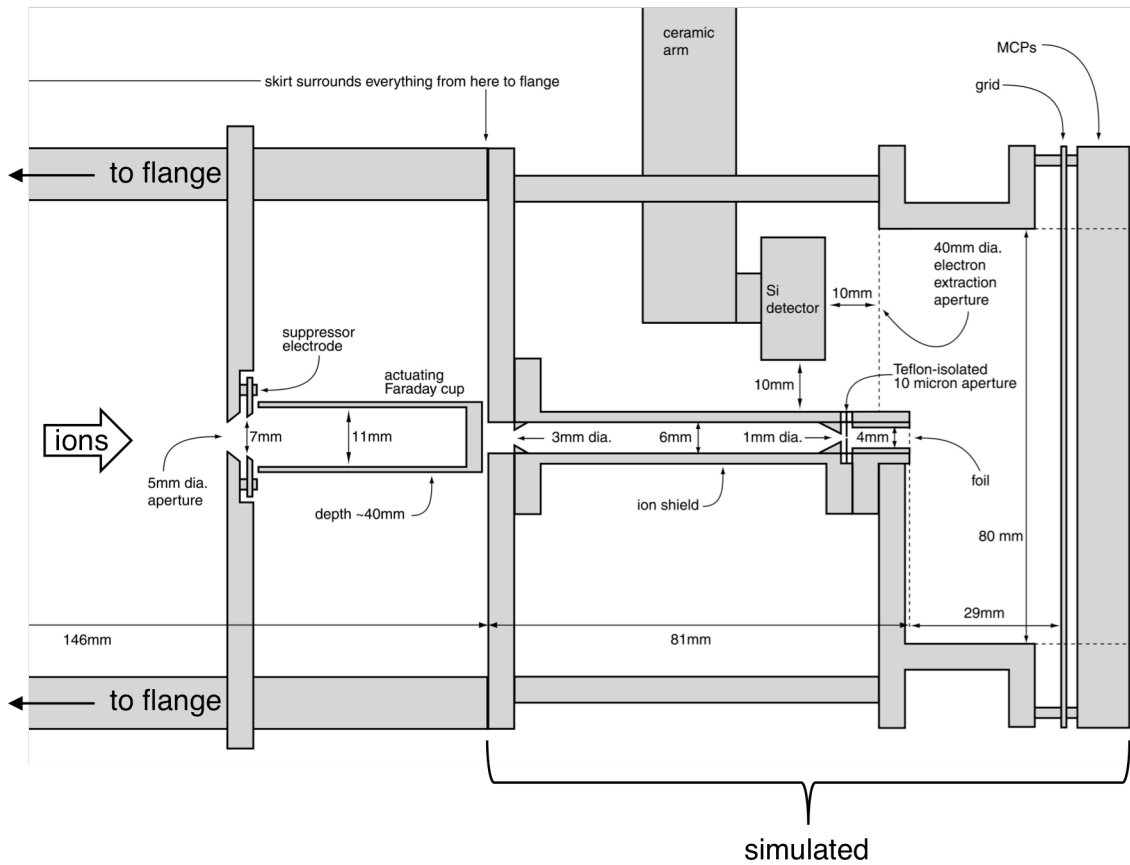
Figure A.3.2 Schematic diagram of detector assembly

A scale drawing of the detector assembly inside the experiment chamber. The portion labeled "simulated" corresponds to the leftmost panel in Figure A.3.3. The assembly connects to the experiment chamber flange (i.e. wall) at left as indicated. See pages I–XI for attributions.

A pair of disk-shaped MCPs mounted in a chevron configuration are suspended a few centimeters downstream from the carbon foil. Each MCP is a semiconducting lead-

glass disk with an 80 mm diameter active area, ~45% of which is etched with 25-micron pores angled 8° to the surface, for a total of approximately 4-5 million pores. Two such MCPs are placed together, their channels inclined in opposition such that an incident ion induces a cascade of electrons from the first plate, and each electron is further multiplied by the second plate producing a gain of ~4 million electrons per ion. A suppression grid held a few millimeters from the input surface of the first plate at –200 V helps to reflect electrons emitted from the foil toward the Si detector and also enhances the MCP gain by returning electrons that might otherwise escape from the surface. The input surface of the front MCP is held at ground potential while the output surface of the rear MCP is held at +2400 V. This potential difference produces a "strip" current that replenishes electrons ejected from the channel walls by incident ions. Lastly, a voltage difference of +300 V between the rear MCP and the anode expedites the collection of electrons emerging from the rear MCP.

Electrons emitted from the carbon foil are drawn through an extraction aperture onto the Si detector in a fashion similar to that described by Aumayr et al. [1991]. While several authors have used MCPs to detect electrons from carbon foils, the lower efficiency and wider pulse-height distribution of the MCP compares poorly to the exceptional energy resolution, linearity and efficiency of a Si charged particle detector. The Si detector operates as a reverse-biased semiconducting diode. A +130 V bias placed across the detector's electrodes produces an interior region depleted of free charge carriers. Radiation entering the depleted region creates electron-hole pairs in proportion to the amount of energy deposited, which are then drawn apart by the applied bias and

collected on opposing electrodes generating a measurable charge pulse. Since the charge-collection time of the Si detector is much longer than the difference in arrival times of electrons emitted from a carbon foil by the same ion, the pulse height is proportional to the number of electrons incident on the detector's surface. Thus, when n electrons impact the Si detector simultaneously they deposit energy equal to $n \times 30$ keV and generate a proportional output pulse, discriminating n since the detector has an energy resolution between 6 and 8 keV. A small correction must be applied to account for the fraction of electrons backscattered at the detector's surface as detailed in Aumayr et al. [1991].

I have taken great care in the design of the detector assembly to maximize the collection of both incident ions and emitted electrons while also shielding the pre-foil ion trajectories from the electron steering potential. It is crucial to collect every electron emitted from the carbon foil by an incident ion because an ion signal with no accompanying electron signal is interpreted as a zero-emission and counted toward the ENS. On the other hand, although it would be satisfying to capture every ion exiting the foil, it is not essential to the integrity of the experiment. Coincidence gating ensures that an electron signal is discarded if no coincident ion is detected, and so such events do not influence the measured ENS.
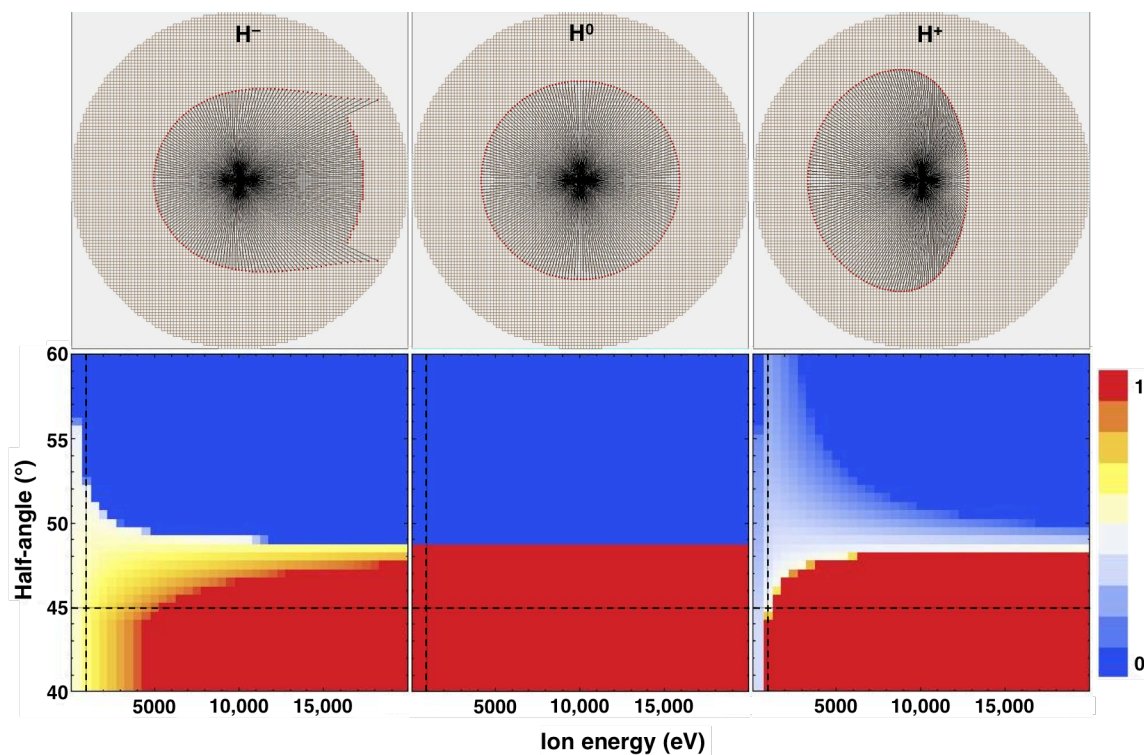
Figure A.3.3 Simulation of ion trajectories and collection efficiencies

Trajectories for positive (top left), neutral (top center), and negative (top right) hydrogen

fragments emerging from the center of the carbon foil at ~45° to the beam axis and

striking the MCP, as viewed from the carbon foil. All ion energies are 1 keV. In each

panel the Si detector, floating at +30 kV, is to the right. The density plots in the bottom

row show the corresponding ion collection efficiencies. See pages I–XI for attributions.

Multiple detector geometries and their resulting ion and electron trajectories were

modeled using SIMION 8.0 in order to find the optimum configuration. The 30 kV

potential on the Si detector produces a potential "finger" that reaches into the electron

extraction aperture and rests on the carbon foil, while the -200 V potential on the

suppression grid acts as a mirror reflecting the electrons back in the direction of the Si

detector. Figure A.3.3 shows simulated trajectories for light, low-energy (relative to the IMS post-acceleration energy) ions emerging from the carbon foil at 48° to the foil normal and striking the MCP, while Figure A.3.4 shows simulated trajectories of electrons between the surface of the carbon foil and the active area of the Si detector.
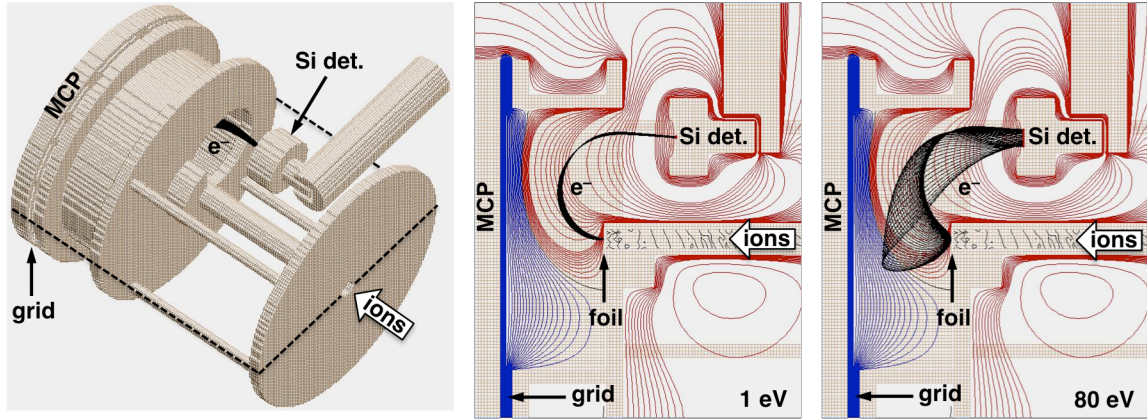
Figure A.3.4 Simulation of electron trajectories

The 3D SIMION model used to simulate electric potentials and electron trajectories (left) and cross-sections through the model showing the trajectories of 1 eV (center) and 80 eV (right) emitted electrons. Black dashed lines at left indicate the plane of the cross-sections. Blue lines indicate negative electric equipotential surfaces and red lines indicate positive ones. The grid and Si detector are held at −200 V and +30 kV resepectively. See pages I–XI for attributions.

Figure A.3.5 plots the simulated electron-collection efficiency of the apparatus as a function of Si detector position and electron energy. The simulation demonstrates that 100% collection of randomly generated trajectories launched at angles up to 89° from the foil axis can be achieved up to energies of ~80 eV, or much greater than 99% of the total

energy distribution according to Meckbach et al. [1975], while maintaining a safe

separation between the floating Si detector and the grounded assembly. Figure A.3.6

shows the actual detector assembly that was constructed and installed in the experiment

chamber (recall the leftmost panel of Figure A.3.4) based on the success of simulated

design.
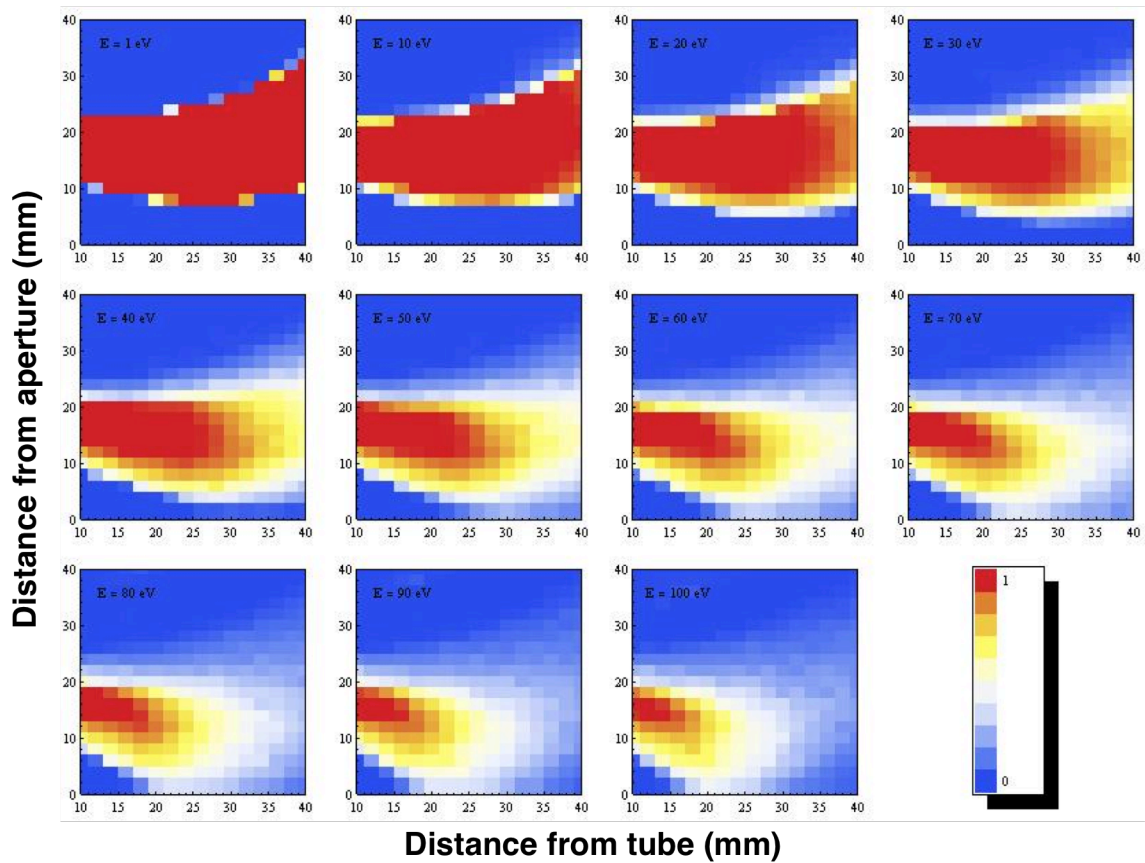
Figure A.3.5 Simulated electron collection efficiencies

The fraction of electrons collected by the Si detector for various emission energies

between 1 eV (top left) and 100 eV (bottom right) as simulated with SIMION. See pages

I–XI for attributions.
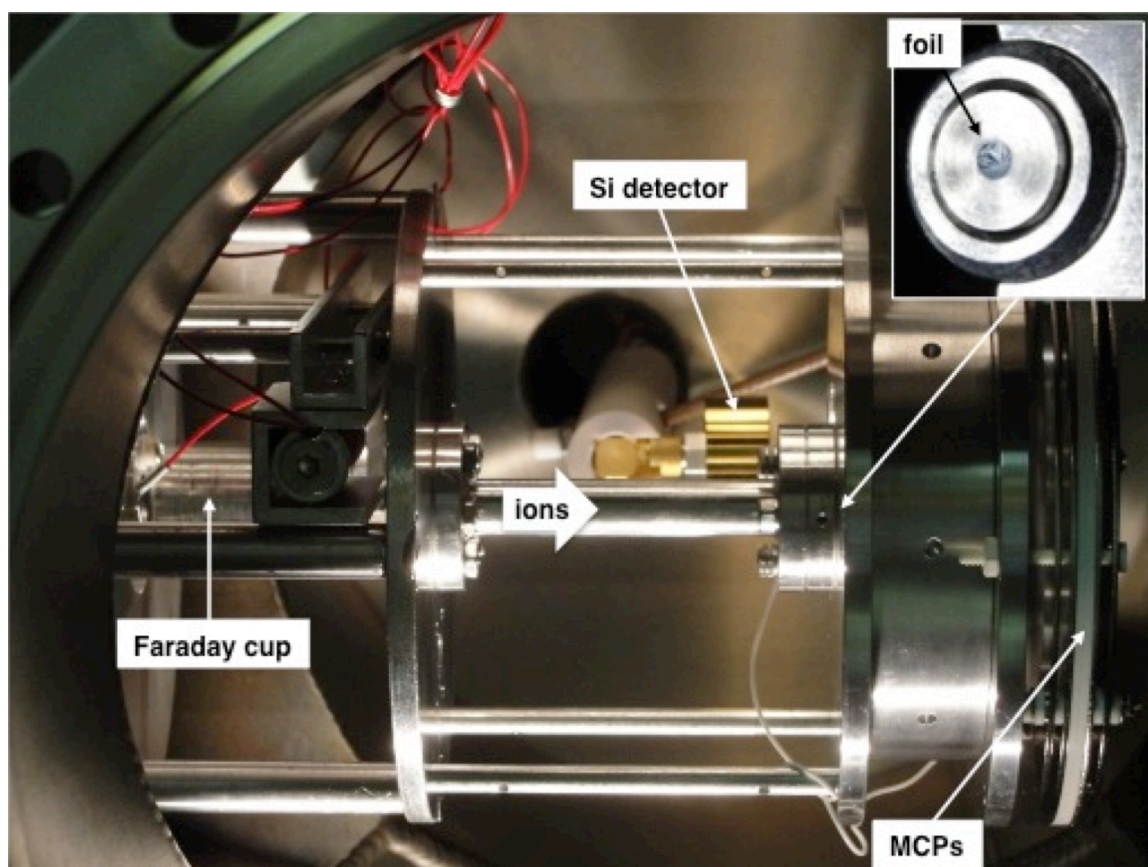
Figure A.3.6 Annotated photograph of detector assembly inside vacuum chamber

See pages I–XI for attributions.

The signal processing circuit that I have assembled for the experiment is depicted in figure A.3.6. Since the Si detector floats at high voltage, all electronic devices connected to it must be isolated from the building mains. Therefore, I constructed a power supply from a rechargeable, regulated battery pack and a set of DC/DC converters to operate the amp and preamp for the Si detector and to provide its 130 V bias. Two separate, current-limited power supplies provide the biases for the rear MCP (2400 V) and anode (2700 V). A charge-sensitive preamp accepts the signal from the Si detector

and produces a positive needle pulse > 45 mV for every 1 MeV deposited in the depleted region of the Si detector. This needle pulse is then shaped and amplified, decoupled from 30 kV through a pair of 22 nF, 40 kV capacitors and fed into a unity-gain delay amplifier for coincidence-timing purposes. The output from the delay amplifier is split and sent to an analog-to-digital converter (ADC) for pulse-height analysis as well as a single channel analyzer (SCA). The SCA produces two outputs, one that is counted by a National Instruments data acquisition (DAQ) card installed in a desktop computer, and one that is further conditioned and routed to a NIM logic unit with anti-coincidence detection capabilities. I have written a custom LabView program to interface with a multifunction DAQ card that steps the MCP voltages, as well as the timer-counter card that tallies the ion, electron, and zero-emission signals coming from the SCAs and the logic unit.

Figure A.3.7 Signal processing electronics

A schematic diagram of the signal processing electronics for the ENS experiment. Connections between components indicate cable types used and barrel-shaped symbols indicate nonstandard coaxial connectors. See pages I–XI for attributions.

National Instruments 6036E DAQ Card

NI SH6868

National Instruments BNC-2090 Breakout Box

Ortec C-25

Ortec 456 High Voltage Power Supply (rear MCP)

Ortec C-25

Canberra 3002D High Voltage Power Supply (MCP anode)

Canberra C123

Burle 3075MA MCP Chevron Assembly

Ortec Ultra Ion-implanted Si Detector

Vacuum Chamber

Canberra C123

Canberra C123

Ortec C-24

Ortec 142A Charge Sensing Preamp

Ortec C-24

Power cable

Floating Power Supply (battery + DC/DC converters)

Spellman SL120P30 High-Voltage Power Supply

HV cable with ground shield cut back (i.e. no return path)

Ortec C-36

15K ohm 1W res

4700 pF 6kV cap

Ortec 572 Amplifier

Homemade power cable

Acrylic Isolation Box: Everything inside at 30kV

F BNC/M BNC

22nF 40kV Cap

22nF 40kV Cap

M BNC/F BNC

Ortec C-25

Ortec 471 Amp

Ortec C-25

Ortec 427 Delay Amplifier (unity gain)

Ortec C-25

Canberra 2037A TSCA

Canberra 2037A TSCA

Canberra C128

Canberra C128

Canberra C128

Canberra C128

Phillips 755 Quad 4-Fold Logic Unit

LeCroy 428F Quad Linear Fan-In-Fan-Out

Ortec LL174 x 3

LeCroy 688AL Quad Linear Level Adapter

Ortec LL174

Canberra C128

Canberra C128 x 3

Ortec 926 ADCAM MCB

Ortec 926-C

Computer

National Instruments BNC-2121 Breakout Box

NI SH6868

National Instruments PCI-6602 Counter/Timer

The ion signal is likewise decoupled from the bias on the MCP anode through a 4700 pF, 6 kV capacitor and then shaped and amplified. The amplified ion signal is split and sent to an identical SCA module as well as the MCA's gate input. Again, one of the SCA outputs is routed to the DAQ card for counting, while the other is sent to the logic unit. This configuration allows for both coincidence gating of the electron signal as well as direct counting of zero-emission events. Specifically, electron signals fed to the ADC are only analyzed if a concurrent ion signal is present at the ADC's gate input, and an ion signal fed to the NIM logic module is counted as a zero-emission event *unless* a concurrent electron signal is present to veto it.
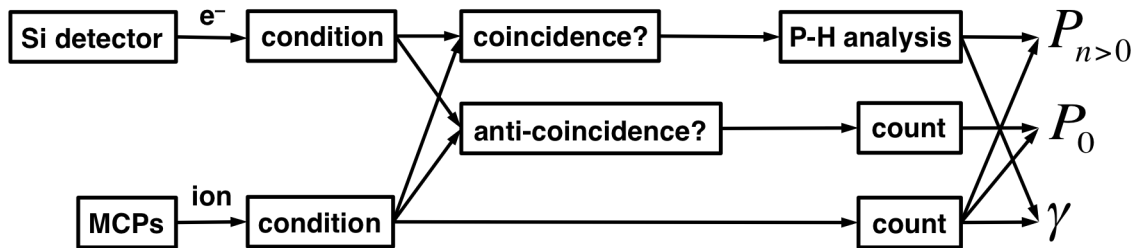

Figure A.3.8 Simplified signal processing flow chart

See pages I–XI for attributions.

The pulse-height analysis and the ion, electron, and anti-coincidence counts provide all the data necessary to determine the ENS, as depicted in the simplified flow chart in Figure A.3.7. P_0 is calculated by dividing the number of anti-coincidence events by the total number of ions counted. For n > 0 the *n*th peak of the pulse-height spectrum is integrated and P_n calculated by dividing the peak area by the total number of ions counted. This method is elegant because, since electrons are counted only in tandem with

131

coincident ions, every analyzed electron and every anti-coincidence event must necessarily accompany an ion event, and so the efficiency of the MCPs can be ignored. In other words, missed ions don't effect the deduced statistics because if no ion is counted then *nothing* is counted.
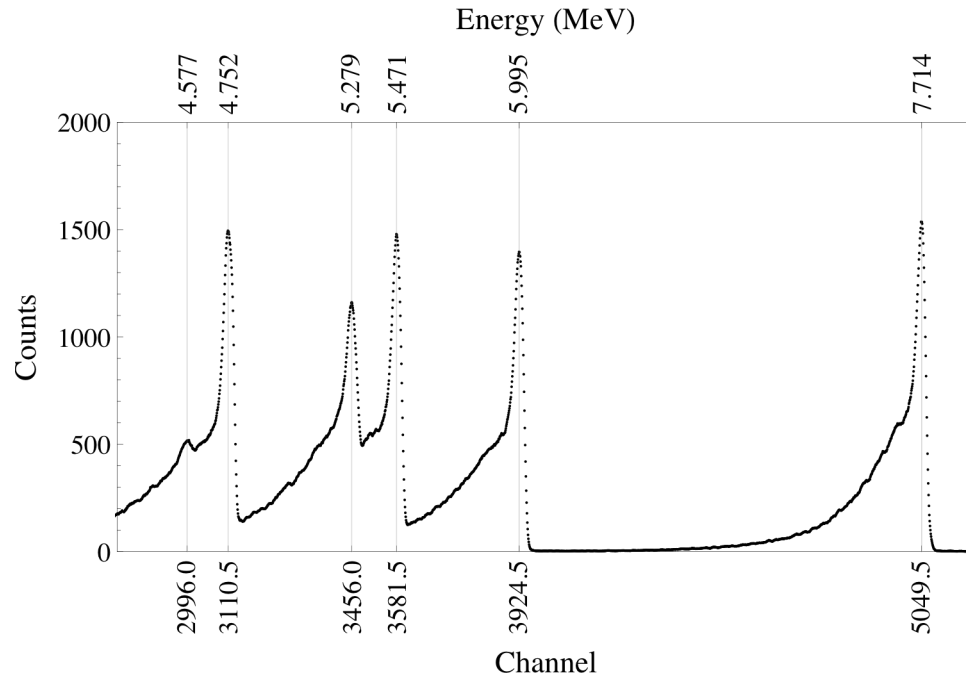

Figure A.3.9 Calibration of Si detector and associated electronics

See pages I–XI for attributions.

The MCA interface is provided by Ametek's Maestro-32 software, which also furnishes data-analysis tools such as peak-detection and integration. The MCA scale was calibrated by exposing the Si detector to a [226]Ra alpha source and correlating the observed peak positions with the known energies of the alphas. The resulting spectrum is shown in Figure A.3.9. The energy lost by the alphas passing through the detector's thin,

passive Si layer en route to the depleted region was simulated using TRIM 2008 and determined to be only ~30eV. Lastly, Figure A.3.10 shows several gain curves resulting from calibration of the MCPs and associated electronics. The object of the calibration was two-fold: to determine the location of the "knee" (~2200 V) which marks the nominal MCP operating voltage, and to ensure that a low current of ~2000 ions/s could be achieved on the face of the MCP in accord with timing restrictions imposed by the signal processing electronics.
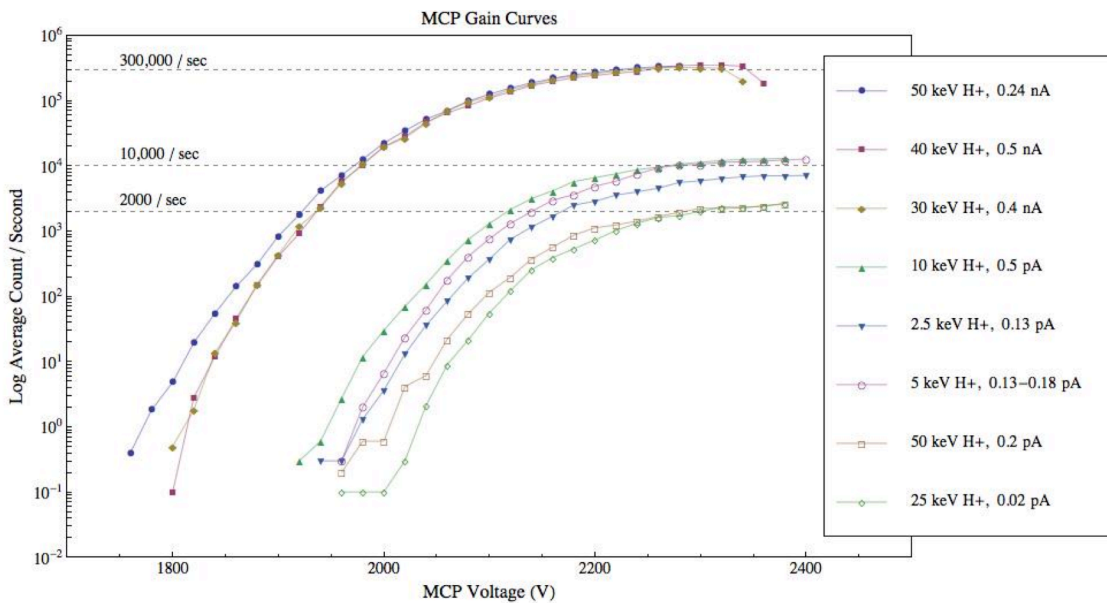

Figure A.3.10 Calibration of MCP detectors and associated electronics

See pages I–XI for attributions.

Appendix B. Publications and presentations

1. Authored Publications

Woodson, A. K., Smith, H. T., Crary, F. J., & Johnson, R. E. (2014). Ion composition in Titan's exosphere via the Cassini Plasma Spectrometer I: T40 encounter. *Journal of Geophysical Research: Space Physics*.

2. Coauthored Publications

Elrod, M. K., Tseng, W.-L., Woodson, A. K., & Johnson, R. E. (2014). Seasonal and radial trends in Saturn's magnetospheric plasma between the main rings and Enceladus, *Icarus*, 242, 130–137.

3. Invited Talks

A. K. Woodson, H. T. Smith, F. J. Crary and R. E. Johnson. Ion composition in Titan's exosphere from the Cassini Plasma Spectrometer. Presented at the Fall 2013 meeting of the American Geophysical Union in San Francisco, California (9–13 December, 2013).

4. Oral Presentations

A. K. Woodson, H. T. Smith, F. J. Crary and R. E. Johnson. Ion composition in Titan's
exosphere during T40. Presented at the joint Cassini Plasma Spectrometer/Ion and
Neutral Mass Spectrometer team meeting in Laurel, Maryland (14–16 October,
2014).

A. K. Woodson, H. T. Smith, F. J. Crary and R. E. Johnson. Ion composition in Titan's
wake from CAPS IMS data. Presented at the joint Cassini Plasma
Spectrometer/Ion and Neutral Mass Spectrometer team meeting in Surrey,
England (6–8 May, 2014).

A. K. Woodson, H. T. Smith, F. R. Crary and R. E. Johnson. Ion compoisition in Titan's
exosphere from CAPS IMS. Presented at the 45th Cassini Plasma Spectrometer
Team Meeting in San Antonio, Texas (29 October–1 November, 2013).

A. K. Woodson, H. T. Smith, F. J. Crary, M. Shappirio and R. E. Johnson. Mapping
methane loss at Titan with the IMS. Presented at the 44th Cassini Plasma
Spectrometer Team Meeting in Boulder, Colorado (7–8 Bebruary, 2013).

A.K. Woodson, F. J. Crary and R. E. Johnson. A multi-encounter survey for CH_x^+ near
Titan. Presented at the 42nd Cassini Plasma Spectrometer Team Meeting in
Glacier National Park, MT (16–17 September, 2011).

A.K. Woodson and R. A. Baragiola. Carbon foil electron emission statistics: experiment
overview and status. Presented at the 42nd Cassini Plasma Spectrometer Team
Meeting in Glacier National Park, MT (16–17 September, 2011).

5. Poster Presentations

A. K. Woodson and R. E. Johnson. Mapping methane escape at Titan with the Cassini

    Plasma Spectrometer. Presented at the Presented at the 44th annual meeting of the

    AAS Division for Planetary Sciences in Reno, Nevada (14–19 October, 2012).

A. K. Woodson, M. K. Elrod and R. E. Johnson. Mapping methane escape at Titan with

    the Cassini Plasma Spectrometer. Presented at the Fall 2012 meeting of the

    American Geophysical Union in San Francisco, California (3–7 December, 2012).

A. K. Woodson, H. T. Smith and R. E. Johnson. Ion composition in Titan's exosphere

    from the Cassini Plasma Spectrometer. Presented at the 45th annual meeting of

    the AAS Division for Planetary Sciences in Denver, Colorado (6–11 October,

    2013).